UNIVERSITY OF CALIFORNIA, SAN DIEGO

Northerly surface wind events over the eastern North Pacific Ocean: Spatial distribution, seasonality, atmospheric circulation, and forcing

A Dissertation submitted in partial satisfaction of the requirement for the degree

Doctor of Philosophy

in

Oceanography

by

Stephen V. Taylor

Committee in charge:

Professor Konstantine Georgakakos, Chair
Professor Daniel Cayan, Co-Chair
Professor Scott Ashford
Professor Walter Munk
Professor Joel Norris

2006

The Dissertation of Stephen V. Taylor is approved, and it is acceptable in quality and form for publication on microfilm:

_____

_____

_____

_____
Co-Chair

_____
Chair

University of California, San Diego

2006

DEDICATION

To all who maintain the interest and exert the effort to learn

TABLE OF CONTENTS

ACKNOWLEDGEMENTS

This research was supported by a student assistantship administered by the Board of Directors of the Hydrologic Research Center, a public benefit corporation. Additional support was provided by Scripps Institution of Oceanography at the University of California, San Diego through the California Applications Program. The California Applications Program is sponsored by the National Oceanic and Atmospheric Administration. Figures herein were created with either GrADS or xmgr.

The first chapter of this dissertation was written with coauthors and submitted as a journal article whose citation is:

Taylor, S.V., D.R. Cayan, N.E. Graham, and K.P. Georgakakos, "Northwesterly surface winds over the eastern North Pacific Ocean in spring and summer". Journal of Geophysical Research – Atmospheres, *submitted September, 2006*.

Several individuals deserve recognition as well. Barbara Hansen and Genevieve Taylor helped with formatting, which any Ph.D. recipient can tell you is no small task. Comrades at the Hydrologic Research Center including Theresa Carpenter, Bob Jubach, Corinne Shafer, Eylon Shamir, Jason Sperfslage (the "Wizard" of Iowa), have all played a role in helping me along and generally creating a fun research environment. In particular, Wang Jianzhong deserves thanks for helping with part of the dissertation.

At SIO, there are too many professionals, colleagues, and friends to thank here, but I will mention John Roads in particular for recruiting me to attend SIO. Gabrielle Ayers deserves a special mention for developing my teaching skills in a place that is all about research.

As one might expect at SIO, all committee members are exceptional scientists and leaders of their respective disciplines. I enjoyed reading about Professor Ashford's research in the newspaper and I thank Professor Norris for his understanding, unpretentious nature, and excellent advice – especially in preparation for the defense. No one enjoys their research like Professor Munk. His intellectual curiosity is inspiring and contagious.

My two advisors deserve special thanks. Dan Cayan and Kosta Georgakakos are both exceptional mentors. Dr. Cayan's monthly calendar probably has more "blackout dates" than a major

airline in December, yet it always seemed that he was pushing me to schedule another meeting with him. A few years back my car was stolen (I got it back…it had over 200,000 miles on it). Dr. Georgakakos practically jumped out of his chair to offer the use of his own car. In short, I could not have hoped for more competent or compassionate advisors. Thank you.

A tip of the hat is also due to Dr. Nick Graham. Through some bureaucratic irregularities, he could not officially serve as one of my committee members, but he has done as much as anyone to ensure my graduation and success. Nick has been like an older brother and is just as eager to help me as he is to show me interesting details of his latest project.

Finally, I am very happy to thank my wife for seeing me through the hard work and poverty that all professional students know and love; I am lucky to have conscientious parents who teach effectively by example.

VITA

2006	Doctor of Philosophy in Oceanography Scripps Institution of Oceanography University of California, San Diego
2001	Master of Art in Geography University of California, Santa Barbara
1993	Bachelor of Science in Physics University of California, Santa Barbara

Publications in Refereed Journals

Taylor, S.V., D.R. Cayan, N.E. Graham, and K.P. Georgakakos (2006), Northwesterly surface winds over the eastern North Pacific Ocean in spring and summer. Journal of Geophysical Research - Atmospheres, *submitted September 2006.*

Carpenter, T.M., J. Wang, S.V. Taylor, E. Shamir, J.A. Sperfslage, and K.P. Georgakakos (2006), Heavy precipitation and flash flooding in Southern California provide impetus for survey of hydrologic response in mountain streams. EOS, Transactions, American Geophysical Union, *in press*.

Other Publications

Georgakakos, K.P., N.E. Graham, T.M. Carpenter, E. Shamir, J. Wang, J.A. Sperfslage, and S.V. Taylor (2006), Integrated forecast and reservoir management (INFORM) for Northern California: System development and initial demonstration. Hydrologic Research Center Technical Report No. 5.

Georgakakos, K.P., E. Shamir, S.V. Taylor, T.M. Carpenter, and N.E. Graham (2004), Integrated forecast and reservoir management (INFORM) - A Demonstration for Northern California, Phase I Progress Report. Hydrologic Research Center Limited Distribution Report No. 17.

Graham, N.E., S.V. Taylor, J.A. Sperfslage, T.M. Carpenter, and K.P. Georgakakos (2001), Training and Technology Transfer for enhancing the spatial variability of historical rain gauge precipitation fields for extended streamflow prediction analysis with the Nile Forecast System. Hydrologic Research Center Technical Note No. 15.

S.V. Taylor (2001), Variability of evaporation and precipitation associated with the North Atlantic Oscillation: Implications for deep oceanic convection in Labrador and Greenland Seas. Master's Thesis. Department of Geography, University of California, Santa Barbara.

Fields of Study

Studies in Climate and Climate Change
Professor V. Ramanathan

Studies in Atmospheric Dynamics
Professor R. Somerville

Studies in Climate Prediction
Professor J. Roads

Studies in the Carbon Cycle
Professor R. Keeling

Studies in Rapid Climate Change
Professor J. Severinghaus

Studies in the Geologic Record of Climate Change
Professor C. Charles

ABSTRACT OF THE DISSERTATION

Northerly surface wind events over the eastern North Pacific Ocean: Spatial distribution, seasonality, atmospheric circulation, and forcing

by

Stephen V. Taylor

Doctor of Philosophy in Oceanography

University of California, San Diego

Professor Konstantine Georgakakos, Chair

Professor Daniel Cayan, Co-Chair

The climate of the coastal US West coast is characterized by cool, alongshore, northerly wind from the Oregon border to the Southern California Bight, south of Point Conception. New datasets, including surface wind estimates derived from satellite scatterometer and North American Regional Reanalysis fields allow for a more detailed exploration than has heretofore been possible. This thesis examines episodes of enhanced northerly surface wind to determine the spatial and temporal character of the surface wind along and offshore of the California coast and the 3-D structure and seasonality of the atmosphere associated with the wind episodes. A deterministic approach is employed to enhance understanding of fundamental processes rather than improve predictability. The methodology includes diagnostic spatial and temporal analysis and numerical sensitivity experiments. Processes known to affect coastal wind are investigated to gain a better understanding of the role of possible mechanisms

driving northerly wind events. It is found that the spatial and temporal structure of wind offshore of California is characterized by episodes of enhance equatorward surface wind that often extend from Cape Mendocino to Hawaii. Wind events typically last four days and are present 20% of the time during January-August. The summer circulation structure associated with wind events is fundamentally different than winter and spring. For instance the surface and upper-air circulation patterns associated with wind events are co-located in winter and 90° out-of-phase in summer. Wind events are nearly always accompanied by a strong trough in the upper-air circulation that is directly above or just east of the coast. The analysis concludes that troughs are a nearly universal forcing mechanism for wind events, while the low-level atmospheric thermal gradient across the coast also plays an important, but less consistent role in wind events. A hypothesis is developed suggesting that southeastward movement of the North Pacific High may be a sufficient forcing mechanism for wind events in summer, but a trough along the coast is a necessary ingredient in winter. Other forcing mechanisms, feedbacks, and processes may also be important in reinforcing the circulation associated with wind events.

CHAPTER ONE

Northwesterly surface winds over the eastern North Pacific Ocean in spring and summer

Abstract

Variability in space and time of northwesterly surface wind in the subtropical eastern North Pacific Ocean is studied using observational records including six years of high resolution (25 km) satellite scatterometer winds and 20+ years of coastal buoy observations. The strongest and most persistent winds in the northeastern Pacific Ocean are concentrated along the California coast from Cape Mendocino to just south of Point Conception and extending west from the coast about 800 km, where more than 50% of all winds exceed 7.5 m/s from the northwest from March-September. Persistent northwesterly winds along and offshore of the California coast in spring and summer are broken up by intermittent, short duration calm periods. The variability of winds can be described as a collection of events of duration one day to two weeks, with frequency of one to four events per month over a spatial scale several degrees in both longitude and latitude. Composites of scatterometer winds based on threshold wind speed at a nearshore coastal buoy demonstrate that wind events maintain a spatially coherent structure throughout their duration. Events lasting 1-2 days are the most common and the frequency of events decreases with duration. However, about 40% of the combined event time is occupied by events lasting longer the synoptic time scale (1-5 days). From inception, events during April-August intensify and spread across a surprisingly vast region of the eastern North Pacific Ocean from the Northern California coast southwestward to Hawaii. Clear signals in the mean composite evolution fade after about five days. Spring and summer wind events appear to coincide with increased trade winds, suggesting a large-scale influence.

1.1 Introduction

1.1.1 Background

Moderate to strong surface wind offshore the US West coast in spring and summer arises from the sea level pressure gradient between the eastern North Pacific high and relatively low pressure over the southwestern US (Nelson 1977; Halliwell and Allen, 1987). Figure 1 shows the mean winds and SLP for Apr-Aug. The equatorward pressure gradient along the US west coast is the strongest and most persistent in North America (Brost et al. 1982). Subsidence below the high pressure system maintains a temperature inversion and marine boundary layer in the lower atmosphere. Coastal geometry combined with large-scale atmospheric circulation, oceanic upwelling of relatively cold water, thermal land heating, and marine boundary layer are parts of a coupled ocean-atmosphere-land system that includes relatively persistent and moderate equator-ward surface wind (Seager et al. 2003; Miyasaka and Nakamura, 2005). This coupled system maintains mild summer temperatures and is the dominant climatic feature of subtropical western continental coasts of the world (Lorenz 1969; Mass et al. 1986; Winant et al. 1988).

Baroclinicity from the horizontal temperature gradient between relatively cool ocean surface and warm land causes the inversion to slope downward toward the coast with enhanced wind speed adjacent to the coast (Nieberger et al. 1961; Baynton et al. 1965; Burk and Thompson 1996). Coastal terrain channels wind leading to further enhancement. However, modeling studies with flat terrain demonstrate the wind is mainly a product of large-scale circulation features and forcing (Burk and Thompson 1996; Hoskins 1996).

1.1.2 Motivation

Wind along the US West coast has been the subject of numerous observational investigations because of its importance for biological and oceanic processes, prominence in the climate system, and threat to human activities. Previous studies have focused on fog and marine stratus formation and dynamics (Fosberg and Schroeder 1966, Klein et al. 1995; Filonczuk et al. 1995, Burk and Thompson 1996, Rogers et al. 1998), radar propagation (Haack and Burk 2001) and radiative properties (Pincus et al. 1997) of the marine boundary layer, air pollution (Dabberdt and Viezee, 1987), and ocean surface and subsurface currents and dynamics (including upwelling of cold, nutrient-rich sub-thermocline water) – (Nelson 1977; Huyer 1983; Beardsley et al. 1987; Miller et al. 1999). In addition, spring and summer winds along the California coast produce wind waves and hazardous conditions (Lovegrove 2003) affecting small craft, coastal and marine structures, commercial, recreational and certain naval operations. More recently, the prospects for offshore wind energy production have gained interest (Yen-Nakafuji 2005).

In the past, observations have been limited to climatologies and measurement campaigns of relatively short duration, relatively poor spatial coverage, or both. Information about the wind more than 30 km offshore is particularly lacking. Routine, fixed point measurements, observational campaigns, and previous satellite studies noted the event-like character of the wind but could not adequately address the spatial structure or evolution of wind events. Now, with more than 6 years of twice daily satellite scatterometer wind estimates at 25 km resolution, it is possible to examine surface wind variability in space and time with unprecedented detail.

The temporal, and to some extent, the spatio-temporal variability of winds along the California coast has been investigated in a number of studies using buoy, land station, and platform or similar fixed point measurements, aircraft flights, soundings and ship observations recorded during measurement campaigns lasting from a few days to two years (Nieberger 1961; Elliot and O'Brien 1977; Caldwell et al.1986; Beardsley et al.1987, Dorman and Winant 1995, Burk and Thompson 1996, Rogers et al.1998; Dorman et al.1999, Edwards et al.2002, and others).

Understanding of the spatial scale of the high wind region along the coast is gleaned from non-synoptic seasonal or monthly averages. Nelson (1977) and Bakun and Nelson (1991) used 100+ years of ship data averaged in 1° x 1° grids to plot monthly mean windstress. Winant and Dorman, 1997 used 50 years of California Cooperative Oceanic Fisheries Investigation (CalCOFI) station observations to produce seasonal mean wind stress with about 65 km horizontal resolution. The CalCOFI sampling is irregular in time but seasonal averages are based on roughly one observation per station per season over 50 years.

Buoy winds along the coast behave in a spatially coherent manner over broad scales of 1000 km or more (Halliwell and Allen 1987). Analysis of hourly wind data from buoys, platforms, and land stations near Pt Conception (Caldwell et al.1986; Dorman and Winant 2000) and Point Arena (Beardsley et al. 1987) indicates that mean coastal conditions include moderate to gale-force northwesterly winds lasting days to weeks interrupted by brief periods (1-6 days) of calm or southerly wind. Enhanced northwesterly winds are characterized as lasting 1-2 days (Halliwell and Allen 1987) up to one week (Huyer 1983; Caldwell et al.1986; Beardsley et al. 1987). Beardsley et al. (1987) also describe northwest wind 7-15 m/s lasting up to 30 days. The discrepancy in the estimated duration of wind events may be attributed to relatively short analysis periods and the qualitative definitions of "enhanced" winds.

Satellite wind estimates have also been used to average wind along the coast over 1-4 months. Dorman et al. 2000 show satellite derived mean winds for June-July 1996, while Edwards et al. 2002 show mean winds for June 1994 and June 1996. Both studies use SSMI passive satellite wind estimates at 0.25° x 0.25° resolution (Wentz, 1997). Perlin et al. 2004, use Quikscat satellite scatterometer (active radar) wind estimates with 25km resolution and depict mean winds for June-September 2000 and 2001. Note that passive satellite wind estimates are obtained via fundamentally different physics relative to active radar scatterometry used in the present study. Passive satellite wind estimates lack directional information and will have different error characteristics. Data and data accuracy will be covered in more detail in the next section.

The extensive catalogue of papers describing winds nearshore the US west coast may unintentionally leave the impression that strong winds are found only along the immediate coast. The offshore region has been largely ignored due to the importance for upwelling at the coast and lack of data farther offshore. However, Huyer (1983) indicates the importance of upwelling farther offshore. Recent research (Chelton et al 2004; Perlin et al 2004) demonstrates the offshore wind field is not smooth and strong winds are not confined to near-coast regions offshore of the US West coast. They find strong gradients in wind speed tied to sea surface temperature gradients hundreds of km offshore of the California and Oregon coasts.

The goal of this paper is a comprehensive examination of temporal variability of coastal wind (from seasonal cycle to event time scale), wind events in both space and time, and the spatio-temporal evolution of wind events along the coast. The motivation is in part fueled by new technology. Satellite scatterometer wind observations allow analysis of the spatial structure of winds with unprecedented detail.

Data are presented below followed by analyses which are broken into three main sub-sections including analysis of the temporal character of buoy winds and the spatio-temporal variability of wind measurement obtained from the satellite scatterometer. The third analysis sub-section covers the mean state of wind events and their evolution in space and time. Concluding remarks are found in section four.

1.2 Data

1.2.1 Buoy Winds

Buoy wind measurements are available from NOAA National Data Buoy Center, or NDBC (http://www.ndbc.noaa.gov). NDBC maintains an archive of about 75 moored buoys in the Northeast Pacific Ocean with over 40 currently in operation. The historical record spans from late 1975 to

present. Eleven buoys were chosen for analysis (Table 1 and Figure 2) based on the duration and continuity of the record. Buoys where diurnal effects dominate variability were not included (e.g. buoy 46025), since diurnal effects are not a focus of this study.

Wind speed is reported hourly based on 8.5 minute averages from anemometers typically located 5 meters above sea level. Anemometers for buoy 46054 and 46023 are located 10 m above sea level. Since the mid-1980's, R.M. Young Model 05103 anemometers have been used (NDBC website http://www.ndbc.noaa.gov/improvements.shtml). Wind speed and wind direction are scalar and vector averages, respectively. Some wind speed data from the 1980's employed vector averaging. Where applicable, these winds were slightly enhanced following Gilhousen, 1987.

NDBC wind accuracy for standard wind observations is listed as 1 m/s and 10 degrees (Hamilton 1980). However, the accuracy may be even better. Gilhousen (1987) performed extensive comparisons of winds from buoys located within approximately 100 km of each other. The standard deviation of wind speed difference was 0.6 to 0.8 m/s for buoys separated by less than 5 km. Scatter plots of wind speed were linear and no bias was evident with wind speed magnitude. The calibration was stable with negligible drift over the lifetime of buoy deployment in several tests. The standard deviation of wind direction differences was 9 to 11 degrees. Gilhousen (1987) also compared results from standard 8.5 minute wind averages to one hour averages. The differences were similar to those obtained between duplicate anemometers on the same platform (i.e. less than 1 m/s and 11 degrees).

For this study, standard meteorological buoy observations were scaled to 10 meters from 5 meters using power law scaling (Hsu et al. 1994, their Figure 5) for near-neutral stability. Air and sea surface temperature differences are generally with 2 degrees in the study region. Errors introduced in scaling are less than 10% in wind speed.

1.2.2 Satellite Scatterometer Winds

Wind speed and direction estimates from the microwave radar scatterometer on board the QuikScat satellite (Liu 2002, Liu and Xie 2001) are available from 20 July 1999 to present. The

satellite was launched in July 1999 and is operated by NASA. QuikScat (QSCAT) data are produced by Remote Sensing Systems and sponsored by the NASA Ocean Vector Winds Science Team. Data are available at http://www.remss.com.

The polar orbiting satellite features a 1600 km swath with two passes, which collectively cover 90% of the globe at 25 km resolution each day. The daily spatial coverage and horizontal resolution are superior to any previous scatterometer missions (Chelton et al. 2004) and offer a significant advantage over sparse in situ measurements from buoys, ships, or short duration intensive observations programs.

Previous publications detail scatterometer physics (Naderi et al. 1991, Liu 2002), QSCAT specifications (Freilich et al. 1994), and instrument accuracy including comparisons with in situ observations (Draper and Long 2002; Ebuchi 2002; Chelton and Freilich 2005). The RSS website above also contains more information. A brief overview relevant to this study is given below.

The QSCAT scatterometer wind estimates are obtained via active microwave radar and are fundamentally different from passive microwave radiometry (e.g. SSM/I instrument, Wentz et al.1997; Mears et al. 2001). Microwave Ku-band (frequency near 14 GHz) pulses transmitted and received at the satellite backscatter from the sea surface. The backscatter signal from the rough sea surface is highly correlated with both wind speed and wind direction. Wind speed and direction are inferred from multiple backscatter cross-section signals with elliptical horizontal dimensions of 25 by 35 km obtained at systematically varying azimuths along the orbital track. Conversion to the equivalent 10-m wind speed assumes a neutrally stratified atmospheric boundary layer (following Liu and Tang 1996, with drag coefficient from Large and Pond 1982) and interpolated onto a 0.25° grid.

Overall accuracy in wind speed and wind direction is 1.5 m/s and 21 degrees (Chelton and Frielich 2005). The accuracy is neither homogeneous nor isotropic across the swath. Accuracy varies by 0.1 m/s and 5 degrees across the swath, independent of wind direction. Wind speed accuracy is 0.75 m/s for wind along the orbital track and 1.5 m/s for wind oriented across the track (Chelton and Frielich 2005). Comparisons with buoys (Ebuchi et al.2002; Draper and Long 2002) indicate a difference in standard deviation of 1.2 m/s and mean bias of 0.11 m/s relative to buoys for wind speeds between 2-18

m/s. For winds from 18-25 m/s the standard error increases to 10%. Buoy measurements of wind events studied in this paper rarely exceed 18 m/s and never reach 20 m/s.

Further error may be attributed to the neutral stability assumption. Chelton and Frielich (2005) found the assumption leads to a mean bias of +0.2 m/s in QSCAT wind speed in the eastern North Pacific Ocean. The overestimate was found in other satellite scatterometer data (Mears et al. 2001) who also attribute the discrepancy to the fact that, on average, the atmospheric boundary layer over the world ocean is slightly unstable. This bias is acceptably small. Even so, this paper focuses on wind speeds generally greater than 5 m/s in spring and summer. Higher wind speed induces neutrality in the atmospheric boundary layer (Hsu et al.1994). The stability assumption seems especially plausible given the wind speeds considered and the lack of dramatic sea to air temperature differences in eastern ocean basins in spring and summer.

QSCAT scatterometer wind estimates feature dense sampling within each swath. However, a sampling rate of just two swaths per day can lead to aliasing of measured winds for processes encompassing relatively small spatial and temporal scales (Schlax et al. 2001). Following Schlax et al 2001, monthly means and composites constructed in this paper have sufficient temporal averaging such that sampling error will not be problematic.

The study region is along the western coast of North America extending offshore to 180°, and from 10° to 45° N (Figures 1 and 2). Backscatter from land received from antenna sidelobes contaminates wind estimates within 30 km of the coast. Satellite wind estimates immediately along the coast (within 30 km) are not a focus of this study. The QSCAT orbit provides twice-daily coverage. Ascending and descending swaths are separated by about 12 hours. Each pass covers the study region in approximately 3 hours (Table 2).

1.3 Analysis

Much of the temporal character of winds can be seen in a simple time series from coastal buoys (Figure 3) and noted in previous studies. Three characteristics readily apparent are seasonal

cycle, persistence, and intermittence in both speed and direction. Also, stronger winds are associated with more persistent wind direction.

Wind along the California coast is frequently greater than 10 m/s for extended times (Figure 3). Winds are generally weaker in winter with intermittent, short duration peak wind episodes while the opposite is true in summer; summer has generally stronger wind with intermittent, short duration drops in wind speed (Huyer 1983; Beardsley et al. 1987). Fluctuations appear more frequently in winter. In all seasons, winds are from the northwest, unless the wind is weak (Nelson 1977; Dorman and Winant 1995). An exception is strong southerly winds in winter associated with land-falling cyclones lasting 1-2 days (Huyer 1983; Dorman and Winant 1995). Such cyclones are quite rare for southern California, but increase in frequency and intensity with latitude (Halliwell and Allen 1987). Peak northwest winds in spring usually last less than 5 days while wind events lasting 1-3 weeks or more tend to occur in late spring through summer (Caldwell et al. 1986, Winant et al.1988). Moderate summer winds blow for extended time up to 30 days without dropping below 5 m/s (Beardsley et al.1987). Finally, interannual variability is also evident in the buoy wind observations (Halliwell and Allen 1987).

1.3.1 Temporal Variability

Buoy Temporal Persistence

Buoy wind observations show remarkable persistence (Nelson 1977). The persistence in wind speed and direction in Figure 3 is representative of wind observed at other buoys along the coast (Figure 4).

Winds are moderately strong with a median speed of roughly 7-10 m/s and predominantly from the northwest for all buoys (Figure 4). For a given buoy, a large majority of winds favor a particular direction. Winds at buoy 46059 (B59) favor 336°-360°, winds at B47 favor 288°-312°, while winds at the other buoys favor 312°-336°. Comparing a buoy's favored direction (Figure 4) with the location map (Figure 2), one can see that winds are aligned with the local orientation of the coast (Halliwell and Allen 1987; Dorman et al.2000). Winds seldom vary from this northwest to southeast

orientation of the coastline. However B59 experiences the most deviation from the northwest. Note that B59 is far offshore and in the storm track and thus experiences the least coastal influence and bears the brunt (and southerly wind) of winter cyclones. The winter cyclone season grows longer farther north as evidenced by the bipolar nature of the wind rose. At B14, for example, strong wind is aligned with the terrain, either from northwest or southeast with a tendency for light easterly winds.

Buoy Seasonal Cycle

The northwesterly wind can be isolated by examining the component of wind speed directed along the dominant wind direction (the mode). The seasonal cycle of these projected winds is shown in (Figure 5). The wind projection along dominant wind direction (DWD) provides an acceptable characterization of buoy wind for analysis because of the remarkable persistence of buoy winds. Substitution of projected winds versus all winds is not universally valid. However, both cases of projected and non-projected (i.e. all winds) are almost identical for buoys B28, B63, B54, and B47. Projected versus all wind cases are quite similar for B12, B59, and B11, but overall and projected winds seasonal histograms differ for B14, B13, and B42. For the last three, the main difference is a concentration of relatively weak winds in fall that do not blow along the DWD. Nevertheless, for spring and summer winds, the substitution is reasonable for all of the above buoys.

Figure 5 reveals interesting features of the seasonal cycle of projected winds. There is a clear seasonal cycle with features that are common across all buoys. Highest wind speeds occur in spring, typically in April but sometimes in May when the entire wind distribution is shifted toward higher speed. Winds are seldom weak from early spring through summer (as opposed to late fall and winter when winds tend to be calm).

Variability is evident from spring through late summer that differs between the northern and southern parts of the domain. Most buoys (B42, B28, B11, B63, B54, B47, and perhaps B13, B12, B59) have highest wind consistency in spring (April-May) and late summer (either Jul-Aug or Aug-Sep). The months with especially high consistency (i.e. relatively high percent of observations per speed and month bin) are in Jul-Aug in northern buoys near the California-Oregon border. However

moderate winds at the southern buoys, from Pt. Conception to the California-Mexico border, are most consistent during Aug-Sep.

From the above sections and Figure 3, it is evident that persistent northwesterly winds in spring and summer are broken up by intermittent, short duration calm periods. The temporal wind pattern can be thought of in terms of wind events. The literature roughly quantifies duration of qualitatively defined wind events. Wind events last 1-2 days (Halliwell and Allen 1987), 2-5 days (Caldwell et al. 1986), and "several days" (Huyer 1983; Winant et al. 1988; Beardsley et al.1987). Beardsley et al. (1987) describe northwesterly winds of 7-15 m/s lasting up to 30 days. However, they also highlight an enhanced northwesterly wind event lasting a week (1-7 June, 1982) in the vicinity of Pt. Arena.

Buoy Temporal Intermittence

A quantitative definition of wind events will be useful for further analysis. Wind events are defined hereafter by threshold exceedance for a given percentage of subsequent observations (Figure 6). The initiation of a wind event occurs when the projected buoy wind speed exceeds the 75th percentile of monthly mean wind speed for the initial hour and 18 of the subsequent 35 hours. A new event cannot be defined until wind speed remains below the 75^{th} percentile for 36 consecutive hours. Events are defined to capture the peaks evident in the time series while preventing overlapping events, yet allowing for wind fluctuation (brief drops in wind speed below the threshold wind) typical of the buoy observations. The events are identified using the time series of winds projected onto the dominant wind direction. The projected winds are used to avoid high southerly wind events due to land-falling cyclones. The 75^{th} percentile wind speed threshold was arbitrarily selected after considering the 85^{th} and 65^{th} percentiles. The statistics of events defined by all three (65^{th}, 75^{th}, and 85th percentile) thresholds are similar. The 75^{th} percentile was chosen because the number, duration, and mean wind speed of events seemed the best (qualitative) fit. Under this definition, the frequency and duration of wind events is shown in Figure 7 for the Pt Arena buoy (B14).

Figure 7 shows that a substantial amount of time is occupied by wind events with duration greater than 5 days. Though synoptic events (1-5 days) are more frequent, events lasting longer than the synoptic time-scale (> 5 days) comprise more than 40% of total time within all wind events (Figure 7, lower panel). Note that, for the given event definition, it is impossible to have more than thirteen, 10-day events in the Apr-Aug season.

1.3.2 Spatio-temporal Variability from Satellite Scatterometer Winds

The QSCAT scatterometer data are available twice daily for (at least) the last 6 years with 25km horizontal resolution and may be used to provide insight into the spatial structure of surface wind. The buoys have excellent temporal resolution (hourly) and sufficient record length (generally 10-20 years) for robust features. Collectively, the buoy measurements hint at spatial coherence. Fortunately, satellite wind measurements are available to determine spatial structure. Scatterometer estimates reveal the spatial extent and seasonal cycle of wind speed, direction and measures of wind persistence and intermittence of northwesterly wind along the US West coast and eastern North Pacific Ocean.

QSCAT spatio-temporal persistence

The QSCAT data also affirm the persistence of wind speed and wind direction seen in the buoy data. From the buoy wind time series (Figure 3), wind roses (Figure 4), projected vs. non-projected wind histograms (Figure 5), northwesterly winds are quite persistent at these locations. For the offshore region, the ratio of vector averaged to scalar averaged winds, or constancy, is a good measure of how frequently winds are along the dominant wind direction (Figure 8). The pattern is similar to that found by Nelson (1977) using 100 years of ship data. Apart from January (winter), wind vector means are nearly the same as the scalar means for the coastal region south of Oregon and extending southwest of the California coast to the trade winds.

South of the San Francisco Bay, the dominant wind direction is from the north-northwest for all months. The mode of wind direction observations at a given grid and for a given month is defined as the dominant wind direction (DWD) for that grid and month.

Figure 8 shows that from spring through summer, winds are from the northwest, rarely deviating from the DWD. The wind is most persistent in July when the entire field has constancy ratio greater than 90% from the California-Oregon border to S. Baja, and above 40% everywhere in the domain. February (not shown) has the least persistence with constancy ratio below 90% everywhere.

In the seasonal cycle, one can clearly see the south-north-south migration of the high persistency region (only 4 of 12 months are shown in Figure 8). The region with constancy >70% starts just below San Francisco in January, moves north to the Oregon border by May, and extends past the Canadian border in July-September, (though >70% remains just offshore from the coast from mid-Oregon northward). Starting in October, the region with constancy ratio greater than 70% moves southward again.

The dominant wind direction along and offshore of the coast is northwesterly, becoming west-southwest only when and where the constancy ratio decreases (e.g. winter near the Oregon coast and the northwest part of the domain).

Monthly mean wind speed and exceedance frequency characteristics

From the constancy figures (Figure 8), monthly mean wind (Figure 9), and threshold exceedance frequency (Figure 10), the windiest region along the west coast of North America extends from central Baja northward to southern Oregon, with highest wind speeds and frequency encompassing the central California coast between the vicinity of Point Conception (just south of Point Conception offshore of southern California) northward to Cape Mendocino in northern California.

Scatterometer wind fields reveal a very broad and persistent northwesterly wind region extending 8 degrees from the coast as seen in monthly mean speed, dominant wind direction, and wind speed frequency exceedance. Highest winds are south of the California-Oregon border. Relatively strong winds are noted between Cape Mendocino (40.5N, 125W) and the San Francisco Bay entrance

(37.5N,123W) and southwest of Pt. Conception (34.5N,120.5W). Winds in the Southern California bight within 1-2 degrees of the coast between Los Angeles (34N, 119W) and the Mexican border (32N,117W) are relatively weak, as previously noted by many (e.g. Dorman et al. 2000).

Strong and persistent wind along the California coast is evident throughout the year, but is especially weak during the period Oct-Jan (Figure 9). The dominant wind direction is north-northwest along California coast and offshore several degrees longitude for all months except Dec-Jan. Monthly mean winds near Pt. Conception are relatively strong and northwesterly in all seasons.

Monthly mean winds greater than 8 m/s are concentrated between Cape Mendocino to just south of Pt Conception; though monthly mean speeds universally decrease from June through August. Beginning in May and continuing through August, the high mean wind region consolidates but still extends from the California-Oregon border to the north and extends south past the US-Mexico border to the south, while extending 8 degrees longitude west of the coast (Figure 9).

Relatively strong mean winds (>9 m/s) along the west coast of North America first appear in March and moderate winds (> 7 m/s) extend from Washington to central Baja with near-uniform magnitude in April. In May and June, a lingering patch of winds greater than 7m/s at Punta Eugenia in central Baja shrinks and finally disappears by July. June has the highest and broadest mean wind speeds. In June, mean winds greater than 9 m/s occur between the California-Oregon border and Pt. Conception and extend 3° longitude west of the coast.

The most dramatic seasonal transitions in monthly mean wind spatial distribution are from February to March and again from August to September. The mean wind region changes shape beginning in September and continuing into October, where the windy region shifts north and moves slightly offshore of Cape Mendocino. November through February is marked by strong west-southwesterly winds west of the Oregon with relatively light northwesterly wind along the coast south of San Francisco.

Monthly mean winds exhibit a clear seasonal cycle, but unlike the monthly constancy maps, the mean winds do no reflect a simple south-north-south migration with the seasons. The only

semblance of such a migration is the development and fading of the high mean wind region off Punta Eugenia in central Baja, Mexico.

There is, however, a seasonal migration of the high wind frequency region. The monthly exceedance fraction, or the fraction of total winds that exceed a given threshold, is computed for three different thresholds, 5 m/s, 7.5 m/s, and 10 m/s. Figure 10 shows the monthly results for the exceedance fraction 7.5 m/s. In a general sense, the region of highest percentage of threshold exceedance frequency moves from south to north from January to July, while growing in magnitude from 40% exceedance to greater than 70%. Peak exceedance greater than 60% extends from Cape Mendocino south to just west of the southern California bight. This peak region diminishes in magnitude and retreats southward from July to December (with the exception of an anomalous shift northward from August to September). During both September and October, the northwest wind region broadens substantially offshore from Cape Mendocino and extends westward from 123W to 134W with speeds over 7.5 m/s. The only other regions to register exceedance percentages greater than 20% are the storm region in upper left, and trade wind region in lower left of Figure 10.

The Pt. Conception region has a high exceedance percent all year, the highest in the entire eastern North Pacific Ocean for 9 months of the year. During June, July, and September, exceedance percentages are slightly greater along the coasts of Oregon and Northern California than at Pt. Conception.

When the exceedance threshold pattern is lowered to 5 m/s (not shown), the overall patterns are roughly the same as the 7.5 m/s threshold patterns. But, the spatial pattern for the 10 m/s threshold (not shown) is very different. Only the region from the CA-Oregon border to just west of the Southern California bight exceeds 10 m/s greater than 30% of the time. The exceedance for 10 m/s exceeds 30% along the coast March-October with little or no migration with seasons.

A clear south-north-south migration from January-December of high wind and wind frequency is evident in constancy and threshold exceedance frequency from scatterometer winds. Spring has the highest northwesterly wind speeds, with intense events of relatively short duration. The highest monthly mean speeds are in June. However, moderate to strong northwesterly winds are most prevalent

in late summer. The mean speeds do not reflect the south-north-south seasonal migration seen in frequency and constancy since the wind speeds in spring are typically greater, especially where constrained by the geometry and topography of the coast (such as at Cape Mendocino). In summer, wind speeds do not reach the same magnitude, but are more frequently moderate to strong when compared with spring. The net effect of these competing influences is observed monthly mean wind speed pattern. It may be more insightful to examine shorter time scales than monthly mean maps.

1.3.3 Wind events, event evolution

Composites of scatterometer wind data demonstrate that wind events identified in buoy time series maintain a spatially coherent structure throughout the duration of the event (Figures 11 and 12). The buoy wind time series (Figure 3) show that intermittent brief periods of low wind are separated by typically much longer duration windy periods. The scatterometer data are used to examine spatial features of wind events determined from buoy time series. Wind events are defined as in Figure 6 and duration statistics shown in Figure 7. Initial wind event times (t=0 hrs) are listed in Table 3. Composites from -1 days before to +4 days after initiation of wind events (t=-24 to t=+96 hrs) are examined.

The most notable feature of the composites is that their spatial extent and coherence is maintained for several days over a surprisingly large area. From inception to dissipation, events maintain their spatial coherence over a very broad spatial scale extending from Northern California to include or connect with the northeast trade wind region (Figure 11). At t=-24, winds are relatively weak along the coast (8 m/s extending 5° longitude from the southern California coast). Winds are below 8 m/s offshore several degrees from the coast heading southwest until they peak in the northeast trade wind region (around 10°N, 180° longitude). At t=+24, winds are greater than 10 m/s immediately at the coast from the California-Oregon border southward to Baja, Mexico and extending out roughly 5° to the west. A region of winds at least 8 m/s continues to extend farther southwest from the coastal peak to connect and pick up with the northeast trades. The peak speeds of the northeast trades increase

and extend farther northeast (Figure 11). After four days (t=+96), a signal is still evident, though wind speed are universally weaker. Winds are generally weaker and less variable between the relatively strong winds along the California coast and the northeast trade wind region (800-2000 km southwest of California). Thus, the spatial coherence of wind events is more easily seen in composites of wind anomalies (Figure 12) than wind fields (Figure 11). At t=+24hrs, winds are at least 0.8 standard deviations above normal in a region extending almost 15° longitude from the coast, and at least 0.4 standard deviations over a full 25° longitude (Figure 12).

Statistical Significance of Wind Event Composites

A montecarlo simulation was run to generate one hundred sets of simulated composites computed as in Figures 11 and 12 for times in Table 3. However, the year value in Table 3 was randomly switched before computing each of the 100 simulated composites, providing a benchmark of random simulated composites with identical statistical sampling (a type of bootstrapping statistical method). Each simulated composite element is constructed from the same number (56) of field maps with the same sequencing (t=-24, t=0, t=+24 hrs, etc.) and similar annual and seasonal representation as the original composite in Figures 11 and 12. At each grid location, the original composite wind anomaly values are ranked relative to the simulated values. Positive wind anomaly data values in Figure 12 are plotted only if their rank is one (1^{st} of 100) relative to the simulated values at a particular grid location (shading). Similarly, negative values are plotted only if their rank is 10 or below (labeled contours, no shading). Other grid values of the original composite (rank 11 to 99) are masked out in Figure 12. This montecarlo analysis of uncertainty suggests the spatial structures in Figure 12 are unlikely to arise by chance.

Another buoy located south of Pt Arena was used to explore the robustness of the composite pattern seen in Figures 11 and 12 based on B14 at Pt Arena. The Pt Conception Buoy, 46063 (B63: 34.25N, 120.66W), is located near Pt Conception and 600 km south-southwest of B14 (39.22N, 123.97W). Wind speeds (not shown) are slightly and universally greater at all composite times for wind field composites based on Pt Conception (B63), relative to Pt Arena (B14). Wind events

identified at B63 are mostly unique. Only 15% of wind events identified at buoy 14 match (within 24 hours) events at B63. Even so, the composite patterns of standardized anomalies for both buoys are very similar for all composite times. The results for B63 support the robustness of the wind event patterns.

1.4 Concluding Remarks

Northwesterly surface wind along the US west coast and eastern North Pacific Ocean has been studied using observational records including 6 years of 25 km resolution satellite scatterometer winds and 20+ years of coastal buoy data. QSCAT satellite scatterometer wind measurements combined with a quantitative definition of wind events allowed examination of the variability and evolution of wind over the eastern North Pacific Ocean with unprecedented detail. The spatial extent, temporal variability, and space-time coherence of wind events over several days could not be determined from spatially limited station observations (e.g. Dorman and Winant 1995), monthly means from satellite or ship reports (e.g. Nelson 1977; Dorman et al. 2000), or intensive observation campaigns (e.g. Beardsley et al. 1987; Rogers et al. 1998). The extensive catalogue of literature describing winds offshore the US west coast may unintentionally leave the impression that strong winds are found only along the immediate coast. The details of large-scale wind events quantified in this paper are an interesting supplement and contrast to observational studies of wind along the US west coast and the relatively smooth offshore winds in model generated fields.

The variability of spring and summer winds over the eastern North Pacific Ocean can be described as a collection of events of duration days to weeks, with frequency 1-4 events per month over spatial scale several degrees in both longitude and latitude. Wind events are prominent among several other climatological features highlighted in sections 3.1 and 3.2 including seasonality, persistence, and intermittence in both speed and direction. In spring and summer, the strongest and most persistent winds in the eastern North Pacific Ocean are concentrated along the California coast between Cape

Mendocino to just south of Point Conception extending west from the coast about 1000km. Winds in the northeast trade wind region are also relatively strong and persistent.

Peak northwesterly winds in spring and summer usually last 1-3 days but wind events lasting 1-2 weeks or more can occur. About 40% of the combined event time is occupied by events lasting longer the synoptic time scale (1-5 days).

Temporal wind events observed at coastal buoys were used as the basis for scatterometer wind field composites created from 56 wind events based on percentile wind speed from an offshore buoy for the April-August seasons between 20 July 1999 to 31 August 2005. From inception to dissipation, events maintain their spatial coherence over a very broad spatial scale extending from Northern California to include or connect with the northeast trade wind region.

Spatially and temporally coherent events lasting days might be related to large-scale forcing from interaction between the thermal low over the southwestern US and eastern North Pacific high pressure system or from sea surface temperature (SST) fronts. Perlin et al. (2004) found enhanced surface winds along strong SST gradients between ambient and recently upwelled sub-thermocline water off the coast of California. Whether upwelled offshore or advected offshore, the cool water comprising the SST fronts lasts several days. But, the composite wind region in Figures 11 and 12 is much broader than the range of advected SST fronts. The mechanism of generating inhomogeneities and relatively strong wind far offshore of the coast identified in Perlin et al. (2004) is unlikely to be the main cause of the composite patterns.

Interaction between the Pacific high and continental thermal low has long been described qualitatively as the general cause of northwest winds along the US west coast (e.g. Huyer, 1983). Shorter, more frequent, and more intense wind events may indicate a relation to passing fronts, while the less frequent, lingering events might be related to adjustments in the strength and position of the thermal low over the desert southwestern US. Spring and summer events appear to coincide with increased winds in the nearby northeast trades, suggesting a large-scale influence which might not be directly related to the thermal low. A future paper will address the large-scale circulation and forcing of northwesterly wind events in the eastern North Pacific Ocean.

Additional studies may focus on implications of the strength, duration, and spatial extent of wind events for the structure and variability of moisture and temperature in the marine boundary layer, offshore oceanic upwelling, and the sea state.

This chapter was written with coauthors and submitted as a journal article whose citation is: Taylor, S.V., D.R. Cayan, N.E. Graham, and K.P. Georgakakos, “Northwesterly surface winds over the eastern North Pacific Ocean in spring and summer”. Journal of Geophysical Research – Atmospheres, *submitted September, 2006*.

CHAPTER TWO

Structure and forcing of northerly surface wind events over the eastern North Pacific Ocean

Abstract

In chapter one, surface wind events with southward direction over the eastern North Pacific Ocean, especially along and offshore of the California coast were defined (section 3.1.3 and Figure 6). Figures 11 and 12 show the evolution in space and time of wind events based on composites of observed winds and wind anomalies derived from satellite microwave scatterometer. This chapter explores the structure, evolution, and seasonal differences of the atmosphere associated with these wind events. New aspects of the research include the use of a quantitative methodology to highlight and analyze the atmospheric circulation associated with wind events using a relatively long record of events. Past analysis has been typically limited to a handful of cases over 1-2 seasons. In this chapter, wind events are explored with a modern, well-established diagnostic dataset (the NCEP Global Reanalysis) and a newly released, high resolution diagnostic dataset (the North American Regional Reanalysis) to examine 200 wind events from 1981-2005. The atmospheric structure during wind events is discussed in the context of modern theories to investigate and formulate hypotheses about the forcing of such events. A cause-and-effect deterministic approach will be employed to enhance understanding of the role of various processes in driving wind events.

2.1 Introduction

The importance of northerly surface wind offshore of the US West Coast for a variety of oceanic and atmospheric processes is hard to overstate. Chapter One, Section 1.2 describes previous studies of winds over the eastern North Pacific and provides citations that are not repeated here. Ocean surface winds over the eastern North Pacific are important for the large-scale wind driven ocean circulation, ocean surface waves and surface mixing, and upwelling and associated biological processes in the California Current system. Northerly surface winds are a key component of the coastal climate of western North America, and profoundly influence basic state variables such as temperature and humidity. Wind along and offshore of the US West Coast influences the properties and stability of the atmospheric marine boundary layer, marine cloud formation, and radiative properties, with feedbacks to and from larger scales.

A discussion of northerly wind events along and offshore the US West Coast is inseparable from the mechanisms that produce the eastern North Pacific surface high and relatively low surface pressure over the western US (Figure 1). As Liu et al. 2004 and Miyasaka and Nakamura 2005 indicate, questions remain regarding formation and maintenance of the spring and summer midlatitude subtropical circulation, in which the northerly surface wind plays a fundamental role.

> However, what is important for the local feedback loop is the alongshore northerly winds associated with the high. The wind cannot be reproduced with its full intensity without fully incorporating the land-sea thermal contrast. Dynamically and thermodynamically, it is the strength of the northerlies that is related to the subsidence, not the strength of the high itself. The formation of maritime stratus depends on the strength of the subsidence and the coolness of the underlying ocean surface, the latter of which is also controlled directly by the strength of the surface northerlies. (Miyasaka and Nakamura 2005)

Thus, a better understanding of the circulation associated with wind events may lead to a better fundamental understanding of the climate system.

2.1.1 Seasonal Mean Atmospheric Circulation from Global Reanalysis

The seasonal mean surface and upper-air atmospheric circulation are discussed because the mean circulation and seasonal differences offer important context in understanding the circulation associated with wind events and their forcing mechanisms. Wind events continue from winter through summer despite large changes in the atmospheric circulation including the intensity and frequency of synoptic systems, mean upper-level wind speed, the meridional atmospheric thermal structure, and the land-sea temperature difference. The fall season has relatively infrequent and generally weak wind events along the US West coast and will not be discussed.

The discussion of the mean circulation begins with the surface pressure before proceeding to higher levels. A surface anticyclone, or high pressure system, can be found over the eastern North Pacific Ocean throughout the year, but varies in strength and position with the seasons (Figure 13). Mean sea level pressure (SLP) over western North America varies more dramatically with the seasons. Cool temperatures and high SLP dominate the northwestern US in winter when the SLP gradient across the West Coast of the US and northerly surface winds along the coast are weak (Figures 9-10). In summer, a thermal low develops over western North America from Mexico northward to the northern Great Basin as temperatures increase over the continent. A gradient between relatively high SLP over the eastern North Pacific and low SLP over the warm continent develops with accompanying climatological wind flowing southward along the US West Coast. In all seasons, the strongest northerly winds along the coast occur near Cape Mendocino (~ 40N, 125W, Figure 14). Seasonally, the strongest mean gradient in SLP across the coast and strongest northerly winds along the coast are in summer.

The seasonal cycle in surface and near-surface temperatures is related to surface pressure. In winter, two high pressure centers are located over the eastern North Pacific Ocean and the western US. A relatively round SLP high over the eastern North Pacific Ocean is located southwest of California and centered at 130W and 30N. Another, stronger, SLP high sits over the western US, centered at 115W 40N, and is a result of the relatively cold winter surface temperatures. In spring, a relatively warm region covers mainland Mexico extending into the southwestern US. The thermal low lies over western

Arizona and the northwest portion of mainland Mexico. A single, elongated, zonal SLP high extends from the west (160W) to the US west coast.

In summer, relatively warm temperatures cover the entire western US and Mexico, with peak temperatures centered on Arizona (110W, 35N). Offshore to the west, a tongue of cool air extends south between 140W-125W. In summer (as with spring), southward flow along the surface pressure isobars and cool air are found along the California coast. The anticyclone over the eastern North Pacific Ocean has greatest mean surface pressure during summer, with a broad region over 1024mb centered at 160W-140W and 37N. The thermal low lies over the Gulf of California.

At 700mb, a ridge in geopotential heights sits above and to the north of each surface anticyclone during winter (Left panel of Figure 13). A weak trough at 700mb sits over the Baja Peninsula. In spring, the flow at 700mb is zonal from the west with troughing at the coast south of the California-Oregon border. The trough over the Baja peninsula is more pronounced in the north-south direction but with weaker gradient than winter, while a ridge remains over northwestern portion of the Rocky Mountain states (e.g. Idaho).

Summer exhibits weak mean zonal flow north of 40N at 700mb with a weak trough centered along Northern California coast and northward (Right panel of Figure 13). South of 40N, two anticyclones are centered at 160W and 100W with weak troughing (relatively low geopotential heights) in between over northern California.

In winter, a ridge is still clear at 500mb over each of the two surface anticyclones (Figure 13). During spring, westerly flow is almost purely zonal with a very weak trough over Southern California. Summer exhibits very weak flow with no contours in the southwest portion of the domain. Even so, a weak trough is evident (along 130W) above the strongest gradient in SLP (between 130W-120W). A region of elevated geopotential heights lies over the southwest US centered on New Mexico (5910m) such that flow over California is from the southwest.

Winter circulation at 250mb (not shown) is similar to that at 500 during each respective season.

2.1.2 Possible mechanisms of wind events: Processes known to affect coastal wind

The annual mean large-scale circulation includes northerly wind along the west coast of North America, though winter circulation does not favor strong northerly wind. In all seasons, there are several physically probable explanations for especially strong winds and wind events to be found along the California coast. Equatorward winds are found at all western continental coasts of the world (e.g Winant et al 1988, Liu, et al 2004). Below processes known to affect coastal equatorward winds are discussed.

Synoptic Systems

The coast itself cannot create wind without external forcing. The surface pressure gradient across the coast and attendant wind change with the passage of synoptic systems. In particular, the North Pacific subtropical high often builds northeastward into the Northwestern US after a cyclone passes to the north of the high, causing a tighter longitudinal gradient across the Northern California coast (as in lower panels of Figure 17) with a strong northerly wind event (Halliwell and Allen 1987).

Low pressure systems passing to the north or over the California coast generate strong winds lasting up to several days. (Even in winter, few storms make landfall south of central California bringing strong southerly wind. These are not considered here).

Dynamic and thermodynamic processes in the upper atmosphere can affect sea level pressure through vertical motion. Upper-level subsidence typically leads to an increase in surface pressure which may strengthen the pressure gradient at the surface, inducing stronger winds. The reverse is true for upper-level lifting.

One particular feature of the upper-level circulation that acts to enhance northerly winds along the West Coast is commonly called a trough or a short-wave. Troughs are equatorward undulations in the eastward flowing upper-level winds. Upper-air troughs create vertical motion that can alter the surface pressure features and, ultimately, surface wind. The sign of the vertical motion can be

diagnosed successfully from the geopotential field with use of quasi-geostrophic theory and some simplifications.

Conservation of quasi-geostrophic vorticity and thermodynamic energy, some reasonable scaling arguments, and geostrophic vorticity and hydrostatic temperature assumptions are employed to obtain the form of the omega equation shown in Equation 1 below. Omega is the vertical velocity in isobaric coordinates. Vertical motion can be determined uniquely from the geopotential field via the omega equation. Holton (1992) employ an additional assumption about the horizontal and vertical behavior of omega to relate omega to Cartesian vertical velocity, w. Holton (1992, p. 166-167) derives:

$$(1) \quad w \propto \frac{f_0}{\sigma}\frac{\partial}{\partial p}\underbrace{\left[\vec{v_g}\cdot\vec{\nabla}\left(\frac{1}{f_0}\nabla^2\Phi + f\right)\right]}_{B} + \underbrace{\frac{1}{\sigma}\nabla^2\left[\vec{v_g}\cdot\vec{\nabla}\left(-\frac{\partial\Phi}{\partial p}\right)\right]}_{C}$$

The Coriolis parameter, f, varies with latitude, while f_0 is the value of the Coriolis parameter at the representative latitude. The static stability parameter in isobaric coordinates is $\sigma = -\alpha\frac{\partial\theta}{\partial p}$, α is the specific volume, Φ is geopotential, and $\vec{v_g}$ is geostrophic velocity.

The omega equation above provides a reasonable approximation of vertical motion tendency and represents the basis of weather prediction for non-convective midlatitude systems in the first operational baroclinic model forecasts made in 1962. Modern weather forecasts employ primitive equation models that do not use the restrictive quasi-geostrophic assumptions and lead to improvements in details of the circulation which are particularly useful for the tropics and convective systems. Nevertheless, the idealized baroclinic model and quasi-geostrophic assumptions can still produce reliable forecasts over a few days for midlatitude systems.

The “B” term is the differential vorticity advection and relates the undulation of the geopothential field to vertical motion. For a short-wave system in an idealized baroclinic model, the

relative vorticity advection is larger than planetary vorticity advection and vertical motion from term B alone is (Holton 1992, P. 168):

$$(2) \quad w \propto \left\{ \frac{\partial}{\partial z} \left[-\overrightarrow{v_g} \cdot \vec{\nabla} \left(\zeta_g + f \right) \right] \right.$$

…where ζ_g is the geostrophic vorticity. The situation is represented schematically in Figure 15. The vorticity is not changing in the y-direction in Figure 15 and the remaining, dominant term of the dot product in equation (2) is the geostrophic advection of vorticity in the x-direction. At the trough (the bottom of the "U" shaped feature between "H" and "L" in Figure 15), the relative vorticity is cyclonic. At the ridge to the far west and far east (the peaks of the undulation to the left of "H" and the right of "L" in Figure15), the relative vorticity is anti-cyclonic. Thus, the geostrophic vorticity advection in the x-direction is positive and there is upper-air descent over the point labeled "H" in Figure 15. The reverse is true above the point labeled "L". The upper-air circulation leads to enhanced pressure at "H" and lower pressure at "L", driving stronger northerly surface wind below the trough axis. If the trough lies above the coast it will produce or augment northerly surface wind along the coast.

In the absence of strong temperature advection from a frontal system (Term "C"), and following the system represented in Figure 15, the effects of troughs are to increase vertical descent and surface pressure to the west of the trough. At the same time, lifting is induced east of trough which typically leads to a reduction in surface pressure. If, for instance, the trough axis were aligned along the coast of California, the trough would produce a stronger surface pressure gradient across the coast and northerly wind along the coast. Thus, northerly coastal winds are enhanced when a trough lies over the coast of California.

Indeed, Beardsley et al (1987) note weak trough passages result in enhanced northerly wind lasting one day near Pt. Arena from the analysis of field campaign data. The authors describe the

surface and upper-level (700mb geopotential height) for two cases studied in spring and early summer of 1982. Halliwell and Allen (1987) also qualitatively described this process and highlight 4 cases in late spring and early summer. Winant et al (1988) note the enhancement of surface winds near Pt. Arena when a trough lies along the California coast during two cases studied - one in May 1982 and the other in July 1982. All of the above authors use data from the 1982-1983 CODE field experiment in their analysis.

Quasi-Stationary Seasonal Circulation Systems and Land-Sea Thermal Contrast

The seasonal change in land surface temperature compared with relatively cool, stable offshore ocean temperatures leads to a strong, near-surface thermal gradient across the US West coast in spring and summer resulting in mean northerly surface flow. The surface anticyclone offshore of the US West coast builds from winter through summer when a thermal low pressure system develops onshore, as indicated in Figure 13. Northerly wind between the two surface pressure systems is sensitive to the pressure gradient between them. In may then be possible for an increase in the thermal contrast on sub-seasonal time-scales to play a role in the forcing of wind events. The thermal contrast and other processes that affect the position and intensity of the quasi-stationary surface pressure systems may also affect the coastal wind.

As the land heats up in summer, a thermal low develops from thermal expansion principles represented in the ideal gas law. Relatively low pressure over the western continent and high pressure offshore would lead to a large-scale thermally direct circulation. Through geostrophy, however, the result is the observed equatorward mean surface wind (Figure 1). The frequency and intensity of cyclones decreases in late spring and cyclones pass far to the north during summer.

Halliwell and Allen (1987) distinguish between spring and summer for the character of large-scale circulation patterns and coastal wind forcing, noting the decline in cyclone activity as cyclones and fronts weaken and move farther north with the advance of summer. In spring, coastal wind fluctuations are driven mainly by propagating cyclones which intensify the pressure gradient across the US west coast between the cyclone and the anticyclone.

The anticyclone over the eastern North Pacific Ocean and the continental thermal low in Figure 13 strengthen and become quasi-stationary as they are seldom perturbed by cyclones in summer. Wind fluctuations are influenced by the variability in the pressure gradient between these two relatively stationary pressure systems. Halliwell and Allen (1987) suggest that troughs, though weaker in summer, still play a role in wind events. Alternatively, they also qualitatively describe "quiet periods" in summer when cyclones are not evident in the SLP field and the high builds far to the north of California. During these "quiet periods", wind events along the northern California coast result from oscillations in the strength and position of the subtropical high and thermal low (Halliwell and Allen 1987).

Any process that causes the anticyclone and pressure gradient force between it and the inland thermal low to migrate or intensify can cause strong wind. But what causes the high and the pressure gradient force across the coast (directed onshore) to move or intensify? Surprisingly, the formation, intensity, and maintenance of the surface high pressure over the eastern ocean basins during spring and summer remains an unresolved scientific issue. Surface high pressure over the eastern ocean basin is stronger during summer in the northern hemisphere (e.g. Figure 13 for the North Pacific), yet the meridional Hadley circulation yields weaker subtropical subsidence in the summer hemisphere (Lindzen and Hou 1988; Rodwell and Hoskins 2001).

Recent papers challenge the notion that convective heating in the mid to upper troposphere associated with Asian Monsoon circulation is the main forcing for creation and maintenance of the subtropical high pressure system in the North Pacific and North Atlantic Oceans. This previously dominant theory was posited by Hoskins (1996) and others. Instead, model experiments by Liu et al (2004) and Miyasaka and Nakamura (2005) suggest that the main forcing is low-level non-convective heating and cooling resulting in a stronger thermal contrast at the western subtropical continental coasts.

Miyasaka and Nakamura (2005) use a global, nonlinear primitive equation model with simplified physics. Key aspects of the model are described in detail in Hoskins and Rodwell (1995). In their model sensitivity tests, observed global diabatic heating based on NCEP/DOE Reanalysis-2 fields from 1979-1998 (Kanamitsu et al 2002) is applied in various horizontal and vertical domains under

perpetual July scenarios. Using only the local lower-level (below ~700mb) heating contrast between the eastern North Pacific Ocean and the Western US, the model results produce a zonally asymmetric surface high pressure system with a magnitude about 70% the observed SLP under mean July conditions. Conversely, use of tropical, upper-level (> 700mb) convective heating produces a SLP high with magnitude only 15% of the observed SLP under mean July conditions.

Results of sensitivity experiments led Miyasaka and Nakamura (2005) to propose a conceptual framework for the forcing and maintenance of the SLP high pressure in spring and summer which is summarized schematically in Figure 16. Radiative cooling over the eastern ocean basin induces lower-level subsidence and anticyclonic circulation. Similarly, sensible heating over the western portion of North America induces cyclonic circulation. The resulting along-shore northerly winds advect positive planetary vorticity at low levels which is balanced by enhanced lower-level subsidence over the northerly winds. Northerly winds also reinforce the circulation through evaporation, cold advection, and cool sea surface temperatures offshore which helps to maintain a strong, stable marine layer. The marine stratocumulus and fog completes the feedback loop by reinforcing radiative cooling over the eastern portion of the SLP high. The mechanisms and details of the system may be important for understanding the cause and variability of the wind events identified in Chapter One. The thermal contrast induces northerly wind along the coast which is a key part of the feedback loop that causes and maintains the high surface pressure over the eastern North Pacific.

Though feedbacks complicate a direct interpretation of cause and effect, the cross-shore temperature gradient in the lower atmosphere during summer is clearly an important influence on northerly wind along the coast. Further, it is evident that any process that affects the position or intensity of the quasi-stationary surface pressure systems (i.e. the eastern North Pacific High and continental thermal low) will affect the northerly surface wind between them.

Interaction between complex geometry and topography of the US West Coast and marine boundary layer (MBL)

Coastal topography along the California coast acts as a barrier to low-level flow, directing it parallel to the coast. Flow with a northerly component, however small, is channeled southward along coast (as discussed by many e.g. Haack and Burk 2001) leading to relatively strong and persistent northerly wind. The California coast between Cape Mendocino and Point Conception is especially prone to channeling because the coastal terrain is relatively high (Figure 14).

Winds immediately near the coast can be especially strong when the marine boundary layer (MBL) lies below the elevation of costal ranges, which is often the case (Filocznuk 1995). The MBL is defined by a vertical temperature inversion that acts to suppress vertical motion and increases the channeling of northerly surface winds. Winant et al (1988) describe a terrain-marine boundary layer interaction affecting coastal wind. Minor obstructions to meridional surface flow such as points and capes protruding along the mostly straight coastline produce gravity waves on the inversion surface. The speed of gravity waves emanating from the source increases with inversion strength.

$$(3) \qquad C = \sqrt{g'h}\,, \text{ and } g' = g\frac{\Delta\theta}{\theta}$$

Where h is the height of the temperature inversion (roughly the height at the middle of the inversion), and $\Delta\theta$ is the change in temperature across the inversion. The potential temperature at the base of the temperature inversion, θ, is related to density of the atmosphere. Waves are supported at the inversion layer when the vertical density gradient of the inversion is sufficiently large. The Froude number is upstream flow velocity (i.e. wind speed) divided by the gravity wave speed: Fr = $\frac{V}{\sqrt{g'h}}$.

For supercritical flow (Fr > 1), gravity waves are too slow to travel upstream and are carried downstream with the flow forming a Prandtl-Meyer expansion fan (Freeman 1950). The material surface height lowers and the flow speed accelerates and turns toward the coast through the expansion fan. A hydraulic jump occurs where flow in the expansion fan once again encounters the coastal barrier. Flow decelerates and the inversion height increases at the hydraulic jump. Prominent coastal

features like Pt. Sur at the southern end of Monterey Bay (Figure 14), and Pt. Conception protrude into the mean flow and are likely sources for gravity waves.

Prandtl-Meyer expansion fans have been observed down-flow of coastal promontories along the California coast (Dorman et al 1999). During the Coastal Waves 1996 experiment (Rogers et al., 1998), aircraft wind and boundary layer LIDAR observations were taken in an expansion fan immediately south of Cape Mendocino (North of San Francisco at roughly 40 N) and another at Pt. Sur. Expansion fans are more common in spring and summer when mean northerly winds and a strong lower atmospheric temperature inversion are present along the coast. In winter, cold fronts with strong, unstable northwest winds destroy the inversion and allow winds to pass over coastal ranges. The typical accelerated wind region associated with expansion fans extends less than 200km from the coast.

Edwards et al (2002) suggest that the prominent eastward bend in the orientation of the coast of roughly 30 degrees south of 40N can instigate a dynamical response, amplifying downstream wind speed over 100's of km. The authors use satellite wind estimates, buoy, and aircraft observations along with theoretical considerations to suggest that the bend in the coast at Cape Mendocino can produce a giant expansion fan extending to the south. The authors find amplified, vertically thin supercritical flow southwest of the California coast in a few cases. The speed and horizontal dimensions of the amplified wind region depends on the direction of the large-scale pressure gradient force and the strength, depth, and stability characteristics of the MBL (whether or not the flow region is supercritical). The horizontal distribution of amplified wind speed is less than 1000 km in latitude and a few hundred kilometers in longitude.

Cui et al (1998) found abrupt changes in the magnitude of coast-parallel flow depending on the large-scale background flow direction in experiments using a fully nonlinear, primitive equation hydrostatic numerical model run at 4-km horizontal grid resolution. Although their model domain covered only Central California and did not include the large change in coastal orientation near Cape Mendocin, Cui et al's results indicate that the complex geometry and topography of the coast can alter the magnitude and spatial extent of winds in a non-linear fashion for 100km or more offshore.

2.1.3 Organization

Section 2.2 and Section 2.3 will cover data and methodology. Results appear in Section 2.4 where the processes known to affect coastal wind are investigated for a possible role in driving wind events. The structure, evolution and seasonality of northerly wind events will be revealed through the analysis. The Discussion Section (2.5) addresses unresolved issues and proposes a new hypothesis. Conclusions are summarized in the final section (2.6).

2.2 Data

NDBC buoy data are described in Chapter One, Section 1.2.1. QuikScat microwave satellite wind data are described in Chapter One, Section 1.2.2.

2.2.1 NCEP-NCAR Global Reanalysis (R-1)

Global Reanalysis fields of operational weather forecasts (Kalnay et al 1996, Kistler et al 2001) from the National Center of Environmental Prediction (NCEP) were obtained from http://dss.ucar.edu/pub/reanalysis/. Sea Level Pressure, omega, U-wind, V-wind, surface temperature and geopotential height data are available at 6-hourly intervals with 2.5 degree latitude-longitude spacing from 1948-present. The NCEP reanalysis fields are obtained through processing historical surface and upper-air data in a dynamically consistent atmospheric numerical weather prediction model. The reanalysis fields are produced in much the same way that routine, real-time global analysis fields are produced. Assimilation of raw atmospheric data, processing and interpolation occur under a universally consistent scheme designed to eliminate artificial jumps in the climatic record associated with changes in data retrieval and assimilation techniques. The process begins with a first guess model

6-hour forecast from the previous post-process analysis combined and optimally interpolated with contemporaneous observations (e.g. rawinsonde, land surface station, ship reports, etc.). This new analysis updates the model before producing the next 6-hour forecast and the cycle continues. The T62 global spectral forecast model includes 28 levels with 5 in the boundary layer. The model is nearly identical to the NCEP Medium Range Forecast (MRF) operational forecast system implemented in 1994. A description of the model is detailed in "Documentation of the Research Version of the NMC Medium Range Forecasting Model" (NMC 1988) and summarized in Kanamitsu (1989). NCEP ranks the reliability of each variable from "A" (the most reliable) to "D" (the least reliable). Level "A" variables are the most influenced by actual observations and are the most reliable. Observations directly affect the value of level "B" variables, though model dynamics also exert an influence. SLP, upper-air U-wind, V-wind, temperature, and geopotential height are level "A" level products, while surface wind (U10, V10), surface temperature, and omega are level "B" products. NCEP global Reanalysis fields have been used in well over a thousand publications in peer-review journals.

2.2.2 North American Regional Reanalysis (NARR)

NCEP repeated the reanalysis process for a nested, higher resolution domain over North America using the NCEP-DOE Global Reanalysis (Kanamitsu et al 2002) as boundary forcing (Mesinger et al 2006). The North American Regional Reanalysis (NARR) uses the NCEP Eta Model (Mesinger 2000) with 32km horizontal resolution and 45 layers in the vertical. The Regional Data Assimilation System (Rogers et al 2001) assimilates precipitation along with other variables leading to improvements in the accuracy of temperature and winds. The improvements are measured by RMS error fits to rawinsonde observations and surface data (Mesinger et al. 2005). Although the regional reanalysis were recently released, a set of studies that employ the fields have been published (Mesinger et al. 2005, Mo et al. 2005, Mo and Cheliah 2006; Ruiz-Barradas and Nigam 2006). The data are available from: http://nomads.ncdc.noaa.gov/#narr_datasets. More information can be found at the following websites, including presentations from users workshops:

http://www.cdc.noaa.gov/cdc/data.narr.html

2.3 Methods

The general approach is deterministic in that the data are explored to find evidence supporting or contradicting the feasibility of proposed wind event mechanisms. Specific techniques are discussed in this section.

2.3.1 Composites

Composites are averages of fields or anomaly fields from a prescribed set of cases. In this analysis, the cases are based on the exceedance of a threshold for projected wind speed at Point Arena (B14) as described in Figure 6 of Chapter 1. Wind speed is projected onto the dominant wind direction before determining threshold exceedance. Use of projected winds eliminates the possibility that events with strong southerly winds will be included in the composite. The dates of events for each season are shown in Table 4.

Standardized anomalies are computed using a 30-day running mean and standard deviation for each 6hr interval separately to ensure removal of both the monthly and diurnal cycles.

2.3.2 Self Organizing Maps (SOM)

SOM analysis is a method for classification, pattern recognition, and feature extraction from large, complex data sets (developed by T. Kohonen. Kohonen 1982, 1989). SOM analysis has been used extensively in a number of disciplines. Oja et al (2003) and Kaski (1998) contain bibliographies of SOM applications. Hewitson and Crane (1994) pioneered the application in climate sciences and provide both excellent description and example of how SOM analysis can be used effectively in the atmospheric sciences (Hewitson and Crane 2000). Cavazos et al 2000 provides another thorough

description of SOM applied to understand mechanisms of extreme precipitation and Liu et al 2006 provides more references and an overview of applications in meteorology and oceanography. More information on the theory and methodology can be found in Kohonen (2001). The software package (Kohonen et al 1995) including codes and documentation is available online at: http://www.cis.hut.fi/research/som_lvq_pak.shtml

The process is analogous to stretching an elastic surface over a cloud of observations. The surface is fixed by a number of nodes specified by the user which define the dimension of the output. The SOM, however, determines the locations of the nodes through an iterative, unsupervised process. At each iteration, the SOM adjusts the position of the nodes in proportion to their distance relative to the data space as determined by a Euclidean measure. The node positions are adjusted during each iteration until the nodes converge to fixed locations.

The process starts by setting the distribution of nodes. Two methods are available for initialization. The linear initialization was chosen for SOM analysis in this application, though a random initialization was also tested and produced similar results in these particular cases. The linear initialization produces reference vectors ordered along a two-dimensional subspace spanned by the two principal eigenvectors of the input data vectors.

For each data record (one record can span a subset of the data space, such as a time series for a given location or a spatial map at a given time), the SOM computes a measure of the similarity between the data record and each node reference vector. The input vectors were the combined fields specified (e.g. SLP and 500hgt). The SOM finds significant features that characterize both maps in combination (somewhat similar to a joint principle component analysis, however, unlike the principle components, the SOM nodes are not orthogonal).

The 'winning' node, c_k minimizes the Euclidean measure:

$$c = \sqrt{\sum_i (x - m_i)^2}$$

where

x = input data vector (e.g. one SLP and 500mb height field pair)

m_i = reference vectors

i = node in reference vector

The reference vector tracks the location of each data point with respect to a given node. Thus x is mapped onto the node c_k, relative to the parameter values m_i. The 'winning' node is adjusted to reduce the difference with the input vector. The reduction is a user-defined learning rate and can be fixed or decrease in magnitude with each iteration. For cases in this study, the radius of the learning function is set to the larger of the two horizontal dimensions of the data space and the radius decreased linearly with each iteration.

The positions of all other nodes in the data space are adjusted in inverse proportion to their distance from the 'winning' node. The adjustment is based on a neighborhood function, the size and shape of which is also a user-determined parameter. For this study, a Gaussian neighborhood function was chosen with default width and magnitude.

The width and magnitude of the neighborhood function also decreases with each iteration. The learning rule for the ‘winning’ node may be expressed as

$$m_i(t+1) = m_i(t) + \alpha(t) \cdot \varepsilon(t)\left[x(t) - m_i(t)\right]$$

$\alpha(t)$ = learning rate

$\varepsilon(t)$ = neighborhood function

where t denotes the current learning iteration and x represents the currently presented input vector. Convergence is achieved after multiple iterations. Fewer SOM nodes are eventually placed where data are sparse, while more in data dense regions allowing for representation of non-linear behavior and subtle details with relatively few nodes.

The final output is the ordered set of nodes. Nodes with similar representation of the data space are mapped close together (the self-organizing "map"). Dissimilar nodes are further apart. It

should be noted that the degree of similarity or dissimilarity in representation of the data space between neighboring nodes is not constant. Adjacent nodes are more closely related than non-adjacent nodes but the degree of similarity or difference is not constant from one pair of adjacent node to the next. (For example, in Figure 24, node (0,1) does not necessarily have the same degree of similarity to both nodes (0,0) and (2,0)).

Before the SOM analysis is run, the user must define the size and shape of the SOM array (e.g. 12 total nodes arranged 3x4). The chosen number of nodes affect the degree of generality or detail and must be chosen a priori. If the SOM array is relatively small, for instance, a dominant pattern may appear in just one node. However, subtle variations of the dominant pattern may be reflected in two or more nodes for a larger SOM array. The SOM was run with twelve and eight nodes but it was found that six or less basic patterns were represented. Therefore, six nodes where chosen for Figures 21-25.

For a given set of learning and neighborhood parameters, the best map will have the smallest average quantization error. The average quantization error is the average of all the individual minimum Euclidean measures of each node.

The node patterns in the SOM for all fields were robust and fairly insensitive to adjustments in the parameters $\alpha(t)$ and $\varepsilon(t)$. The character of basic node patterns did not change noticeably for small variations of $\alpha(t)$ and $\varepsilon(t)$.

The nearest node to each composite time was computed and the frequency of occurrence of each node (i.e. the percent of input composite fields mapping to the specified node) appears on each node map.

2.3.3 Composite Stability and SOM Analysis

The stability of composite patterns is verified by computing the composite mean over different temporal subsets of all events. For instance, the composite of SLP and 500mb heights using as little as three years of seasonal data produce a pattern remarkably similar to the corresponding composite with 25 years of data. Composites were computed and inspected for subsets of 20 maps of individual times

for each season and field (not shown). The resulting subset averages showed good agreement with each other and the full composite for nearly all fields and seasons. Minor differences with the overall composite were found in only one subset for lag+1 700mb height anomalies in spring, one subset of lag-1 500mb height anomalies in all seasons, and with warm anomalies in summer 925mb level temperatures. Summer 925mb temperatures did, however, consistently place the cool anomaly in the Pacific Northwest. Such differences in the composite pattern of the subsets could possibly be related to the ENSO cycle, but this was not investigated.

Even over a relatively small subset of wind events, there may be a variety of recurring patterns. The Self Organizing Map technique is used to highlight distinct patterns or subtle variations of the same pattern that comprise the overall composite. The purpose of SOM analysis is to identify distinct patterns that merit further review or imply physical explanations of the composite structure.

2.3.4 Case studies

Global Reanalysis with 2.5° x 2.5° resolution is fairly coarse to represent the timing and spatial details of meso-scale features such as weak, mid-level shortwarves passing in summer. Wind events are highlighted in case studies with higher resolution NARR data. The data are described in the data section. Case studies are a subset of the composite times in Table 4 selected on the basis of SOM nodes of composites of wind events. For instance, two case studies in winter are selected from wind event dates corresponding to the most common joint SOM node pattern for SLP/500mb heights. Likewise, spring case studies correspond to the first and second most common SOM node. For summer cases, a variety of nodes are represented. All cases are chosen without prior inspection of the wind field for the date in question. The SOM nodes for each case can be cross-referenced in Table 5.

NARR surface wind (arrows and magnitude), SLP and upper air heights and temperatures at 925mb, 700mb, 500mb, and 300mb levels of the atmosphere are shown for each case. The height of the 925mb level varies seasonally between 600-1000 meters over the domain tending to increase with surface temperatures. Wind events typically last four days with peak winds approximately 24 hours

after initiation. The dates shown in the sensitivity test figures are chosen to roughly coincide with the peak of the wind event. Where available, QuikScat satellite derived wind measurements are also shown.

2.4 Results

Processes known to affect coastal wind including troughs, the thermal contrast, and terrain-marine boundary layer interactions are investigated as possible mechanisms of northerly wind events described in Chapter One. Evidence of the mechanisms are explored though the data. During the fall season, mean northerly winds are at the annual minimum as are the number of wind events because both of the main mechanisms, troughs and the thermal contrast across the coast, are relatively weak. Thus, the fall season is not considered in this analysis.

2.4.1 Composites of NCEP global Reanalysis Fields

Seasonal composites are used to explore evidence of troughs along the coast during wind events. Wind measured at a central California coast buoy (46014 -Pt Arena) is used as the basis of composites of Global NCEP Reanalysis fields described in the data section this chapter. The large-scale surface and upper-level circulation associated with conditions preceding and during wind events in each season is highlighted using NCEP Global Renalysis fields. In the first chapter, the number of events was limited to the range of available QuikScat data (1999-2005). Here, the full record from Buoy 14 south of Cape Mendocino (Figure 2) was used and two hundred wind events are identified and categorized in 3 two-month seasons (Jan-Feb, Apr-May, Jul-Aug) using hourly buoy data from 1981-2005. Wind events are defined as in Chapter One (Figure 6) and the new dates of the 200 events are listed in Table 4.

Wind events account for an appreciable proportion of each two-month season. Three wind events on average occur during each season, with each event typically lasting four days. Thus, wind events are present about 20% of the time during each two-month season. Composites of fields and anomalies for peak wind periods at buoy 46014 of sea level pressure, 925 millibars (mb) temperature, and geopotential height at 700mb, 500mb, and 250mb pressure levels were created in order to examine the large-scale circulation associated with wind events. Evidence that troughs, the thermal contrast across the coast, and terrain effects may influence wind events in each season is evaluated

2.4.2 Evidence of Upper-air Troughs During Wind Events

Composites of Global Reanlaysis data and case studies using the NARR data indicate that troughs in the upper-air circulation are almost always associated with wind events (Figures 17 and 18). As shown in the 500mb composite features, the northerly wind events in all seasons develop as a trough deepens with lower geopotential height extending farther south in a larger amplitude undulation along the coast during the lag+1 composite (i.e. t = +24hrs). In all seasons, the ridge at 500mb over the offshore surface anticyclone strengthens and/or shifts east toward the coast. The upper trough deepens in magnitude along the coast and extends farther south at lag+1 relative to the seasonal mean.

Composite fields and composite anomalies indicate approaching upper disturbances that move onshore, when surface wind increases significantly (Figures 11 and 12).

From lag-1 day to lag+1 day (Figure 17), an offshore disturbance moves toward the coast to eventually lie just onshore, strengthening the anticyclone offshore and cyclonic low onshore. Figure 18 shows the characteristic dipole of positive and negative co-located surface and upper air patterns resulting from the trough.

The signal from the troughs extends vertically through the atmosphere and are seen as broad, round positive-negative dipole anomalies in composites of winter and spring wind events. Within the respective season, the composite of geopotential height anomalies maintain the same

characteristic patterns at 700mb, 500mb, and 250mb (not all shown). The patterns at 500 and 250mb are particularly similar.

In winter, troughing along the coast represents a dramatic departure from mean conditions (Figure 13) where high pressure normally dominates the entire Western US. A strong trough dipping under the California-Mexico border with steep gradient can be seen, in conjunction with a dipole of anomalous anticyclonic and cyclonic circulation (Figure 22). In spring and summer, however, the mean circulation favors alongshore northerly wind at the US west coast with slight troughing above. In spring, the negative anomaly over land at 500mb is northwest of the surface signal (Figure 18). The offset between surface and upper anomalies is even more pronounced in summer. This feature of the summer pattern will be discussed more later. Spring and summer signals (0.35-0.65 σ) are relatively weak, while winter signal remains strong (~ 0.65-0.95 σ).

Strong troughs along the US West coast associated with wind events can be seen in case studies with higher resolution NARR data. Deep troughs (both in intensity and vertical extent) are positioned above or immediately to the east of the coast in the eight of eleven cases examined. The troughs are characterized by a clear undulation of packed horizontal isopleths indicating the steepness of the meridional gradient on the height surface that dips to the south, which typically, but not always, returns north to form a U-like feature with relatively cold air on the north side of the gradient.

The upper trough is dynamically connected, through vertical motion, with high surface pressure to the west and low surface pressure to the east such that northerly winds are present at the surface (Introduction sub-section 2.1.4).

Clear, strong troughs are evident in two winter case studies for 16Jan1991 (Appendix Figure A1) and 14Feb1997 (not shown). Indeed, both winter events are accompanied by a powerful wind event observed at the surface. For the winter cases, there is no indication of thermally induced low pressure at the surface.

In addition, a strong upper trough is evident at 700mb, 500mb, and 300mb on 18May2000 (Figure 19), 27Aug2002 (Appendix Figure A5), 22Aug2002 (Appendix Figure A6), 02May2001 (not shown), and during 26-28May1982 (Appendix Figures A2-A4). The troughs are all co-located in the

X-Y plane (vertically consistent). On 03Jul2000 (Figure 19), the upper trough is most evident at 700mb.

There are a few exceptions during summer. Three highlighted cases of wind events in summer indicate weak or barely perceptible troughs at 700mb with unusual anomaly patterns relative to winter and spring. The magnitude of winds during wind events is generally smaller in summer than spring, so weaker troughs might be expected. Weak troughs during summer and these particular cases will be discussed more in the discussion section of this chapter (Section 5).

2.4.3 Evidence of Near-Surface Thermal Contrast across the Coast during Wind Events

Modeling results from Liu et al (2005), Wang et al (2005), and Miyasaka and Nakamura (2005) suggest a low-level thermal contrast across the coast is mainly responsible for forcing and maintaining the surface anticyclone and equatorward wind over the eastern ocean basins. Simple physics of the atmosphere and geostrophy also predict southward flow along western continental coasts (Intro Section 2.1.2). Below, evidence regarding the role of near-surface thermal contrast across the western continental coast during wind events is examined using Global Reanalysis and NARR fields.

As the western continent of North America warms with the onset of spring, the ocean remains relatively cool setting up a large temperature gradient across the coast with a thermal low over the desert southwest (middle and right panels of Figure 13). The strongest temperature gradient across the US West Coast is in summer (right panel of Figure 13) and the strongest mean winds are in summer (Figures 9 and 10).

Evidence of a thermal effect relating to wind events may be found in the composites, self organizing map (SOM) nodes of composite maps, and case studies of wind events. Self organizing map analysis is a feature extraction technique used to highlight distinct patterns or subtle variations of the same pattern that comprise the overall composite. More information on SOM analysis can be found in the methods section of this chapter (Section 2.3).

The subtropical anticyclone moves offshore and occupies the eastern North Pacific Ocean leading to northerly surface flow (Figures 13 and 20). Spring composites of wind events (middle panel of Figure 17) indicate a deeper thermal low over northwest mainland Mexico and southwest US (12mb down to 8mb) with only slightly enhanced offshore high (2mb). The asymmetrical change in surface pressure and increased temperatures over land suggest a thermal forcing.

Also in spring, SOM node (1,0) for 925mb temperatures at lag -1 (Figure 21) shows a warm anomaly over the southwestern US ahead of a wind event, and two other nodes ((2,0); (2,1)) show warming over the continent and offshore of Southern California (extending far offshore).

Case studies of individual wind events using higher resolution NARR fields may also suggest some influence of temperature contrast on wind events. A strong surface wind event occurred in late May, 1982 (Appendix Figures A2-A4), which provides a good example of a thermal low during an especially strong wind event. On May 26, 1982, a deep, warm low pressure region covers the Western US. SLP is relatively low in Northern California where the pressure is 1004 unusually close to the coast. A 1036mb high sits offshore at 140W, 45N. While surface winds are strong, the Pacific Northwest US states are relatively warm. Temperatures at 925mb are unusually warm over Northern California just east of the maximum wind region. As the upper trough moves onshore bringing very cold air into the Pacific Northwest, the surface winds along the coast decrease (Appendix Figures A2-A4). The SLP rises in Northern California to 1012mb (up from 1004mb), while temperatures drop precipitously (from over 283K in Northern California in Appendix Figure A2 to less than 267K in the right panel of Figure A4). A similar evolution occurs on 28Jul2001 (Appendix Figure A7).

High winds tend to correspond to the strongest temperature gradient at 925mb. During summer, the strongest surface winds are found in the immediate vicinity of the strongest temperature gradient at 925mb on 22Aug2002 (Appendix Figure A6), 18Aug2002 (Appendix Figure A8), and 06Aug1994 (not shown).

Along with several suggestive case studies, there are counter examples and evidence against a strong, or consistent thermal relationship with wind events on the time-scales considered. In winter, clearly the land is very cold and there is no thermal effect to lead to northerly wind (Left panel of

Figure 17). During and immediately before wind events, 925mb temperatures are actually above the mean over the southwestern portion of North America in only about 25% of SOM nodes during spring and summer. None of the preceding (lag-1) SOM nodes for summer 925 temperature anomalies (not shown) show a warm anomaly over land. Only one node (2,1) for the lag+1 anomalies shows anomalously warm 925 temps over land (not shown). In all seasons, 925 air temperatures during wind events (Figure 20) have a common feature: a cool anomaly in the region where the SLP anomaly pattern favors northerly flow. This feature, typically in the Pacific Northwest, indicates cold temperature advection.

If a thermally induced low pressure were responsible for stronger northerly coastal wind, one would expect lower surface pressure and higher temperatures at 925mb to accompany a wind event. Instead, anomalous decrease in SLP and temperature east of the northerly surface flow likely indicates the passage of a short-wave, suggesting that falling pressure over the continent is due to the synoptic system (a storm). In summer, lag+1 temperatures cool slightly during wind events (Right panel of Figure 20) and SLP drops from 1012mb to 1010mb over the northern Sea of Cortez. Offshore high pressure increases slightly possibly indicating a short-wave moved through into the southwest US. A decrease in temperature and SLP is not what one would expect if a warm-core thermal low were responsible for enhancing northerly surface winds along the coast.

The limited evidence supporting and detracting from a link between the thermal contrast and wind events leaves an unclear picture of the effects of the low-level thermal contrast on wind events over the time scales considered. It is clear, however, that low-level thermal contrast is not necessary to cause all of the observed wind events.

2.4.4 Effect on Wind events of Terrain-Marine Boundary Layer (MBL) Interaction

The spatial scale of known terrain-marine boundary layer interaction processes along the US West Coast is too limited to produce the majority of wind events indicated in the wind event composites and cases highlighted with NARR fields. Seasonal mean surface wind field (Figure 9) indicates that

strong winds are tied to the Northern and Central California coast of western North America. The persistence of northwest wind along the California coast relative to surrounding longitudes suggests that terrain effects play an important role in wind events over the eastern North Pacific Ocean. The terrain may simply channel winds near the surface or there may be more complex dynamic marine boundary layer effects as discussed in the Introduction sub-section 2.1.2. However, the spatial extent of surface wind speed during wind events as seen in composite field and anomalies (Figures 11 and 12) is much greater than the extent of high mean winds along the coast of California, indicating that wind events are not a simple enhancement of mean conditions.

Occasionally, the large-scale flow is relatively moderate but satellite measurement reveals small-scale variable structure of high and low winds embedded in larger-scale flow. This phenomenon is attributed to the existence of Prandtl-Meyer expansion fans. Winant et al (1988) used observations from a field campaign to contrast the corresponding synoptic scenario ("pattern 3" in their Figure 3) with the broad uniform, non-supercritical flow which includes a relatively deep MBL ("pattern 2" in their Figure 3). Halliwell and Allen (1987) and Beardsley et al (1987) also describe marine boundary layer processes that enhance winds occurring along the California coast. Expansion fan processes have been confirmed through intensive observation campaigns (e.g. Rogers et al 1996). When expansion fans are present along the coast, models typically fail to capture the spatial variability and tend to underestimate the intensity of wind speed. Edwards et al (2002) describe a larger-scale expansion fan effect created by the bend in orientation of the California coast at Pt. Arena and supercritical flow conditions downstream (Introduction sub-section 2.1.2).

However, the expansion fans described in Winant et al (1988), Rogers et al (1998) and Dorman et al (2000) extend only about 100km west of the coast. The large-scale boundary layer effects on wind speed from the coastal geometry described in Edwards et al (2002) extend up to 800km west of the coast. Such marine boundary layer processes and coastal effects do not explain the increase in winds extending from Cape Mendocino towards the trade winds that accompany many wind events. When strong wind events occur along the coast, winds often also increase far offshore extending southwest toward Hawaii. Composites of wind events from satellite derived wind speed (Figures 11

and 12) include a wind pattern extending over 2000km west of the coast. This can also be seen in the case studies with NARR fields. Wind events on 04Aug1999 (Figure 27), 22Aug2002 (Appendix Figure A6), 28Jul2001 (Appendix Figure A7), 22May2000 (not shown), and 04Jul 2000 (not shown) show very clear signals extending toward the trade winds. However, it should be noted that not all wind events show a clear connection to the trades (for example, 18Aug2002 in Appendix Figure A8).

2.5 Discussion

2.5.1 Comments on Seasonal Differences

The wind event composite patterns during summer are quite different than either winter or spring (Figure 18). The upper-air circulation pattern associated with wind events is out-of-phase with the surface circulation in summer, but in phase in winter. Summer circulation anomalies associated with wind events are relatively weak and exhibit more variety relative to the other seasons (Figure 22 and 24). Recall composites of anomalies have been computed from standardized anomalies relative to each season. Further, not all wind events are accompanied by a strong upper-air trough during summer.

During winter, the surface and upper-air circulations associated with wind events are co-located (Figures 18 and 22) with anticyclones to the west and cyclones to the east of the coast, indicating a strong, vertically extensive system. Spring patterns appear to be a transition between the winter and the summer relation with the upper-level anticyclone/cyclone slightly out of phase with the corresponding surface feature (Figures 18 and 23).

The anomalous circulation associated with wind events has some surprising dominant patterns as seen in the SOM of the summer composite anomalies. However, in summer, the surface and upper air features become more out of phase with height (Figures 24 and 25). All SOM anomaly nodes in winter and spring (Figures 22 and 23) look similar within and between the seasons, with the possible exception of nodes (2,0) and (2,1) in spring. Summer nodes (Figure 24), however, look quite different

from each other with only nodes (0,0) and perhaps (0,1) resembling the typical winter or spring node. Summer nodes (1,0), (1,1), (2,0), and (2,1) all display a similar elongated, triangular, SLP high anomaly with the northeastern portion of the surface high anomaly protruding beyond the boundary (0.3 sigma) of the 500mb anomaly. Individual nodes combine to produce the quadrature pattern observed in the composite (lower, right panel of Figure 18).

SOM nodes at 500mb and 700mb (Figures 24 and 25) indicate that summer circulations have more variety than either winter or spring. The upper high (anticyclone) anomaly (Figure 25) appears in five of the six node maps, though it is generally weaker than in other seasons. Most surprisingly there is no upper anticyclone anomaly evident at 700mb in SOM node (1,1), which is the second most common SOM node. Summer SOM nodes generally show very weak signals for both surface and upper air circulations. An upper-level negative (cyclonic) anomaly over the US West appears in four of the six SOM nodes but the low is relatively weak in nodes (1,0) and (1,1). A negative anomaly is not present over the US West in 700mb heights or in SLP in nodes (0,0) and (0,1) .

Because the summer node patterns at 500mb are varied, robust, and unusual, they are explored in more detail. The summer node patterns at 500mb can be identified with each 700mb node, though they appear in different locations in the SOM, supporting the robustness of each SOM and the notion that summer circulation associated with wind events is fundamentally different from winter. The composite patterns for wind events during spring appear to be mostly of the winter variety and the beginnings of summer-type wind event circulations.

The dates of three basic patterns in the summer 500mb SOM at lag+1 day (Figure 24) are used to create conditional composites of other atmospheric variables. From Figure 24, it appears that three basic patterns are represented by the six some nodes. Nodes (2,0) and (2,1) appear similar and both feature an approaching upper trough near 150W and 45N. The dates for these two nodes are combined and labeled “approaching trough”. The nodes (1,0) and (1,1) both exhibit surface anomalies and upper-air anomalies that are 90° out-of-phase. They both also feature an upper-level negative anomaly centered near 125W and 45N. Dates corresponding to these two nodes are combined and labeled “Quadrature”. Nodes (0,0) and (0,1) more closely resemble the composite of anomalies for winter or

spring. Dates corresponding to these two nodes are combined and labeled “Winter-Like”. Conditional composites predicated on the SOM of lag+1 (t = + 24hrs) SLP/500 mb composite of anomalies are created for each of the three newly label groups. The conditional composites are created for 700mb geopotential height fields and 925mb air temperature at lag-1 and lag+1.

The “Quadrature” and “Winter-Like” conditional composites of 700mb geopotential height fields indicate a substantial deepening of the trough over the California coast from lag-1 to lag+1 (Figure 26). In contrast, for the “Approaching Trough” conditional composite, a very weak trough lies over Point Conception at lag-1. The trough remains weak, actually moving north to eventually lie over Pt. Sur at lag+1 (referenced locations are indicated in Figures 2 and 14). The SLP over the southwestern US is actually anomalously high in the “Approaching Trough” conditional composite at both lag-1 and lag+1, unlike the other two conditional composites. Also of note, the “Approaching Trough” pattern has positive 925mb air temperature anomalies over the southwestern North America at both lag-1 and lag+1 while the two other conditional composites do not have a positive anomaly over southwestern North America at either lag.

Wind speeds southwest of Cape Mendocino during summer wind events generally have magnitude comparable to winter, yet upper-air troughs during Jul-Aug are relatively weak compared with winter. Summer is the only season where weak upper-level troughs can be found during wind events (e.g. Figure 27). Winter mean conditions do not favor strong along-coast wind at the surface. In the winter, a ridge, rather than a trough, sits along the California coast (left panel of Figure 13) and the SLP field indicates a weak offshore flow over California with high pressure firmly over the interior West. Passage of an upper trough represents a dramatic change to mean January-February conditions (compare the left panels of Figure 13 and Figure 17). The thermal low does not exist, so trough passage is an essential forcing mechanism of wind events during winter. Indeed, winter wind events are always accompanied by a strong upper trough (Figures 17 and 22, and Appendix Figure A1).

Summer events are not always accompanied by a strong trough, as seen in composites (Right panel of Figure 17), the SOM for 500mb and 700mb (Figures 24 and 25) and cases with weak or no trough at 700mb (Figure 27 and Appendix Figure A8). The quadrature-like character of the summer

circulation associated with wind events (right panel of Figure 18) and the weak troughs during some cases are not satisfactorily explained.

However, it is clear that mean conditions in spring and summer favor along shore surface wind and a trough overhead (middle and right panel of Figure 13). Thus, especially strong winds perhaps should not be expected to come with large anomalies in the circulations, but more subtle changes with a different spatial character. This would explain the lack of a strong signal in SOM node (1,1) of 700mb height anomalies (Figure 25).

2.5.2 A New Hypothesis: Southeast Migration of the North Pacific High

The signal in the trades suggests that wind events along the California coast are related to adjustments in the position and/or intensity of the individual pressure systems on either side of the coast and into the tropics. In a more general sense, this would not necessarily require a trough along the coast to intensify subsidence locally or the anticyclone more generally.

Instead, consider that in late spring and summer, the land surface of the western US continent is warm with relatively low surface pressure compared with the nearby ocean. Also, the inter-tropical convergence zone (ITCZ) is farther north (Waliser and Somerville 1993). The ITCZ is an additional source of low surface pressure. Thus, whenever an anticyclone intensifies and/or moves toward the southeast portion of the eastern North Pacific Ocean, it moves closer to fixed low pressure regions - namely the thermal low over US West and the ITCZ. In doing so, the pressure gradient must tighten leading to stronger surface winds (Figure 28). This theory is supported by the shape of the wind anomaly composite pattern shown in chapter one (Figures 11 and 12). In winter, such movement of the high pressure system would not necessarily produce strong winds since the land is cold and the ITCZ relatively far south. A trough would be required to cause a strong wind event in winter. This might explain the dissimilar upper-air circulation patterns associated with wind events. In summer, movement of the high closer to the US West Coast may be the only requirement for a wind event.

Further, this southeast migration hypothesis could explain why wind events in summer sometimes start as a trough approaches but has not yet reached the coast. The along-coast trough is relatively weak in SOM nodes ((0,0); (0,1); (1,1)) at 700mb height (Figure 25) for summer wind events when a low is farther offshore to the northwest. Wind events in summer with a very weak or no trough along the coast could be explained by a propagating offshore disturbance that alters the position of the anticyclone before the upper trough reaches the coast. It remains to be explained how an approaching low pressure system could adjust the position of the subtropical anticyclone along the US West Coast and this will be a subject of future research.

2.6 Conclusions

Primary features of the atmospheric structure during and preceding two hundred wind events identified using 25 years of buoy wind observations were derived from NCEP Global Reanalysis fields from 1981-2005. Possible mechanisms involved in the wind events were evaluated by diagnosing features and variability of the atmospheric structure of wind events at multiple vertical levels. Fourteen cases were examined with recently released, high resolution (32km) North American Regional Reanalysis fields. The case studies were selected from representative dates of archetypical patterns identified via Self Organizing Map analysis.

Based on the present study, northerly wind events are set up by a broad circulation over the eastern North Pacific Ocean and the western US. Upper-level troughs are the predominant feature that accompanies almost all northerly wind events along and offshore of the US West Coast. Thermal effects from low-level sensible heating, topographic effects, marine boundary layer processes may reinforce the dynamics of troughs along the coast ultimately creating wind events.

There is a strong seasonal modulation of these mechanisms wherein aspects of wind events can also be conceptually explained by migration or eastern intensification of the eastern North Pacific anticyclone near the US West Coast, though it remains unclear exactly which process or processes may

be responsible. The complex set of processes associated with wind events suggests that they are forced by multiple forcing mechanisms.

The most universal mechanism driving wind events are troughs along or just onshore of the coast. The movement of a trough onshore is evident in composites of surface and upper-air fields from one day before to one day after initiation of wind events. During wind events, a trough is present in composites of 700 and 500mb fields using NCEP Global Reanalysis fields. A breakdown of the dominant patterns comprising each composite indicate a trough in 700mb fields located along or onshore of the US West coast in each pattern for all seasons. A strong trough is evident at 700mb in most of the case studies of wind events examined using higher resolution (32km) NARR fields. Thus, the primary forcing for wind events can be qualitatively described using quasi-geostrophic potential vorticity concepts to approximate the relative strength and direction of vertical motion associated with troughs along the coast.

The circulation associated with wind events varies with the seasons. The atmospheric circulation during wind events typically includes a strong tough with broad, round, positive anomalies over the eastern North Pacific and negative anomalies over western North America. Surface and upper-air anomalies are co-located during winter events and most spring events.

Summer exhibits relatively weak and varied circulation patterns during wind events. Anomalies of summer wind events are in quadrature. Surface and upper-air anomalies are 90° out of phase. Troughs at 700mb are generally weak when compared with winter or spring. The circulation during spring wind events has characteristics that most resemble winter with elements of summer circulation.

The mean circulations provide important context for wind events. Winter mean circulation does not favor northerly wind. A strong trough is needed to alter the mean state and qualify as a wind event. Summer mean circulation favors northerly wind along the US West Coast. Weak troughs can boost wind speed high enough to qualify as an event.

Seasonal differences in circulation associated with wind events include the location of troughs. Troughs at 700mb are typically located onshore, east of the coast in winter while troughs are generally

much weaker located immediately along the coast or perhaps even to the west a tad during summer wind events. The seasonal preference for trough location and the quadrature pattern of surface and upper-air circulation during summer events remain unexplained.

Evidence supporting and contradicting a relation between wind events and the horizontal thermal gradient across the coast was found using the NCEP Global Reanalysis and the NARR fields. Recent papers (Liu et al 2004, Miyasaka et al 2005) implicate the low-level thermal contrast across the western continental coasts as the main forcing behind summertime surface anticyclones and northerly wind over the eastern ocean basins. The magnitude of mean northerly surface wind along and offshore of the California coast is stronger in summer, when the temperature gradient across the coast reaches the peak of its seasonal cycle. Temperatures at the 925mb level are much warmer over the western North American continent in summer when the highest mean winds are found along the coast. During individual wind events, the maximum wind speed region along the coast often coincides with the region of maximum temperature gradient across the coast as seen in NARR case studies. The magnitude of these winds decreased when temperatures dropped in the corresponding region of high temperature gradient for more than one case highlighted with NARR fields.

The correlation of wind and local temperature gradient does not demonstrate a causal link and other evidence implies the thermal gradient across the coast is not important for wind events. Wind events still occur in winter when near-surface temperatures are cool and the cross coast temperature gradient is small or of opposite sign. Composites of wind events in all seasons fail to show an antecedent warm anomaly one day before initialization of wind events. During summer, 925mb air temperatures over the continent were comparable or below their seasonal mean value both one day before and after initialization of wind events. A clear, consistent signal relating the across-coast near surface thermal gradient to wind events is not evident, at least not in the Global and Regional Reanalysis fields on the time scales considered.

Terrain and MBL effects address some, but not all aspects of the observed wind events and associated circulation. High mean winds and wind events appear tied to the California coast between Cape Mendocino and Point Conception, rather than migrating with the seasons and strongest thermal

gradient across the coast. Once initiated by a trough, channeling or other MBL-terrain effects may amplify the wind speed or alter the spatial scale of resulting surface wind. These effects cannot explain the signal far from the coast as seen in Figures 11 and 12 of Chapter One and in the NARR case studies. The spatial scale of wind events extends far beyond the range of MBL-terrain effects. Furthermore, wind events occur in winter when the MBL is weak and often wiped out by cool, northerly wind and the unstable conditions they bring.

Extension of anomalously high winds far offshore and to the southwest of the coast is evidence that wind events are sometimes associated with large-scale, rather than local processes at Cape Mendocino. Absent a strong trough, and considering the spatial and temporal scales of some wind events, it is hypothesized that a southeastward migration of the SLP high is a sufficient forcing mechanism. The SLP high is part of a relatively slow, but transient anticyclonic circulation that evolves in time. Wind events could result from a distortion of its symmetry, shape, or intensity that leads to southeastward movement of surface high pressure. As the SLP high offshore of the US West Coast moves toward the southeast, the SLP gradient increases as the surface high encounters relatively low pressure in the tropics. Movement of the SLP high then produces enhanced surface wind extending from the US West coast southwest toward Hawaii.

This hypothesis can explain aspects of the seasonal differences in the atmospheric circulation associated with wind events, such as the absence of a strong upper-level trough over the coast during some wind events. Under the hypothesized mechanism, a trough would not be necessary to cause a wind event in summer. Wind events along the coast could be produced by SLP gradient between the Pacific SLP high and the thermal surface low dominating the western continent in summer. The wind event could extend to the trades since the inter-tropical convergence zone (ITCZ) is farther north in summer. As the high moves to the southeast, the SLP gradient strengthens between the thermal low to the east and the ITCZ to the south. In winter, however, the continent is relatively cool while the ITCZ is farther south. Thus, a relatively strong trough is needed to produce a wind event in winter, but not in summer. Furthermore, the hypothesis may explain why some wind events in summer coincide with the

approach of a trough in the northwest portion of the domain. The approaching trough may signify a southeastward shift in the eastern North Pacific high.

The effect the coastal geometry and topography, thermal contrast, position of anticyclone and passing cyclones and troughs on wind events are difficult to quantify separately. Each forcing or response likely involves feedbacks to the other forcings that are similarly difficult to diagnose with the Global Reanalysis and NARR fields. In the next chapter, numerical experiments are designed to test the feasibility of a low-level thermal forcing and terrain influence on wind events over synoptic time-scales.

CHAPTER THREE

Sensitivity Tests

Abstract

Two model sensitivity tests are conducted to examine effects on the surface wind along the coast of the US of a) the large-scale thermal contrast in the lower atmosphere across the coast and b) the coastal terrain. The sensitivity tests are motivated by results from observational diagnoses in Chapters One and Two, and are guided by previously published model sensitivity tests, but with important differences. The temperature perturbation experiment produces a displacement of the eastern North Pacific surface anticyclone affecting the surface wind field offshore of the US West coast. The spatial pattern of the difference in the wind field in relation to the control run closely resembles the spatial pattern of wind events described in Chapter One (Figure 11 and 12). A mechanism responsible for wind events due to displacement of the North Pacific anticyclone was hypothesized at the end of Chapter Two (Figure 28). The temperature perturbation experiment qualitatively supports the viability of this mechanism. The terrain sensitivity experiment produces a substantial effect on surface wind in the immediate vicinity of imposed terrain changes, but not beyond, implying that the influence of coastal topography is relatively local. This conclusion is supported through an additional sensitivity experimental run for one case where the terrain is flattened over the entirety of western North America, which produced smooth and broad surface wind features, relative to the control.

3.1 Introduction

Effects of the coastal geometry and topography, thermal contrast, position of anticyclone and passing cyclones and troughs on wind events are difficult to quantify separately. Each forcing or response likely involves feedbacks to the other forcings that are similarly difficult to diagnose with the

Global Reanalysis and North American Regional Reanalysis fields (described in Chapter 2, Sections 2.3 and 2.4). One method to help assess the relative role individual forcing is through numerical experiments. Two weather simulations, rather than steady-state climate simulations, are run here. Both are sensitivity tests designed to investigate the transient response in case studies of wind events over several days time.

3.1.1 Introduction and Motivation for the Temperature Perturbation Sensitivity Test

The first involves a perturbation of the low-level atmospheric temperature field over the eastern North Pacific. In Chapter Two, it is proposed that the thermal contrast in the lower atmosphere across the US West Coast may play a role in forcing the northerly wind events along and offshore of the coast that were described in Chapter One. The perturbation experiment and control run are conducted during test cases when a wind event has been identified (e.g an event from Table 4 in Chapter Two). The hypothesis is that the temperature perturbation which enhances the thermal contrast will lead to an additional increase in surface wind magnitude extending offshore from Cape Mendocino during the wind event.

The introduction of Chapter Two described model experiments by Miyasaka and Nakamura (2005) and a conceptual framework conceived by Liu et al 2004 suggesting the main forcing for subtropical anticyclones is low-level non-convective heating and cooling (thermal contrast) at the western subtropical continental coasts. Model experiments from Miysaka and Nakamura (2005) suggest that extratropical low-level oceanic cooling, if formed for any reason, can generate a land-sea

thermal contrast, acting to force a surface subtropical high. The enhanced high surface pressure from the anticylone would then lead to enhanced surface northerly wind along the coast.

As described in the introduction of Chapter Two (section 2.2.3), climate sensitivity tests of Miyasaka and Nakamura 2005 were perpetual July steady state runs where the authors estimate a spin-up time of almost 10 days. It is interesting to consider the possible response over smaller time scales, since the mean time-scale of wind events described in Chapters One and Two is four days.

Burk and Thompson (1996) conducted a similar weather simulation to address the role of zonal surface temperature variations on low-level coastal winds. NORAPS, a regional, hydrostatic primitive equation model (Hodur 1987) is forced with time-dependent boundary conditions from the Navy global model (Hogan and Rosmaon 1991) in the experiments of Burk and Thompson (1996). The regional model has 20km horizontal resolution. The latitude-longitude range is not explicitly stated but their figures indicate the domain at least covers 128W-117W and 34N-41N. The regional model is still constrained by the lateral boundary conditions from large-scale analysis and assimilation of observed data inside the domain. The model is run for 72 hrs with emphasis on the final 24hr forecast for the target time on July 22, 1992.

Burk and Thompson (1996) run two sensitivity experiments for one case study of low-level wind along the California coast. Specifically, the authors examine the response of a low-level jet. A low-level jet (LLJ) is a strong northerly wind along the coast whose core is ~100km wide and centered 400m above sea level and 50km west of the coast of Pt. Arena. The authors attribute the existence of the low-level jet to local and large-scale baroclinicity from the thermal longitudinal temperature gradient across the coast.

The first sensitivity test of Burk and Thompson (1996) concerns the removal of the zonal sea surface temperature (SST) gradient on low-level coastal wind of wind along California coast near Pt. Arena during 24 hr period on July 22, 1992. Zonal SST difference are removed by setting a uniform value across the domain equal to the value at the domain's western edge (~1000km west of California). SST's are usually several degrees cooler immediately along the coast relative to 1000km offshore.

Thus, in their first sensitivity test, SST's are warmer than normal along the coast but constant in the zonal direction.

Burk and Thompson (1996) compare the control forecast for 0500 PDT on July 22 1992 to their first sensitivity test indicates a decrease in the amplitude of the LLJ at 425 m above sea level. The LLJ maintains structure in X-Z plane similar to control, but the wind speed drops ~10% in the core of the jet (from 21 m/s to 19 m/s - compare their Figures 5a and 8a). The surface wind 100 or more km from the coast actually increases by 0.5 m/s, presumably because the surface boundary layer conditions turn from stable (control) to unstable (test) with the prescribed change in SST, removing the stability restricting downward transfer of horizontal momentum.

The authors suggest that the longitudinal temperature gradient at sea level is not as important as the gradient above sea level between the coastal terrain and offshore air for driving strong wind along the coast. The local baroclinicity due to coastal terrain still dominates the wind and temperature structure along the coast. The large-scale baroclinicity is also still present (the SST over the eastern North Pacific are zonally uniform, but still less than coastal land temperatures) and important for the set-up of northerly coastal wind and temperature structure.

In summary, Miyasaka and Nakamura (2005) found the temperature gradient in the lower atmosphere produced a response which acts to strengthen the subtropical anticyclone and thus, the northerly along-coast winds. Miyasaka and Nakamura suggest that any type of low level subtropical atmospheric cooling over the eastern North Pacific Ocean in summer will enhance the thermal contrast and strengthen the subtropical anticyclone and northerly along-coast winds. Burk and Thompson (1996) suggest that baroclinicity (i.e. an across-coast thermal gradient) is important in the lower layers of the atmosphere, above the surface. Therefore, it is expected that the lower atmospheric temperature perturbation simulation experiment conducted in this Chapter should produce an increase in the surface wind along the coast US West Coast. New aspects of the temperature perturbation experiment conducted in this chapter include a focus on surface wind in the X-Y plane, rather than the strength of the anticyclone (as in Miyasaka and Nakamura 2005) or the above-surface low-level jet in the X-Z

plane (as in Burk and Thompson 1996). The experiment is a transient weather simulation, rather than a steady state climate simulation (as in Miyasaka and Nakamura 2005).

3.1.2 Introduction and Motivation for the Coastal Terrain Sensitivity Test

In the second sensitivity test, the coastal terrain is removed above 200 meters for 3-4 degrees longitude inland from the coast. The coastal terrain is west of the Sierra Nevada Mountains. The Sierra Nevada are a tall (over 3000 m), narrow mountain range oriented north-south on the eastern border of California, about 200km inland from the coast (grey area in the upper panel of Figure 52). This experiment is designed to investigate the spatial-scale of effects of the coastal terrain on northerly wind events. It is speculated that the removal of the coastal terrain will not substantially affect surface wind more than 1000km from the coast, supporting the hypothesis from Chapter Two that the terrain-marine boundary layer interaction is not responsible for the wind event pattern described in Chapter One (Figures 11 and 12).

As mentioned earlier, experiments with changes in the coastal and inland terrain of the US West Coast have been conducted in relation to coastal near-surface winds. Burk and Thompson (1996) flatten all terrain including the Sierra Nevada, in their second sensitivity test. The flattened terrain maintains its character as land (friction, heat capacity). Removal of the terrain has a pronounced effect on the low-level coastal wind. The northerly wind speed in the core of the low-level jet drops ~25% (21 m/s to 16m/s, compare their Figures 5a and 10a). The core flattens in shape and tilts west. Surface wind speeds decrease 1.5 m/s 100km from the coast (11 m/s to 9.5 m/s at 124W) and 1 m/s 250 km from the coast (9 m/s to 8 m/s at 125.5W).

Cui et al (1998) conduct additional sensitivity tests with regard to the effect of the Sierra Nevada mountain range on northerly wind along the California coast. Three sensitivity tests are run using a 3D hydrostatic meso-scale model (Tjernstrom 1987a,b) that has been used in a variety of settings including terrain-induced flow, coastal flows, dispersion calculations, and marine stratocumulus

(see references in Cui et al 1998). The model is set up regionally with 4km resolution over a domain 400km by 450km by 5km centered near Pt. Sur, California (Figure 29).

In the first sensitivity test Cui et al (1998), only the coastal range is specified and the Sierra Nevada do not exist in the lower model boundary. In the second test, both the coastal range and the Sierra Nevada are represented. In the third test, the coastal range and the western half of the Sierra Nevada are represented but the eastern half of the Sierra Nevada is modeled as a plateau.

The results of the tests lead the authors to suggest that the magnitude and thermal structure of the LLJ of northerly wind along the coast of California requires a realistic representation of the Sierra Nevada. The first and third sensitivity tests produced wind and temperature structure in the atmosphere along the coast that differed dramatically from test two.

In summary, Burk and Thompson (1996) found the coastal terrain exerts a more substantial effect on the LLJ along the coast than the zonal sea surface temperature gradient between the Central Pacific and the West Coast. Experiments by both Burk and Thompson (1996) and Cui et al (1998) indicate the inclusion of the Sierra Nevada is critical in reproducing the character of northerly wind along the California coast. Burk and Thompson (1996) note that local coastal terrain is important not just as a physical barrier but because of the thermal properties of the terrain create a longitudinal thermal contrast in the lower layers of the troposphere. Therefore, the flat coastal terrain experiment in this chapter will surely produce an impact on the wind field. What remains to be seen is the spatial scale of the impact and whether the influence extends beyond the immediate vicinity of the induced change in coastal terrain. New aspects of the experiment in this chapter include use of a non-hydrostatic model. Both Burk and Thompson (1996) and Cui et al (1998) use a hydrostatic model. Free from the limits of the hydrostatic approximation, non-hydrostatic models are useful specifically where considering complex terrain with relatively large topographically-induced vertical velocities may be present. Furthermore, the domain used in the modeling experiments of Cui et al (1998) includes only Central California. Burk and Thompson (1996) remove all terrain while Cui et al (1998) remove only the Sierra Nevada while retaining the coastal terrain. Neither article examines the response in oceanic wind field from the removal of the coastal terrain.

3.1.3 Organization

The following section covers the data and model used. Description of the sensitivity test design and results are presented in Section 3.3. The summary and final conclusions appear in Section 3.4.

3.2 Data and Model

3.2.1 Data

The North American Regional Reanalysis (NARR) fields are used as lateral boundary conditions for the nested model described below. The NARR fields are described in Chapter Two Section 2.2

3.2.2 Model

A nonhydrostatic version of the Pennsylvania State University-NCAR Mesoscale Model (MM5) is used (Dudhia 1993). Free from the limits of the hydrostatic approximation, non-hydrostatic models are useful specifically when considering complex terrain with relatively large topographically-induced vertical velocities may be present. The MM5 uses pressure perturbation and temperature as prognostic variables. The model has been modified (Wang and Georgakakos 2005) with respect to cloud microphysics processes that are not important for this study.

Version 3.5 of the MM5 model is run over 108 hrs (4.5) days for each of 12 case studies. The initialization field and lateral boundary conditions are provided by the North American Regional Reanalysis (NARR) field at three hour intervals (BC only). The NARR fields are described in Chapter

2 Section 2.4 The model is run on an irregular grid at 27km resolution spanning 145W-110W at 20N and expanding to 155W-100W at 55N.

3.3 Sensitivity Tests

The responses exhibited in the sensitivity tests are gauged through comparison of wind, pressure, geopotential height and temperature fields at various vertical levels (e.g. Figures 31-36) The six cases depicted in the left and right panels of Figure 30 include one winter, one spring, and four summer cases. The model was run for 4.5 days in each case covering 2 days preceding the initiation of the wind event and continuing 2.5 days into the event. All wind event initiation times are listed in Table 4 and wind events are defined as in Figure 6. The plots in Figure 32-35 are time-averaged over 24 hours to minimize differences between the test and control due simply to a difference in the timing of transient features of the circulation (except Figure 32, which is time averaged over 12 hours). Wind events typically last four days with peak winds approximately 24 hours after initiation. The date s shown in the sensitivity test figures are chosen to roughly coincide with the peak of the wind event.

The top-left panel of Figures 32-35 show the wind speed, directional arrows, and sea level pressure (SLP) for the control run while the bottom left panel depicts the corresponding map for the sensitivity run. The top middle panel shows the scalar mean difference of surface wind speed while the arrows indicate the residual (vector) difference. The lower-middle panel shows the difference in SLP and the surface residual vector difference is again included for reference. On the top right, differences in 700mb height between the sensitivity and control runs are shown along with the residual wind vector difference at that pressure level. Finally, the lower right panel depicts difference between the sensitivity and control of 925mb temperatures along with the residual wind vector difference at 925mb.

Mean values (Figure 13), composite a day preceding and an day following initiation of a wind event (Figure 17), and the Self Organizing Maps (Figures 21-24) of SLP, 700mb heights and 925mb temperatures described in Chapter 2 provide a basis for quantitative comparison of the magnitude of

changes in the following sensitivity tests discussed below. Nominal variability between seasonal means, composite values roughly estimated from these figures specifically for Cape Mendocino include:

Season	SLP	925mb Temperatures	700mb heights
Jan-Feb	6mb	5 C	75m
Apr-May	2mb	4 C	25m
Jul-Aug	1-2mb	3 C	30m

As with any sensitivity test with a limited number of cases, the results should be viewed with caution.

3.3.1 Sensitivity Test One: Temperature Perturbation

The North American Regional Reanalysis (NARR) is used as the initial and boundary forcing for a nested version of the MM5 model for weather simulations of two sensitivity tests (Figure 30). Once initialized, the model is updated with boundary conditions at three hour intervals. In the first test, S1, a low-level idealized cooling is modeled by imposing a perturbation with Gaussian shape in both horizontal and vertical dimension. This perturbation is subtracted from the temperature field used to initialize the inner MM5 domain (Figure 34). The perturbation is:

$$T'(\phi,\theta,s) = T(\phi,\theta,s) - c_T e^{-\left[\frac{(\phi-\phi_0)^2}{\sigma_x}+\frac{(\theta-\theta_0)^2}{\sigma_y}+\frac{(S-S_0)^2}{\sigma_z}\right]}$$

The second term includes an amplitude, c_T and in the argument of the exponential, ϕ, θ, and S represent longitude, latitude, and pressure level. Each has a corresponding offset (denoted with the "0" subscript) and variance, σ.

The vertical and horizontal distribution of cooling is based on analysis and modeling experiments from two recently published papers. The magnitude of cooling and distribution in space are based on the Miysaka and Nakamura (2005) climate simulation response to observed mean July diabatic heating determined from NOAA/DOE Reanalysis fields (Kanamitsu 2002) and prescribed at low-levels and limited rectangular domain (20-50N, 150W-110W) under perpetual July conditions (Miysaka and Nakamura, 2005). The model and experiments are described in Chapter Two, Section 1.2.3. The pattern of cooling achieved is roughly circular, covering the eastern North Pacific with peak magnitude of -8 degrees C near the surface (sigma 0.983) centered at ~30N, 140W (Miyasaka and Nakamura 2005, their Figure 7B). The vertical distribution of heating is estimated from the shape of mean July heating rate profiles over the eastern North Pacific (Liu et al 2004, their Figure 5a ; Miyasaka and Nakamura 2005, their figure 4b). The shape of the profiles suggests the temperature signal should peak at roughly 875mb and decrease to near zero at 700mb. Thus, the temperature perturbation in Figure 31 was applied to the initial conditions of the sensitivity tests in S1.

The lateral boundary conditions from NARR are also modified, but only at the western boundary. The temperature value below 700mb at the western edge of Figure 31 is applied to the western boundary condition from NARR. All other boundary conditions from NARR remain unperturbed.

Results for Sensitivity Test One: Temperature Perturbation

The responses to the imposed temperature perturbation in all summer cases exhibited similar characteristics. For the most part, the summer responses were different, however, from those in winter and spring. Winter and spring has a similar common pattern of response characteristics that differed from the summer cases. Thus, two figures, one each for winter/spring and summer, are sufficient to represent the character of their respective seasons (Figures 32 and 33).

There are a few archetypical responses that were seen in all cases (winter, spring, and summer), namely the anticyclone moves north and slightly east relative to the control. As a result, the region of maximum wind speed along the Northern California coast shifts northward and turns more

offshore (with a more easterly component). The SLP increased over ocean in the far north portion of the domain and decreased over ocean to the south for all cases except spring (where pressure did not increase appreciably anywhere in the domain relative to the control).

The values in the region of maximum wind speed offshore of Northern California did not appreciably change relative to the respective control simulation. The strongest signals in wind speed difference (top-center panels in Figures 32-33) are due mostly to the shift in position of the maximum wind region, not a change in magnitude. The wind speed near Cape Mendocino remained nearly the same, though some cases did show slight increase/decrease. The maximum wind speed region can be compared to the control and between sensitivity tests for different dates because the maximum winds were always tied to the coastal region with highest topography between Cape Blanco and Pt. Arena (top panel of Figure 29). Farther southwest of Cape Mendocino, extending 10 degrees or more in both latitude and longitude toward the trade wind region, surface wind speeds decrease in all cases.

While the northward shift of the anticyclone was ubiquitous, there were seasonal differences in the sensitivity runs relative to their respective control runs. In both winter and spring cases, temperatures at the 925mb level are much cooler and 700mb geopotential heights much lower over a broad region of the eastern North Pacific in the sensitivity test, relative to the control. In contrast, during each of the summer cases, the air warms at the 925mb level and the 700mb heights increase over and offshore of California, relative to the respective control simulations. All summer cases also experience an increase in coastal northerly wind speed north of Cape Blanco, while the same was not true of winter and spring cases.

The sensitivity tests suggest a relationship between the surface wind field at the coast and cooling in the lower atmosphere far to the west (i.e. the initial and boundary conditions). The cooling affects the wind via a northward movement of the eastern North Pacific. Small changes in the surface wind field are accompanied by relatively large changes in the upper air geoptential height (at 700mb) , temperature fields (at 925mb), and included a decrease in the surface wind speed ten degrees latitude and longitude southwest of the Northern California coast.

In Chapter Two, it was hypothesized that the pattern of surface wind speed and anomalies during wind events (Figures 11 and 12) could be produced by southeast migration of the North Pacific High (Figure 28). The pattern of difference in surface wind speed between S1 and the control (Top, center panel of Figure 33) appears quite similar to the spatial pattern of wind events in Figures 11 and 12. In the top, center panel of Figure 33, a *northeast* migration of the North Pacific High produces *decrease* in wind speed in relation to the control. It is then easy to imagine that a *southeast* migration of the high would produce an *increase* in wind speed of the same pattern, which lends support to the southeast migration mechanism for wind events hypothesized in Chapter Two (Figure 28). The analysis suggests the position of the North Pacific High is the main consideration for the strengthening or weakening of wind events.

3.3.2 Sensitivity Test Two: Flat Coastal Terrain

Cui et al (1998) tested the effect of the coastal terrain without the Sierra Nevada but did not examine the effect of the Sierra Nevada without the coastal terrain. In the second sensitivity test, the coastal topography above 200m is flattened inland three-four degrees longitude from the coast. The flattened region maintains its character as land in the model (i.e. heat capacity, friction), but the topographic barrier to onshore flow has been largely removed (bottom of Figure 29). After initialization, the thermal structure evolves freely inside the domain, subject only to the flattened terrain and lateral boundary conditions.

Results of Sensitivity Test Two: Flat Coastal Terrain

The response in all summer cases and the spring case had similar characteristics in common while the winter response differed from both spring and summer cases (in contrast to the previous sensitivity test where winter and spring were similar). Two figures, one each for summer/spring and winter, are sufficient to represent the character of their respective seasons (Figures 34-35).

The comparison between the sensitivity tests with flat coastal terrain and the control runs reveal generally modest changes in the surface and upper-air fields (refer to the beginning of section 3 for a rough comparison of nominal variability). Large changes in the magnitude of surface winds near Cape Mendocino are due to movement of the maximum wind region (compare top-center and left panels within each of Figures 34-35).

The response to the flat coastal terrain is limited to the surface and small spatial scales (~less than 500km) in comparison with the temperature perturbation sensitivity test (Figures 32-33), composite anomalies (e.g. Figures 20), and spatial scale of surface wind events (Figure 12).

Figure 34 is representative of the summer (and spring) cases. The magnitude of maximum surface wind offshore of the Northern California coast weakens during the sensitivity runs during summer. The wind speeds increase notably over the now-flat land while turning more onshore, especially along the Central California coast. Unlike the previous sensitivity test, the surface anticyclone does not appear to move (compare left panels of Figure 34) and 700mb heights do not appreciably change (top-right panel of Figure 34).

For the winter sensitivity test, there was very little response in any field, save for winds along the Baja peninsula (Figure 35). Recall from the beginning of section 3, winter fields have a higher degree of variability than summer fields. The strong trough along the California coast during the January wind event (e.g. Appendix Figure A1) may explain the lack of change in seen in this sensitivity test. The deep trough may dominate the circulation, preventing a greater response due to the localized coastal terrain change. Spring also has a strong trough above the coast during the event simulated, though it is not as cold, deep, or as far south as in winter (not shown).

Summer simulations are more sensitive to the terrain change factors showing a weak, but clearer response. Enhanced onshore surface wind along Central California during the sensitivity runs could be due to removal of the physical barrier, ventilation of inland temperatures, or from removal upper-air baroclinicity from the elevated heat source (removal of costal mountains). An interesting (and perhaps related) feature is the pressure increase and drop in temperature at 925mb in the localized

region southwest of Cape Mendocino during summer. The region is comparable in size and location to the maximum surface wind region (Figure 34). The cause of these last two features remains unclear.

An Additional Experiment

An additional terrain sensitivity experiment was conducted for one summer case to explore the robustness of results from the coastal terrain experiment. In the additional experiment, all terrain above 200 meters was flattened over the entirety of western North America. This "no terrain" case for the middle of August, 2002 was conducted in an identical manner to the flat terrain cases. For the "no terrain" case, the North Pacific High strengthened and diffused east (Figure XXX). The surface winds weaken substantially southwest of Cape Mendocino, relative to the control. Wind speeds along the Central California coast turn offshore and increase slightly in the sensitivity test. Overall the surface and 925m features are broad and smooth, in contrast to the spatially limited response seen in the flattened coastal terrain sensitivity experiment cases. The "no terrain" experiment thus supports the conclusion that the coastal terrain effects are spatially limited to well within 1000km from the coast, while the large-scale topographic features play a more prominent role in the relatively large spatial extent of some wind events. A similar conclusion was reached through modeling experiments by Burk and Thompson (1996) and Cui et al (1998).

3.4 Conclusions

Two sensitivity tests were run to examine the relative impacts on the surface wind field, sea level pressure field, and two upper-air fields (925mb temperatures and 700mb heights). The first test involved a temperature perturbation in the lower atmosphere over the eastern North Pacific applied to the initial field from the NARR fields. The perturbed NARR field is used to initialize the run beginning two days before a wind event. A smaller temperature perturbation is applied to the NARR boundary

forcing at subsequent update cycles (3hrly intervals) as the run continues two days after the wind event begins. The boundary perturbation is applied only in the lower atmosphere at the western boundary

This set of experiments was designed to test the effect of a large-scale increase in the lower atmospheric temperature perturbation over the eastern North Pacific on wind events along the US West Coast. An important goal of this weather simulation was determine the response produced on the time-scale of wind events (a few days), rather than the steady state response seen in previously published climate simulations.

The second sensitivity test involved flattening the coastal terrain (but not the Sierra Nevada range) 3-4 degrees inland along the western coast of North America. This experiment was designed to test whether coastal topographic features are a necessary element in the development of northerly wind events. The responses in this set of experiments produces suggestive results that shed light on possible mechanisms of northerly wind events.

The temperature perturbation sensitivity tests consistently produce northward migration of the eastern North Pacific SLP high which resulted in a northward shift of the maximum surface wind region offshore of Northern California. The shift in the maximum wind region was accompanied by relatively large changes in the upper-air geopotential height (at 700mb), temperature fields (at 925mb), and included a contiguous decrease in the surface wind speed extending ten degrees latitude and longitude southwest of the Northern California coast. Thus, the temperature perturbation affects surface wind speed relatively far from the coast via displacement of the North Pacific high pressure system. The spatial pattern of the response on surface wind speed through movement of the SLP high supports the hypothesis discussed at the end of Chapter two (Figure 28). In these sensitivity tests, however, the movement of the SLP high is in the opposite direction and produces the opposite effect. The sensitivity test produces a northeast ward movement of the SLP high causing a reduction in surface wind south of Cape Mendocino while the hypothesis suggests a southeastward movement of the SLP high causes an increase in surface wind south of Cape Mendocino. The experiment supports the hypothesis from Chapter Two suggesting a southeastward displacement of the eastern North Pacific High may play an important role in producing a wind event over synoptic time-scales.

On the other hand, the flat coastal terrain sensitivity test produces generally modest changes in the surface and upper-air fields which are limited mostly to the surface and small spatial scales. Changes in summer are larger than in winter, despite the climatological tendency toward greater variability in winter. The winter event is due to a strong trough over the coast in both the control and sensitivity run. The seasonal difference in response is consistent with the notion that strong troughs are a dominant cause of wind events in winter (as described in Chapter 2), but not all summer events. An additional terrain sensitivity experiment is run for one case where not just the coastal terrain but all terrain of western North America is flattened. This experiment produces broad, smooth changes to the wind field in contrast to the coastal terrain experiment and provides a basis of support for the limited role of coastal terrain in the large-scale wind field structure during some wind events.

DISSERTATION CONCLUSIONS AND RECOMMENDATIONS

Persistence, seasonality, and variability in space and time of northerly surface wind episodes over the eastern North Pacific Ocean are described in Chapter One. This study is based upon 20 years of coastal buoy observations and six years of surface wind estimates derived from satellite scatterometer with 25km resolution. Especially in spring and summer, the wind climate along and offshore of the US West coast is dominated by a sequence of enhanced northwesterly wind episodes, lasting up to 10 days, and typically 4-5 days. The significant finding is that the strengthened winds cover a surprisingly large portion of the eastern North Pacific Ocean, often extending from Cape Mendocino on the California coast over 2500km southwest to Hawaii.

The circulation, seasonality, and forcing of the atmosphere associated with wind events was analyzed in Chapter Two. This analysis was based upon two hundred wind events from 1981-2005 during three 2-month seasons (Jan-Feb, Apr-May, and Jul-Aug) representing winter, spring, and summer. Roughly three events occur during each season. On average, wind events are present during ~20% of the time in each two-month season. Wind events were analyzed at the surface and multiple vertical levels using 25 years of NCEP Global Reanalysis fields. In addition, specific events were studied with higher resolution North American Regional Reanalysis fields.

Upper-level troughs observed at 700mb, 500mb, and 300mb levels are a nearly universal feature of the circulation associated with wind events. In winter and spring, wind events coincide with a strong upper trough located above the coast during the peak of the event. However, during summer, when the mean anticyclonic circulation around the North Pacific High and the large-scale thermal contrast across the US West Coast favors northerly wind, some wind events coincided with a very weak or imperceptible trough. Summer was also unusual in that circulation anomalies at the surface during wind events were not always aligned with those aloft. In contrast, positive surface circulation anomalies always coincide with positive upper-air anomalies, and vice versa, during winter and spring wind events. Large-scale circulation, thermal effects from low-level sensible heating, in addition to

terrain-marine boundary layer interaction, and other influences on enhanced northerly wind events were investigated. The observational evidence indicates that these processes and their interaction may be important driving factors for some wind events but not others, and it appears these forcings may act intermittently. The fall season was not covered in detail because mean along-shore wind speeds and the frequency of wind events are at an annual minimum. It is worth noting that the thermal contrast and the intensity of upper troughs over the coast of California are both relatively weak during fall, thus supporting the importance of the two mechanisms.

Aspects of the spatial pattern of wind events from Chapter One, and the atmospheric structure and seasonal differences in Chapter Two can be conceptually explained by migration or eastern intensification of the eastern North Pacific high pressure system. This hypothesis could explain the absence of strong troughs during some wind events in summer, while still supporting strengthened winds extending toward the trade winds and Hawaii. With the southeastward movement of the surface high pressure system, a trough would not be necessary to cause a wind event in summer. Wind events along the coast could be produced by the SLP gradient between the Pacific SLP high and the thermal surface low dominating the western continent in summer to the east, and the ITCZ to the south. In winter, a trough is necessary to drive the northerly surface wind since the US West is dominated by cool temperatures and high pressure.

This hypothesis is supported by a temperature perturbation model sensitivity test in Chapter Three. Twelve wind event case studies were modeled using the MM5 non-hydrostatic meso-scale model with lateral boundary forcing from the North American Regional Reanalysis. In the temperature perturbation sensitivity test, the key response was manifest as a movement of the North Pacific High, which also produced a signal in the surface wind that extended far to the southwest from Cape Mendocino toward the tropics and Hawaii. The shape of the response was similar to that in the wind event composite anomaly pattern from Chapter One.

Another sensitivity experiment with flat coastal terrain produces a modest response in the surface wind field over relatively small spatial scales indicating a limited role of coastal terrain in the large-scale wind field structure during some wind events. During winter, when a strong trough is

associated with the wind event, the response from the coastal terrain sensitivity test is especially weak compared to summer. The seasonally asymmetric response supports the concept that strong troughs are the primary mechanism of wind events during winter, while other processes become more prominent during summer.

The dissertation points to several future research paths. In Chapter One, preliminary work indicated a similar spatial evolution pattern associated with wind events defined at a different buoy. A more flexible proxy for wind events based on NARR wind speed would allow exploration of the spatial and temporal variability of wind events at other locations over a longer, more consistent record.

A natural outgrowth of the analysis presented in Chapter Two is to investigate surface wind speed and spatial extent during wind events as a function of upper trough strength and as a function of the basic summer patterns. Dynamics surrounding the wind event mechanism hypothesized in Chapter Two should be explored further. About a third of summer wind events are associated with an unusual surface and upper-air pattern that led, in part, to the development of the hypothesis. Surface pressure along and southwest of Cape Mendocino increases and these wind events reach their peak when an upper-level trough approaches, but has not yet reached, the coast. A future investigation should examine the dynamics of interaction between upper-level troughs and subtropical anticyclones in the context of coastal wind events.

The low-level temperature perturbation sensitivity experiment in Chapter Three suggests it may be worthwhile to pursue further modeling sensitivity and significance tests to examine the influence of lower atmospheric diabatic heating sources and sinks, or other influences on the across-shore thermal contrast affecting the eastern North Pacific High and equatorward wind events over synoptic time-scales.

In addition, the effects of wind events should be explored, such as the impact of wind events on ocean surface waves, ocean mixing, and ocean currents. The association between wind events and the vertical and horizontal structure of the marine boundary layer and cloud cover could also be studied.

TABLES

Table 1: NDBC Buoy Wind Observations. Buoy 23 data have been relabeled as buoy 63 prior to 1997 when buoy 23 was moved to its current location.

Buoy 460##	Latitude N	Longitude	Start Year	% coverage
14	39.22	-123.97	1981	88.3
13	38.23	-123.32	1981	85.7
59	37.98	-130	1994	81.3
12	37.36	-122.88	1980	74.9
42	36.75	-122.42	1987	86.6
28	35.74	-121.89	1983	81.0
11	34.88	-120.87	1980	70.0
23	34.71	-120.97	1997	91.5
63	34.25	-120.66	1982	77.5
54	34.27	-120.45	1994	86.9
47	32.43	-119.53	1999	91.1

Table 2: QSCAT Satellite orbit pass times

Range (Longitude)	GMT	Orbit
115W-140W	1300-1400	Ascending
140W-155W	1500	Ascending
115W-125W	0100	Descending
125W-155W	0200-0300	Descending

Table 3: Wind Event Dates at Pt Arena (B14). The times noted are for start time (t=0) hour of wind events identified in the buoy time series as in Figure 6 in section 3.1.3. The study period is Apr-Aug seasons from 2000-2005.

#	Year	Month	Day	Hr (Z)
1	1999	Jul	2	6
2	1999	Jul	8	5
3	1999	Aug	5	5
4	1999	Aug	14	18
5	1999	Aug	21	9
6	1999	Aug	31	8
7	2000	May	17	15
8	2000	May	25	8
9	2000	May	29	23
10	2000	Jun	23	6
11	2000	Jul	3	5
12	2000	Jul	26	5
13	2000	Aug	14	5
14	2001	Apr	10	19
15	2001	Apr	22	5
16	2001	May	2	6
17	2001	May	10	5
18	2001	May	17	20
19	2001	May	29	20
20	2001	Jun	2	22
21	2001	Jun	13	23
22	2001	Jul	1	6
23	2001	Jul	15	6
24	2001	Jul	29	6
25	2001	Aug	16	7
26	2001	Aug	26	6
27	2002	Apr	15	18
28	2002	Apr	19	18
29	2002	Apr	26	20
30	2002	May	6	2
31	2002	May	14	22
32	2002	May	31	2
33	2002	Jun	20	4
34	2002	Jul	4	12
35	2002	Aug	7	4
36	2002	Aug	19	4
37	2002	Aug	26	18
38	2003	Apr	18	19
39	2003	May	8	13
40	2003	May	15	13
41	2003	Jun	16	5
42	2003	Jun	22	15
43	2004	Apr	9	4
44	2004	May	10	18
45	2004	May	30	4
46	2004	Jun	12	3

Table 3: Wind Event Dates at Pt Arena (B14) Continued. The times noted are for start time (t=0) hour of wind events identified in the buoy time series as in Figure 6 in section 3.1.3. The study period is Apr-Aug seasons from 2000-2005.

47	2004	Jun	15	5
48	2004	Jun	28	2
49	2005	Apr	10	4
50	2005	Apr	15	2
51	2005	Apr	18	10
52	2005	May	23	14
53	2005	Jun	1	3
54	2005	Jun	12	4
55	2005	Jul	3	6
56	2005	Aug	30	10

Table 4: Wind Event Times (UTC) in Each Season (Jan-Feb, Apr-May, Jul-Aug)

	Yr	Mo	Dy	Hr	Yr	Mo	Dy	Hr	Yr	Mo	Dy	Hr
1	1982	Jan	4	6	1981	Apr	25	18	1981	Jul	5	18
2	1982	Jan	11	0	1981	Apr	30	6	1981	Aug	4	6
3	1982	Jan	20	0	1981	May	19	6	1981	Aug	11	0
4	1982	Jan	27	18	1981	May	29	6	1981	Aug	25	6
5	1982	Feb	20	12	1982	Apr	14	18	1982	Jul	12	12
6	1983	Jan	7	12	1982	Apr	27	18	1982	Jul	27	18
7	1984	Jan	22	0	1982	May	6	6	1983	Jul	2	6
8	1984	Feb	20	0	1982	May	25	12	1983	Jul	7	18
9	1985	Jan	27	12	1983	Apr	1	18	1983	Jul	23	6
10	1985	Feb	14	18	1983	May	8	0	1983	Jul	30	18
11	1985	Feb	28	18	1984	Apr	6	0	1983	Aug	7	6
12	1986	Feb	2	18	1984	Apr	16	12	1984	Jul	8	12
13	1987	Jan	12	0	1984	Apr	22	6	1984	Jul	21	6
14	1987	Feb	16	0	1985	Apr	22	18	1984	Jul	27	6
15	1988	Jan	16	18	1985	May	3	0	1984	Jul	31	6
16	1989	Jan	11	18	1985	May	24	6	1984	Aug	13	6
17	1989	Jan	22	18	1986	Apr	10	0	1984	Aug	18	12
18	1989	Jan	26	18	1986	Apr	21	12	1984	Aug	31	12
19	1989	Jan	30	18	1986	May	6	0	1985	Aug	3	6
20	1989	Feb	11	6	1987	Apr	10	6	1986	Jul	3	0
21	1989	Feb	26	0	1987	Apr	17	0	1986	Jul	14	6
22	1990	Jan	13	18	1987	May	14	6	1987	Jul	5	6
23	1990	Jan	21	0	1987	May	22	0	1987	Jul	15	6
24	1990	Jan	25	6	1987	May	31	0	1988	Jul	10	0
25	1990	Jan	30	0	1989	Apr	9	12	1988	Jul	16	6
26	1990	Feb	3	0	1990	Apr	20	0	1988	Aug	16	18
27	1991	Jan	14	12	1990	Apr	22	18	1989	Jul	3	6
28	1991	Jan	27	0	1990	May	5	6	1989	Jul	13	12
29	1991	Feb	14	12	1990	May	9	18	1989	Jul	18	6
30	1994	Jan	4	6	1991	Apr	6	12	1989	Jul	26	6
31	1994	Feb	7	0	1991	Apr	26	6	1989	Aug	7	6
32	1995	Feb	13	6	1991	May	7	6	1989	Aug	23	0
33	1996	Jan	16	0	1991	May	13	6	1989	Aug	31	12
34	1996	Jan	21	0	1991	May	16	6	1990	Jul	21	12
35	1997	Jan	4	12	1991	May	20	6	1990	Aug	12	6
36	1997	Feb	11	6	1994	Apr	12	6	1990	Aug	22	6
37	1997	Feb	16	12	1994	Apr	25	18	1991	Jul	23	18
38	1997	Feb	25	0	1994	May	10	6	1991	Aug	1	6
39	1998	Feb	23	12	1994	May	22	18	1991	Aug	22	18
40	1999	Jan	5	12	1995	Apr	12	18	1992	Jul	22	18
41	1999	Jan	23	18	1996	Apr	26	12	1992	Aug	4	6
42	1999	Jan	30	12	1996	May	8	6	1992	Aug	16	6
43	1999	Feb	3	12	1996	May	22	6	1993	Jul	11	0

Table 4: Wind Event Times (UTC) in Each Season (Jan-Feb, Apr-May, Jul-Aug) Continued

44	1999	Feb	8	6	1997	Apr	7	18	1993	Jul	22	18
45	2000	Jan	4	0	1997	Apr	23	0	1993	Aug	12	6
46	2000	Jan	25	0	1997	Apr	26	6	1993	Aug	22	18
47	2001	Jan	13	18	1997	Apr	30	0	1994	Jul	13	12
48	2001	Jan	28	12	1998	Apr	6	6	1994	Jul	27	6
49	2001	Feb	4	6	1998	Apr	23	6	1994	Aug	3	18
50	2002	Feb	27	12	1998	May	7	12	1994	Aug	14	12
51	2003	Jan	31	12	1999	Apr	11	6	1994	Aug	29	6
52	2003	Feb	18	18	1999	Apr	19	12	1995	Aug	6	12
53	2003	Feb	27	0	1999	Apr	26	0	1996	Jul	8	12
54	2004	Jan	23	18	1999	May	6	0	1996	Aug	1	6
55	2004	Jan	29	12	1999	May	11	6	1996	Aug	17	6
56	2004	Feb	3	0	1999	May	18	6	1996	Aug	31	6
57	2004	Feb	17	12	1999	May	26	6	1997	Jul	6	0
58	2004	Mar	1	18	2000	May	16	12	1998	Jul	17	6
59	2005	Jan	10	12	2000	May	24	6	1998	Aug	4	12
60	2005	Feb	4	0	2000	May	29	0	1998	Aug	14	12
61					2001	Apr	8	18	1999	Jul	6	6
62					2001	Apr	20	6	1999	Aug	3	6
63					2001	Apr	30	6	1999	Aug	12	18
64					2001	May	8	6	1999	Aug	19	6
65					2001	May	15	18	1999	Aug	29	6
66					2001	May	27	18	2000	Jul	2	6
67					2001	Jun	1	0	2000	Jul	25	6
68					2002	Apr	13	18	2000	Aug	13	6
69					2002	Apr	17	18	2001	Jul	13	6
70					2002	Apr	24	18	2001	Jul	27	6
71					2002	May	4	0	2001	Aug	14	6
72					2002	May	13	0	2001	Aug	24	6
73					2002	May	29	0	2002	Jul	2	12
74					2003	Apr	16	18	2002	Aug	5	6
75					2003	May	6	12	2002	Aug	17	6
76					2003	May	13	12	2002	Aug	24	18
77					2004	Apr	8	6	2005	Jul	1	6
78					2004	May	9	18	2005	Aug	28	12
79					2004	May	29	6				
80					2005	Apr	8	6				
81					2005	Apr	13	0				
82					2005	Apr	16	12				
83					2005	May	21	12				
84					2005	May	30	0				

Table 5: SOM Nodes Corresponding to Case Studies Joint SOM nodes are listed for SLP/500mb height anomalies at lag+1 (500HA+), SLP/925mb temperatures anomalies at lat+1 (925A+) and lag-1 (925A-), SLP/700mb heights at lag+1 (700HF+) and lag-1 (700HF-), and SLP/700mb height anomalies at lag+1 (700HA+) and lag-1 (700HA-).

YYYY	MON	DAY	HR	500HA+	925TA+	925TA-	700HF+	700HF-	700HA+	700HA-
1982	May	25	12Z	(0,1)	(2,1)	(1,0)	(2,1)	(0,1)	(2,1)	(0,1)
1990	Aug	12	06Z	(2,1)	(0,0)	(2,0)	(1,1)	(1,0)	(0,0)	(0,1)
1991	Jan	14	12Z	(1,1)	(2,0)	(1,0)	(2,1)	(1,1)	(2,1)	(1,0)
1999	Aug	3	06Z	(1,1)	(0,0)	(2,0)	(1,1)	(2,0)	(0,0)	(0,1)
2000	May	16	12Z	(2,0)	(0,0)	(1,0)	(0,0)	(1,1)	(0,0)	(1,1)
2000	Jul	1	06Z	(0,1)	(0,1)	(1,1)	(2,0)	(1,1)	(2,0)	(2,0)
2001	Apr	30	06Z	(2,0)	(0,1)	(1,1)	(2,0)	(2,1)	(1,0)	(2,0)
2001	Jul	27	06Z	(1,1)	(1,1)	(0,1)	(2,1)	(0,1)	(2,0)	(2,0)
2002	Aug	17	06Z	(0,1)	(0,1)	(1,1)	(2,1)	(0,0)	(2,0)	(0,0)
2002	Aug	24	18Z	(2,1)	(2,0)	(1,0)	(0,1)	(2,0)	(0,0)	(1,1)

FIGURES

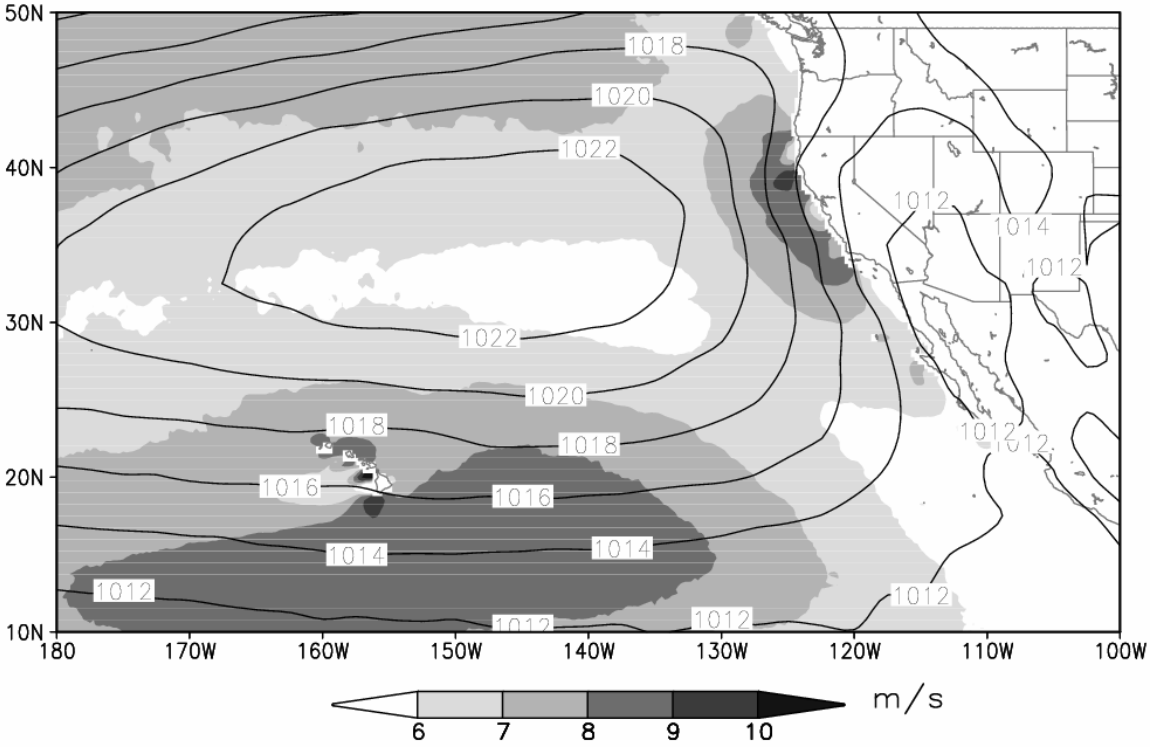

Figure 1: Apr-Aug climatological mean wind speed (from QSCAT satellite 2000-2005) with sea level pressure in mb (from NCEP Reanalysis 1982-2005).

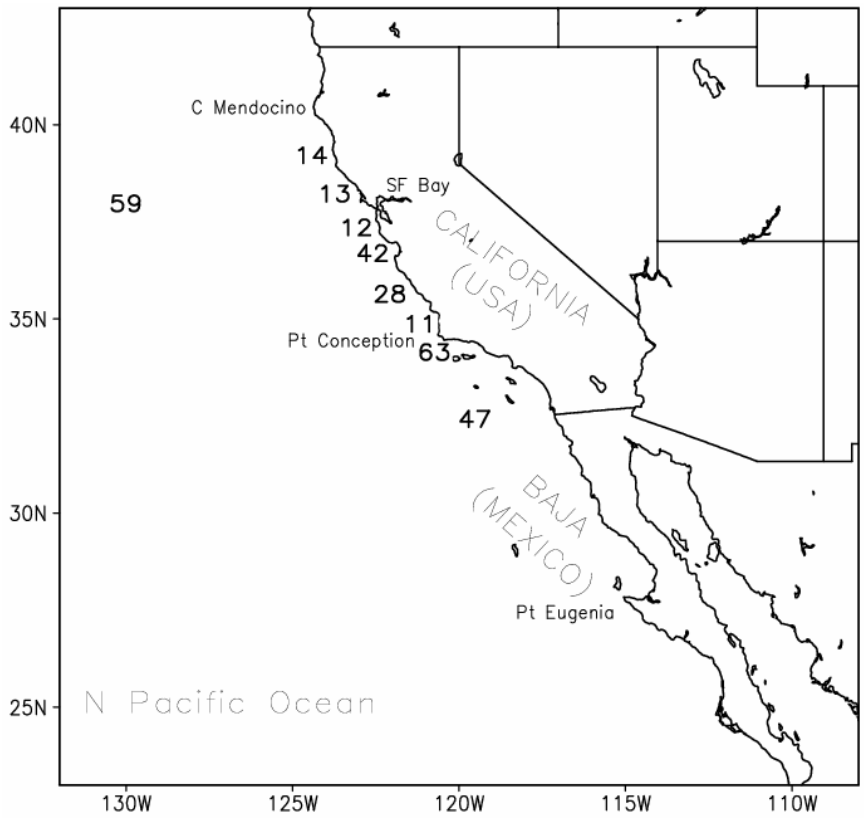

Figure 2: Geographical reference and buoy locations. Numbers mark approximate location of buoys from Table 1. Buoys 23 and 54 are not labeled but are in the immediate vicinity of Buoy 63 at Point Conception. Three prominent protrusions along the coast are Cape Mendocino, Point Conception, and Punta Eugenia. The state of Oregon borders California to the north.

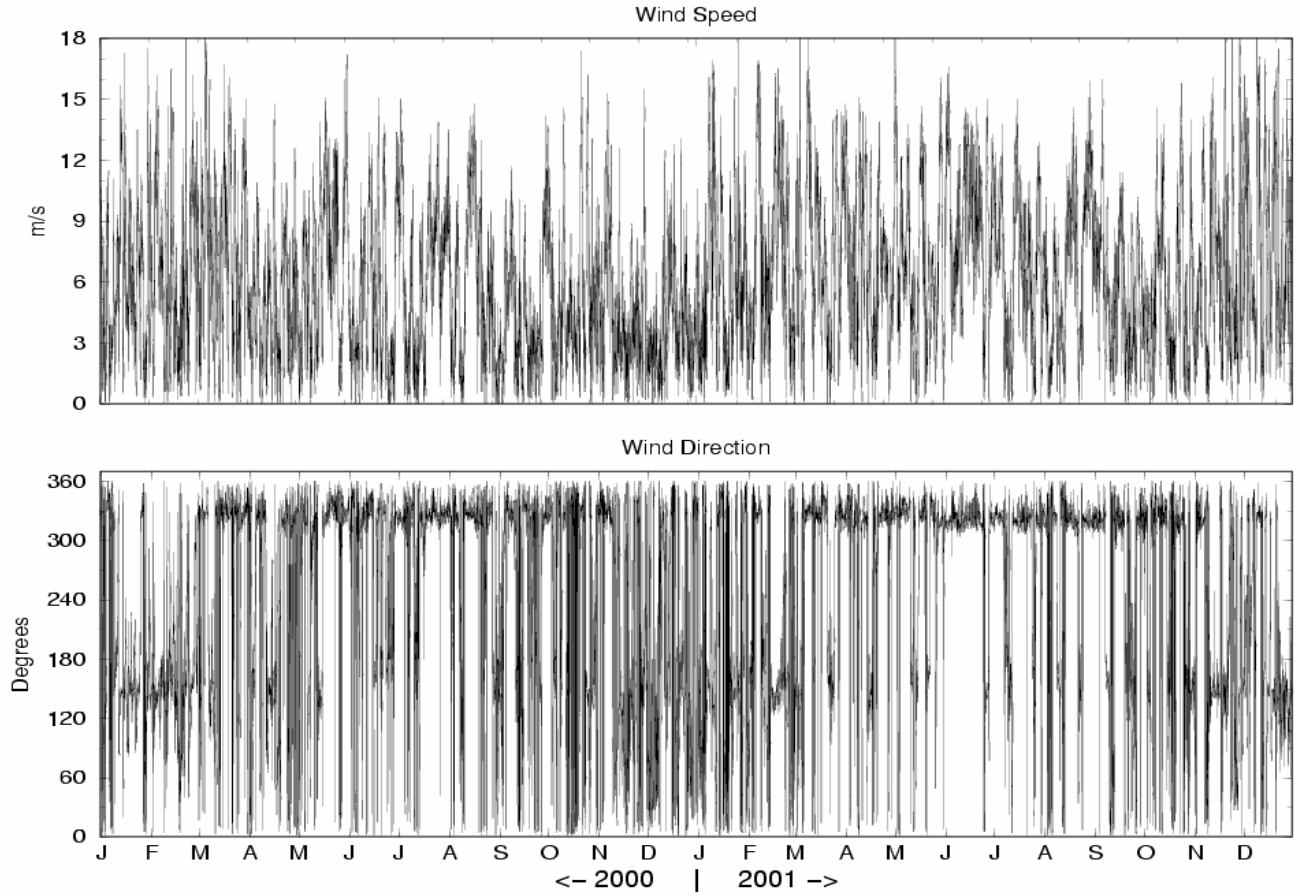

Figure 3: Hourly time series of wind speed and wind direction at Pt Arena (B14) for 2000-2001. Winds are persistently from the northwest in summer in these and other years.

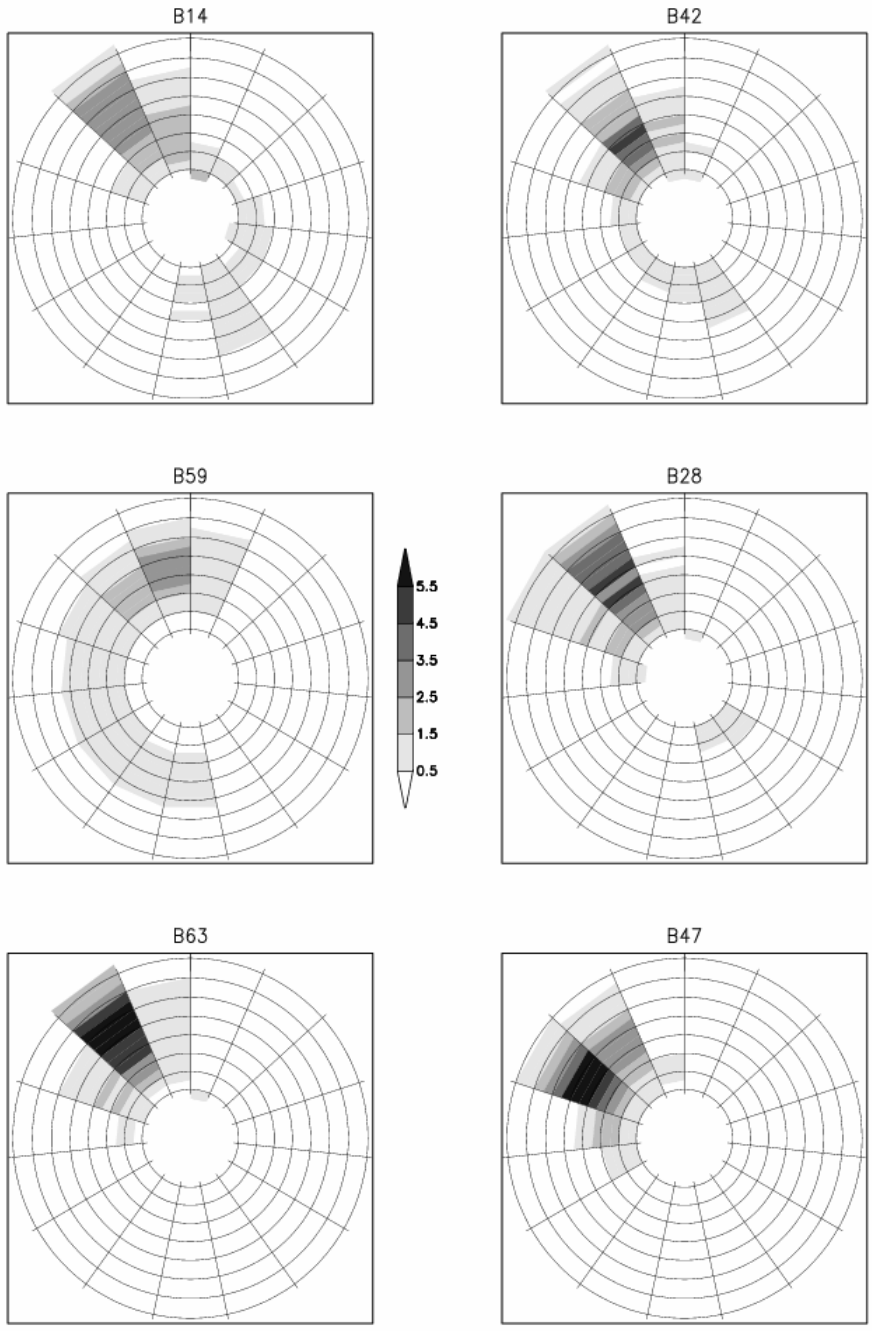

Figure 4: Buoy wind roses calculated from long-term hourly buoy records in Table 1. Shading indicates percentage of observations within the specified speed-direction bin. Wind direction is indicated by compass reference (North is 0°, 360°) at 24° degree intervals. Wind speed is indicated by distance from the origin. Grid lines are spaced at 2 m/s intervals beginning with 2 m/s extending outward to 16 m/s.

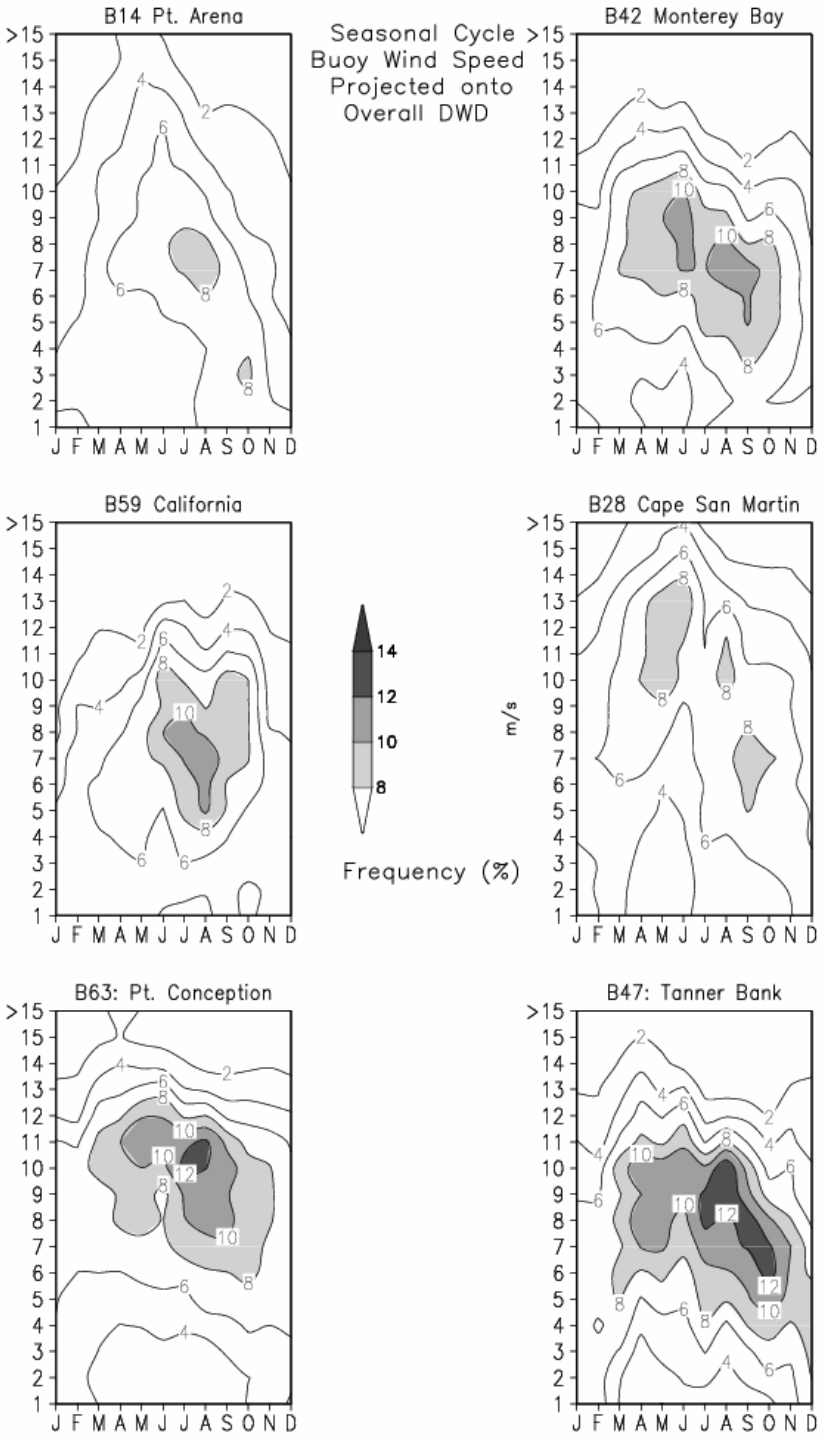

Figure 5: Seasonal cycle of projected buoy winds. Contours and shading indicate the percentage of projected observations at the specified speed and month. Winds are projected on the overall dominant wind direction (DWD).

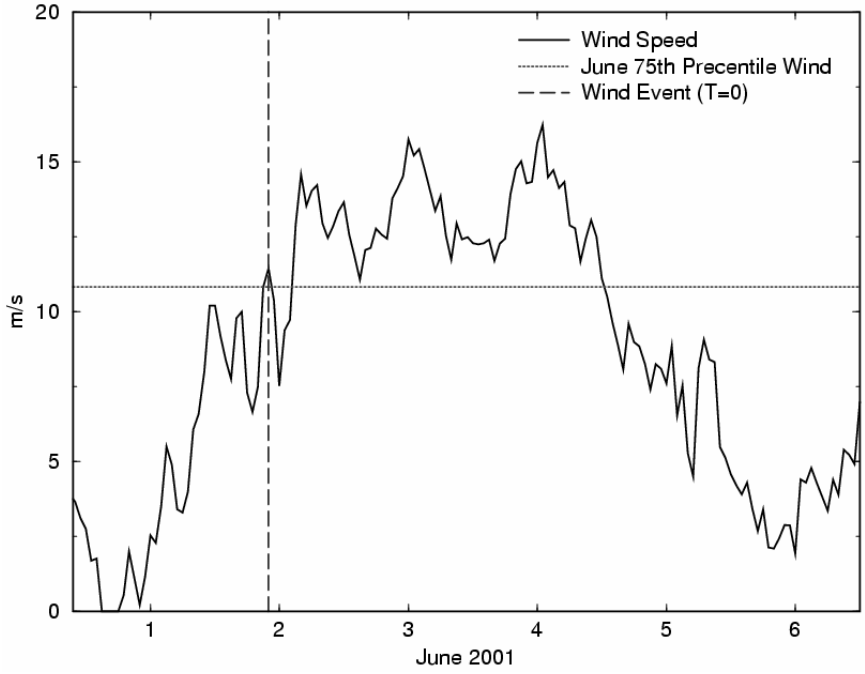

Figure 6: Wind Event Example. A wind event is identified in buoy wind at 20Z on 01 June 2001 (dashed vertical line). The horizontal line is the 75th percentile wind speed at buoy 46014 for the long-term (1981-present) for June. The dotted vertical line marks the initiation of the event, when the wind speed at the initial hour and 18 of the subsequent 35 hours are above the 75th percentile. A new event cannot be defined until wind speed remains below the 75th percentile for 36 consecutive hours.

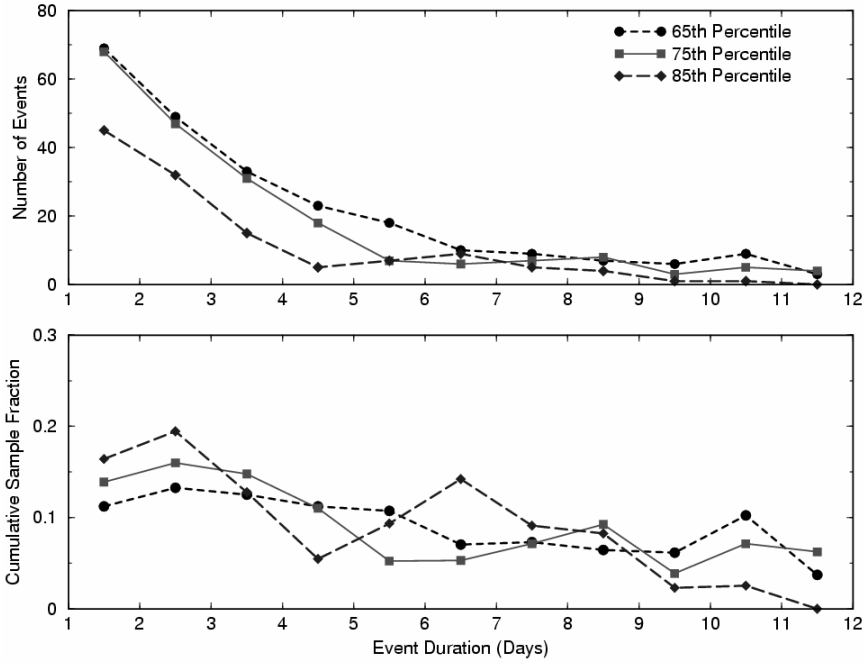

Figure 7: Wind Event Frequency-Duration-Threshold. The x-axis is duration of individual wind events defined in the text and in Figure 6. In the upper panel, the y-axis is the number of events identified (of a given duration and exceeding indicated frequency) during Apr-Aug of 1981-2005 for buoy 46014. Threshold wind speeds of 65th, 75th, and 85th percentile wind speed for all events considered were used in the event definition to test the stability of event frequency. Only the 75th percentile is used in subsequent analyses. In the lower panel, the sample fraction of cumulative event duration is the combined time among all counted events, of a given duration, divided by the total combined duration of all events. Thus, between 4-5 days duration on the x-axis, the corresponding values is 4.5 days multiplied by the number of events (from upper panel) divided by the sum total of all durations (1-2, 2-3, ...11-12 days) multiplied by their corresponding number of events.

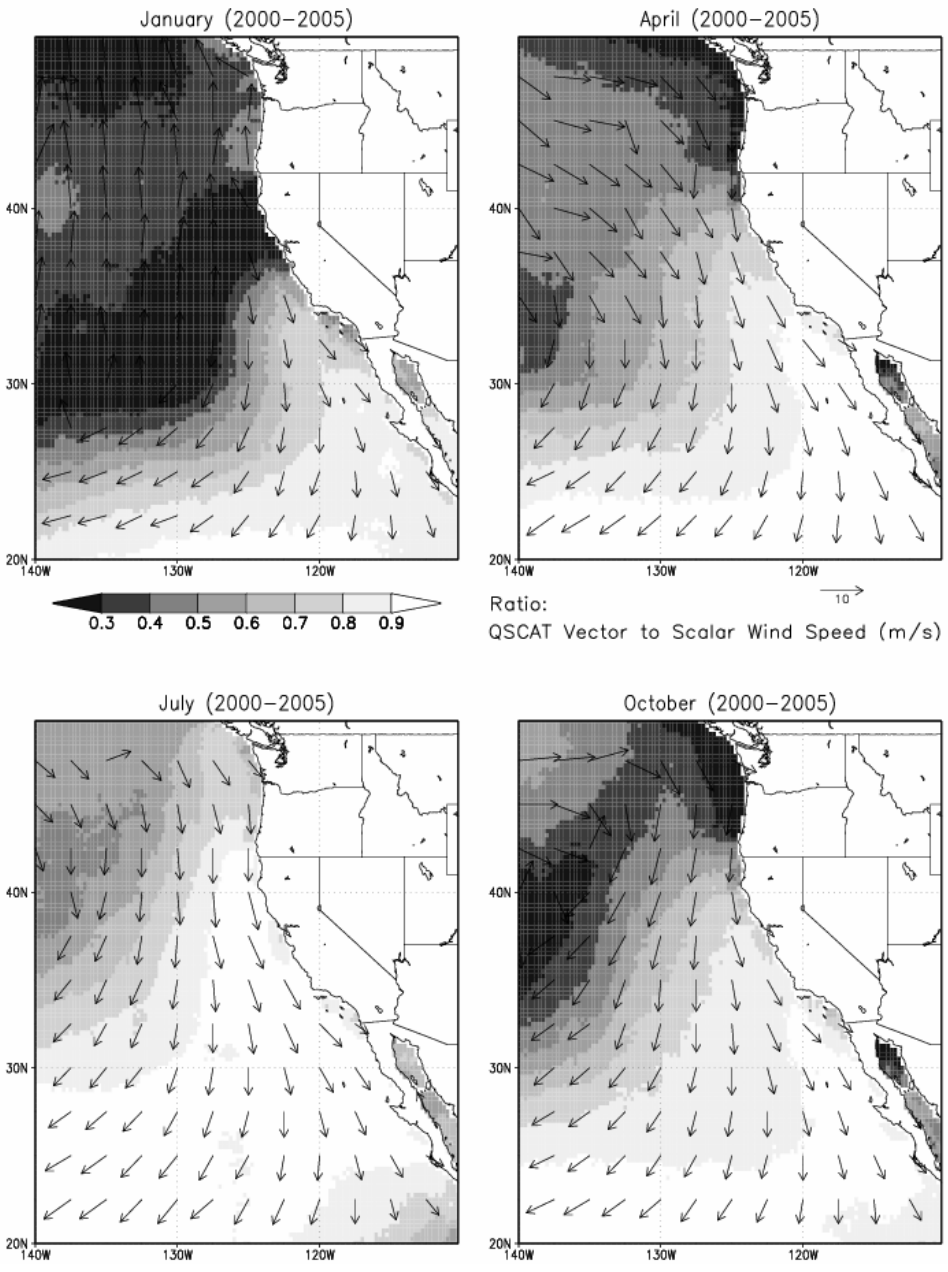

Figure 8: Seasonal Constancy of QSCAT wind speed. The ratio of vector to scalar wind speed magnitudes. The arrows indicate the monthly dominant wind direction, not the vector winds. An arrow is plotted for every 10^{th} grid in both horizontal dimensions.

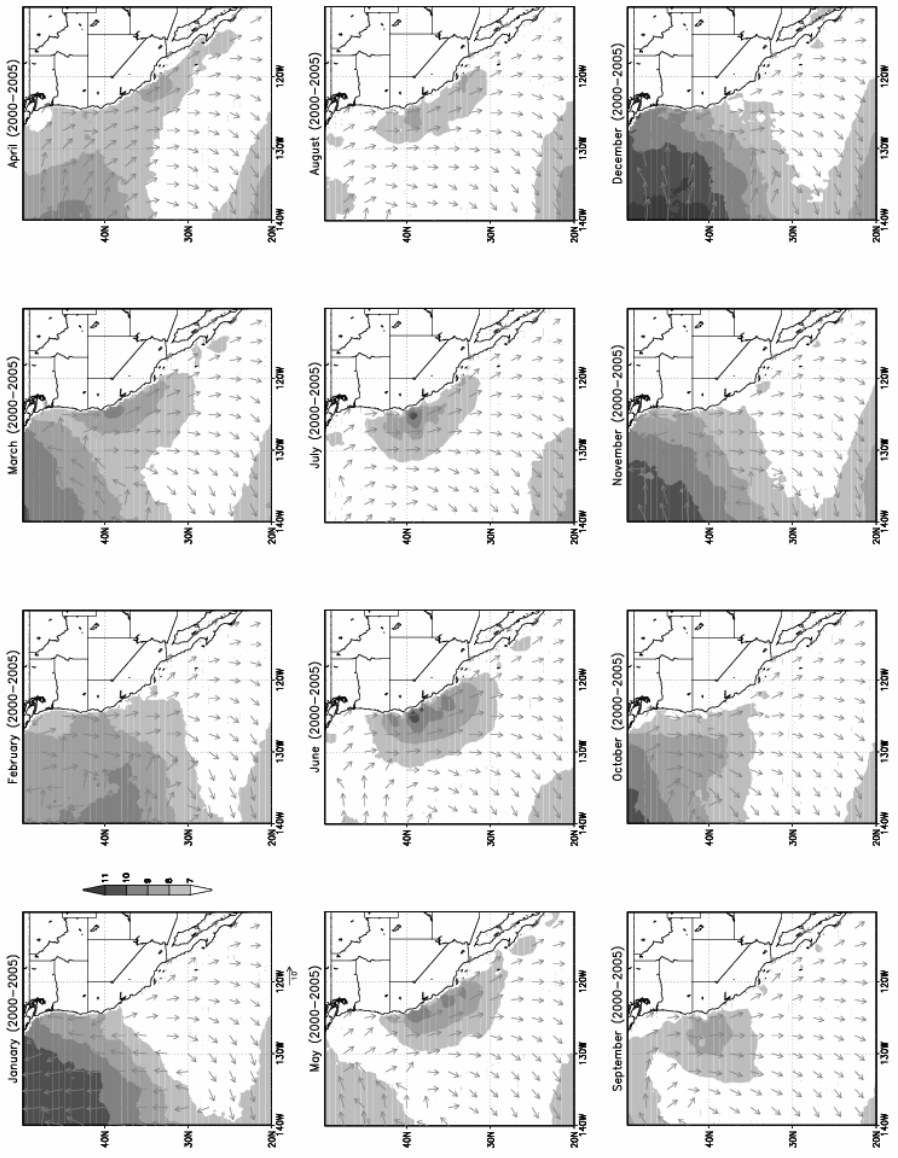

Figure 9: Monthly mean climatology of QSCAT wind speed (m/s). The arrows indicate monthly dominant wind direction.

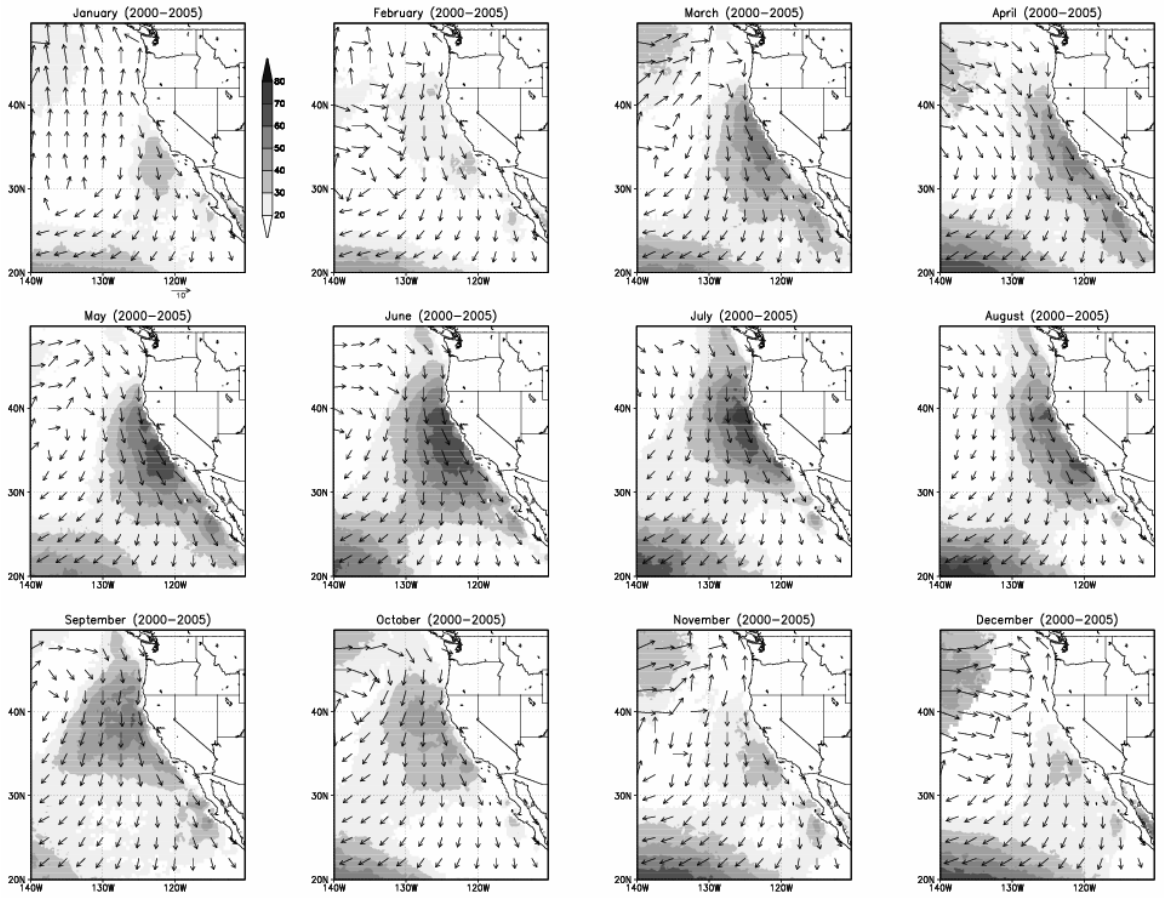

Figure 10: Threshold exceedance frequency of projected winds. Color scale indicates percent of winds exceeding 7.5 m/s wind speed for each month. The arrows indicate monthly dominant wind direction.

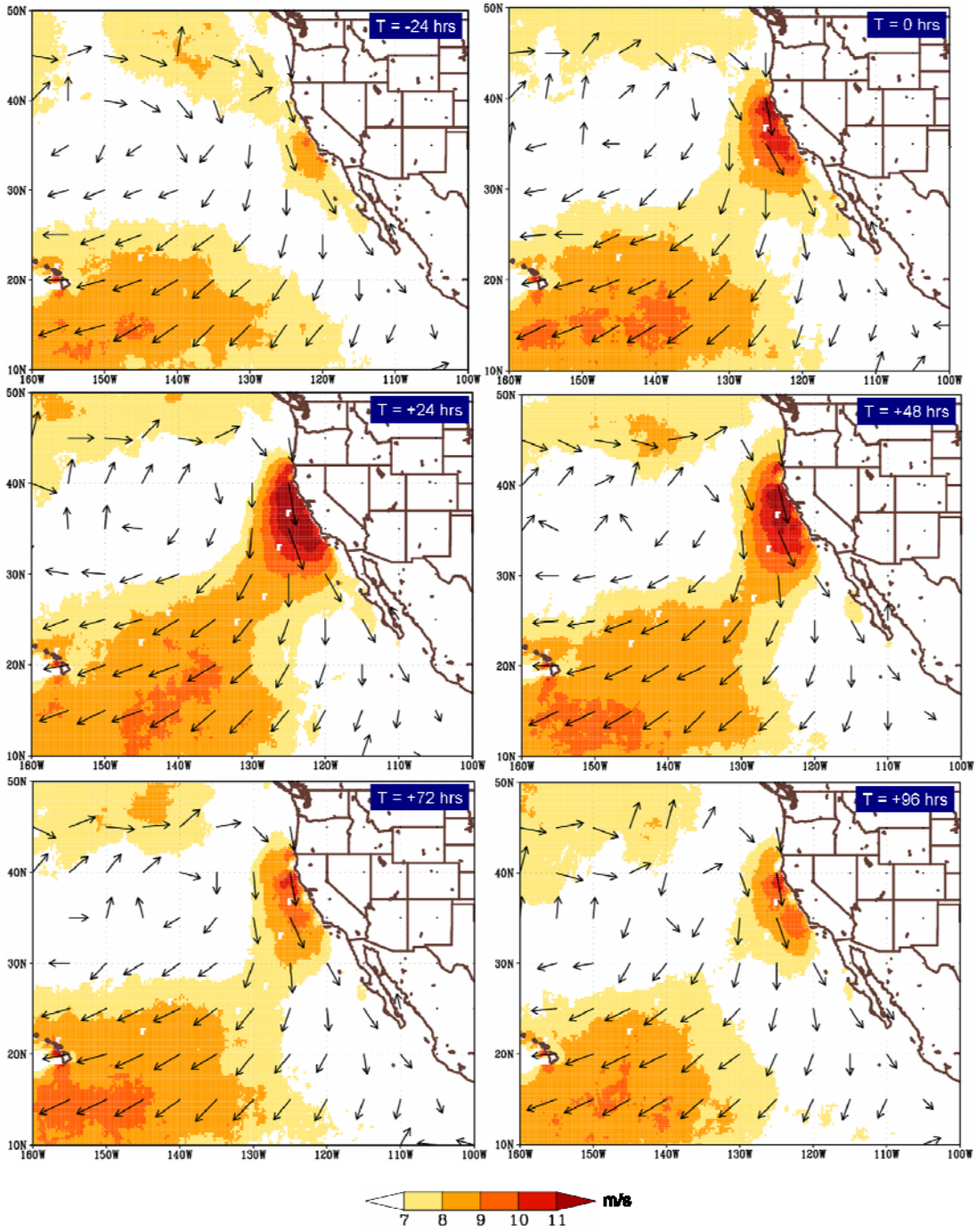

Figure 11: Composite evolution QSCAT wind field for wind events identified at Pt Arena (B14) and listed in Table 3. Wind speeds are in m/s. Arrows indicate the dominant wind direction in each composite map. The composite maps are shown at intervals relative to t=0, as defined in Figure 6.

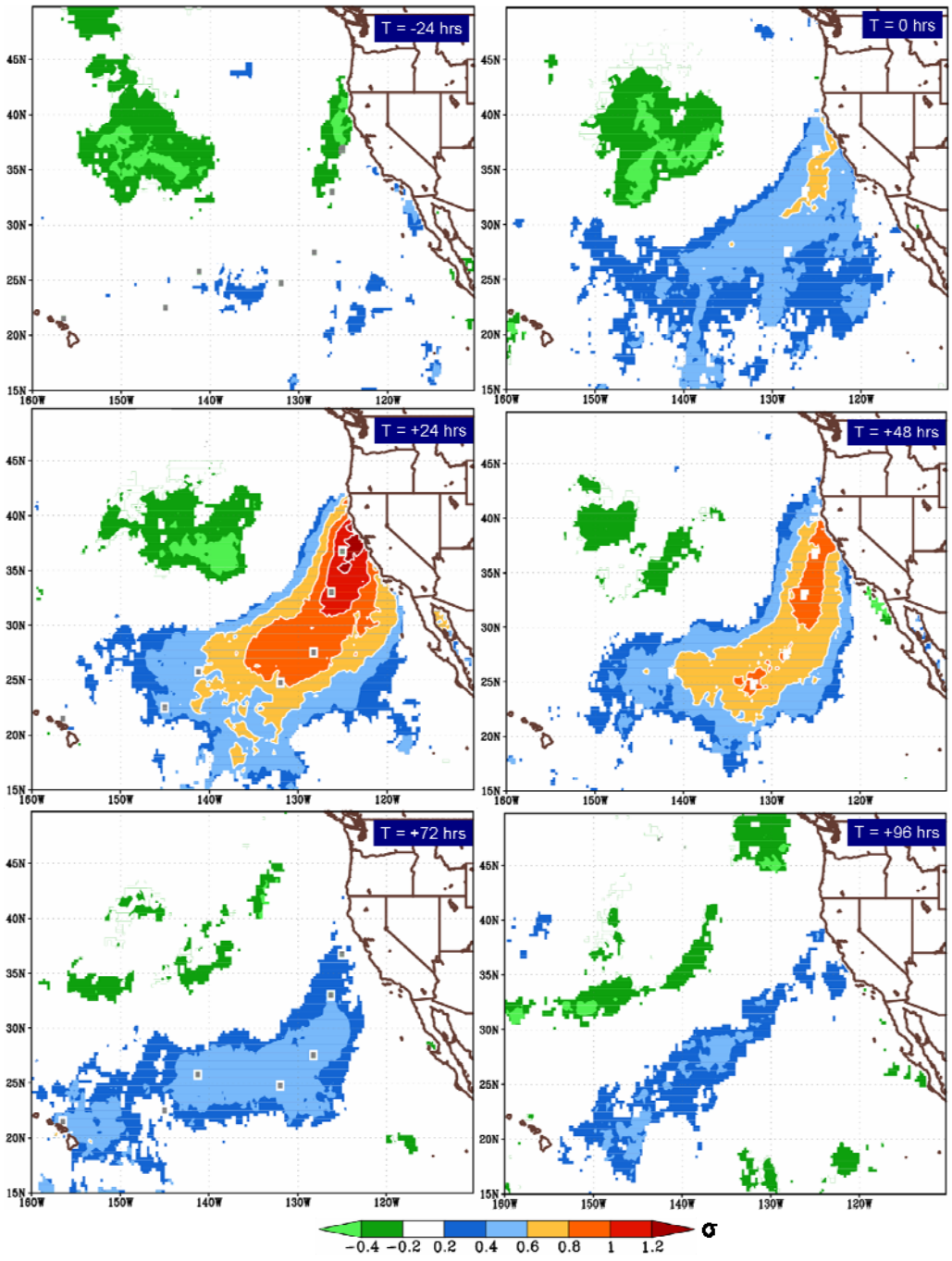

Figure 12: Composite evolution QSCAT wind anomalies for wind events identified at Pt Arena (B14) and listed in Table 3. Wind event composites are computed as in Figure 11, but for wind speed anomalies. Standardized anomalies are computed using a 30-day running mean and standard deviation for each pass separately to ensure removal of diurnal cycle. The contours and shading are in units of standard deviations. Shaded areas include only those positive grid values ranked 1st relative to 100 random composites from a montecarlo simulation. Negative contours are plotted only when the values rank in the bottom 10/100.

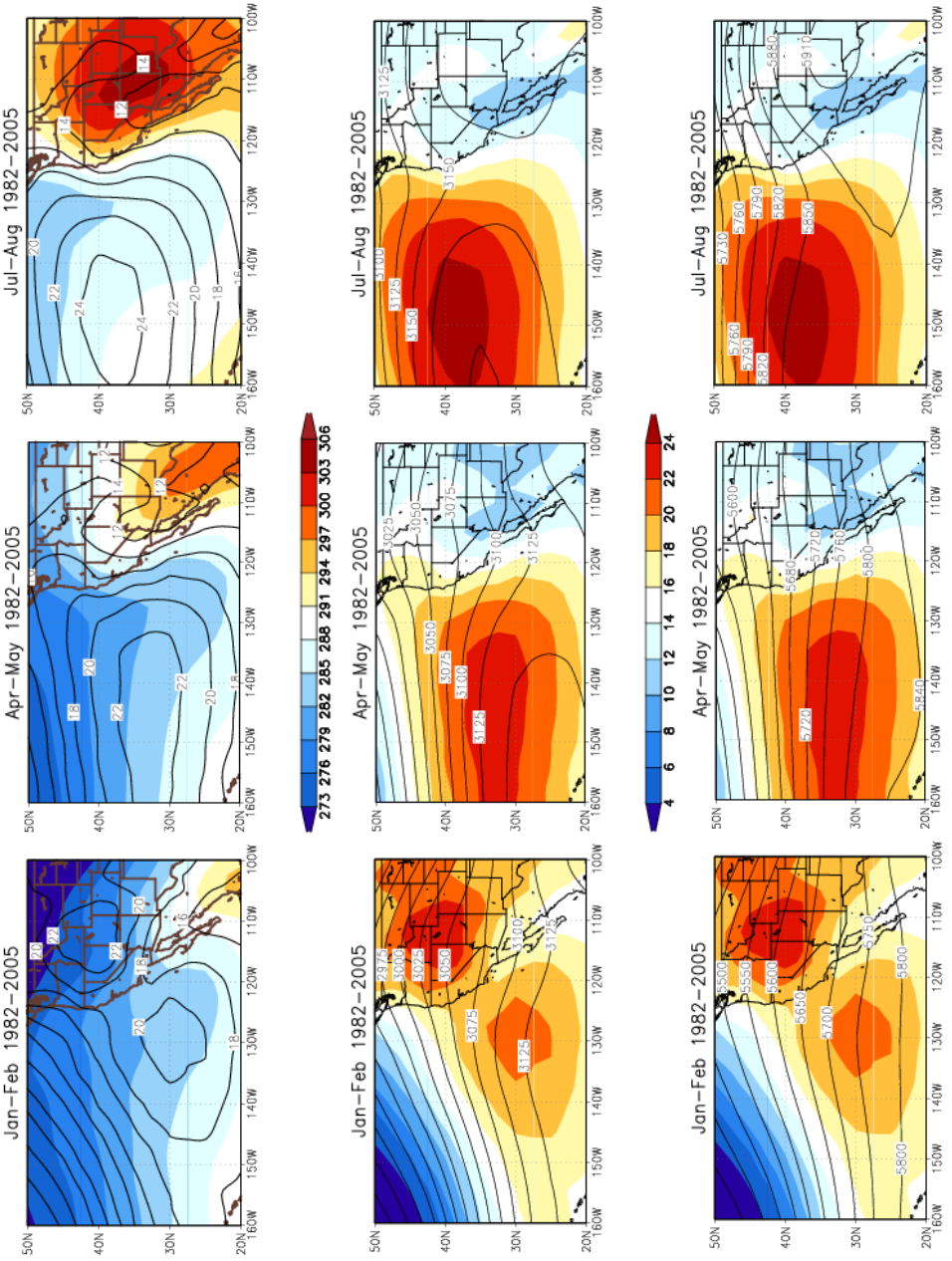

Figure 13: Top: Mean 925mb Air Temperature (shading, K) and SLP (contours, mb-1000). Middle: Mean SLP (shading, mb-1000) and 700mb heights (contours, m). Bottom: Mean SLP (shading, mb-1000) and 500mb heights (contours, m).

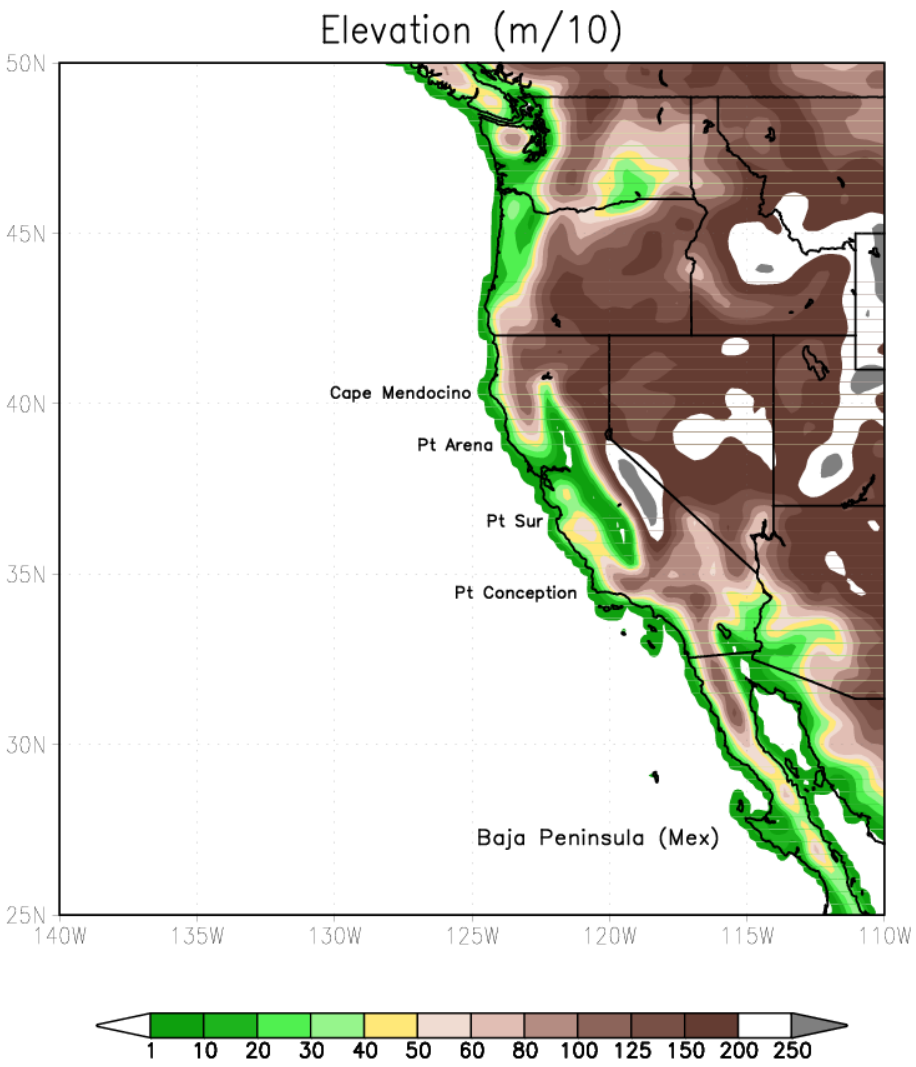

Figure 14: Terrain elevation at 25km resolution.

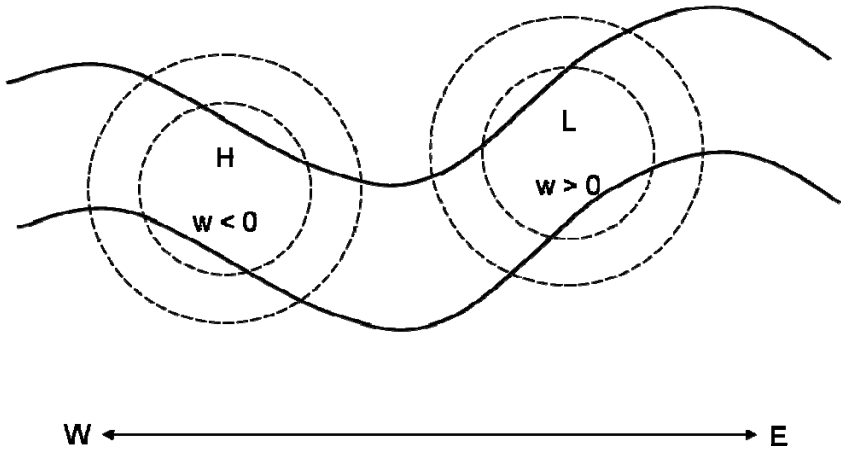

Figure 15: Schematic of vertical motion, w, associated with troughs. After Holton, 1992 Figures 6.11.

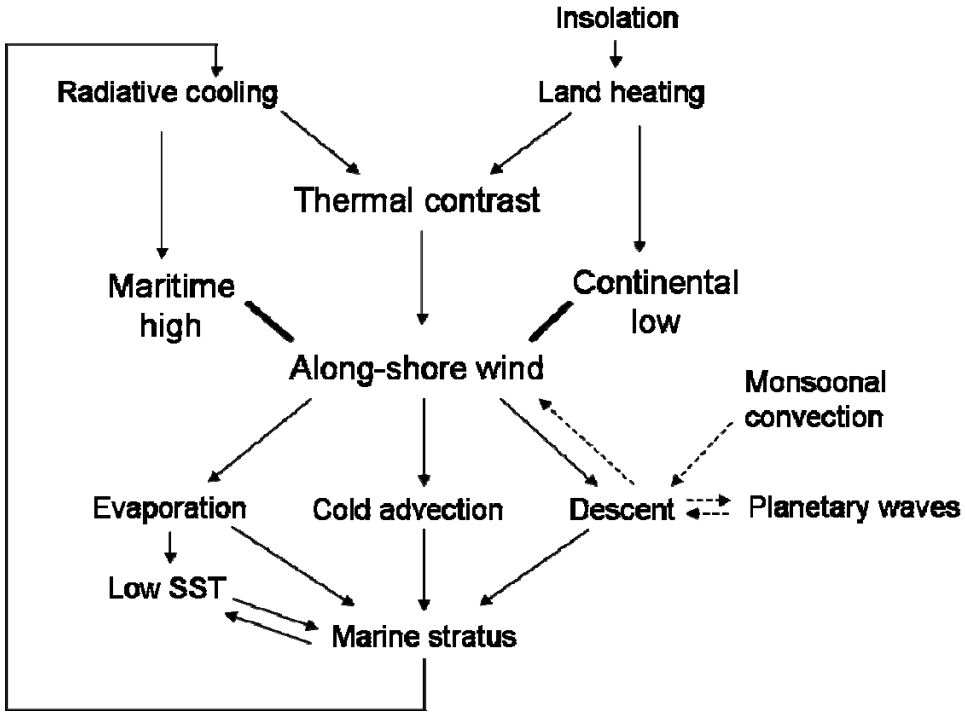

Figure 16: Schematic of forcing of the summertime subtropical anticyclone. After Miyasaka and Nakamura 2005 Figure 15.

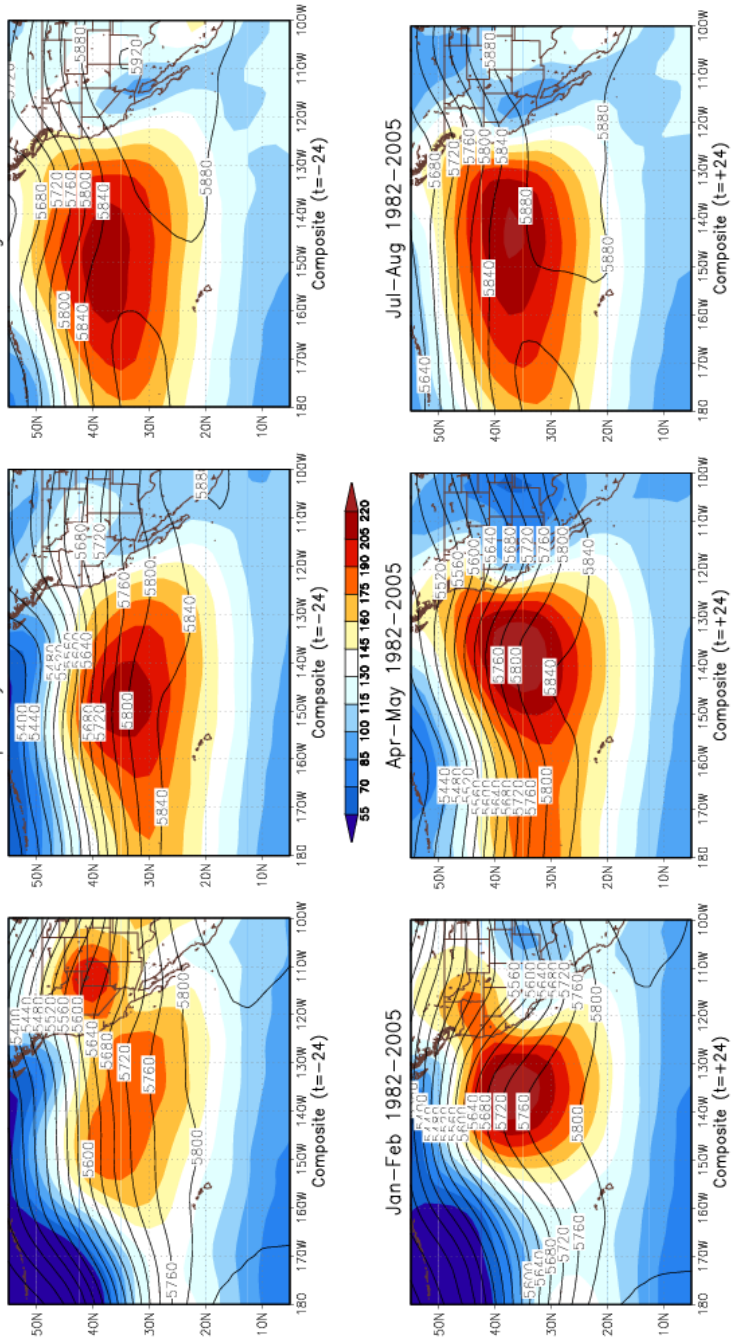

Figure 17: Composite of 1000mb heights (shading, m) and 500mb heights (contours, m) for lag-1 day (top) and lag+1 day (bottom) relative to initiation of wind events observed at NDBC buoy 46014 (39N, 124W).

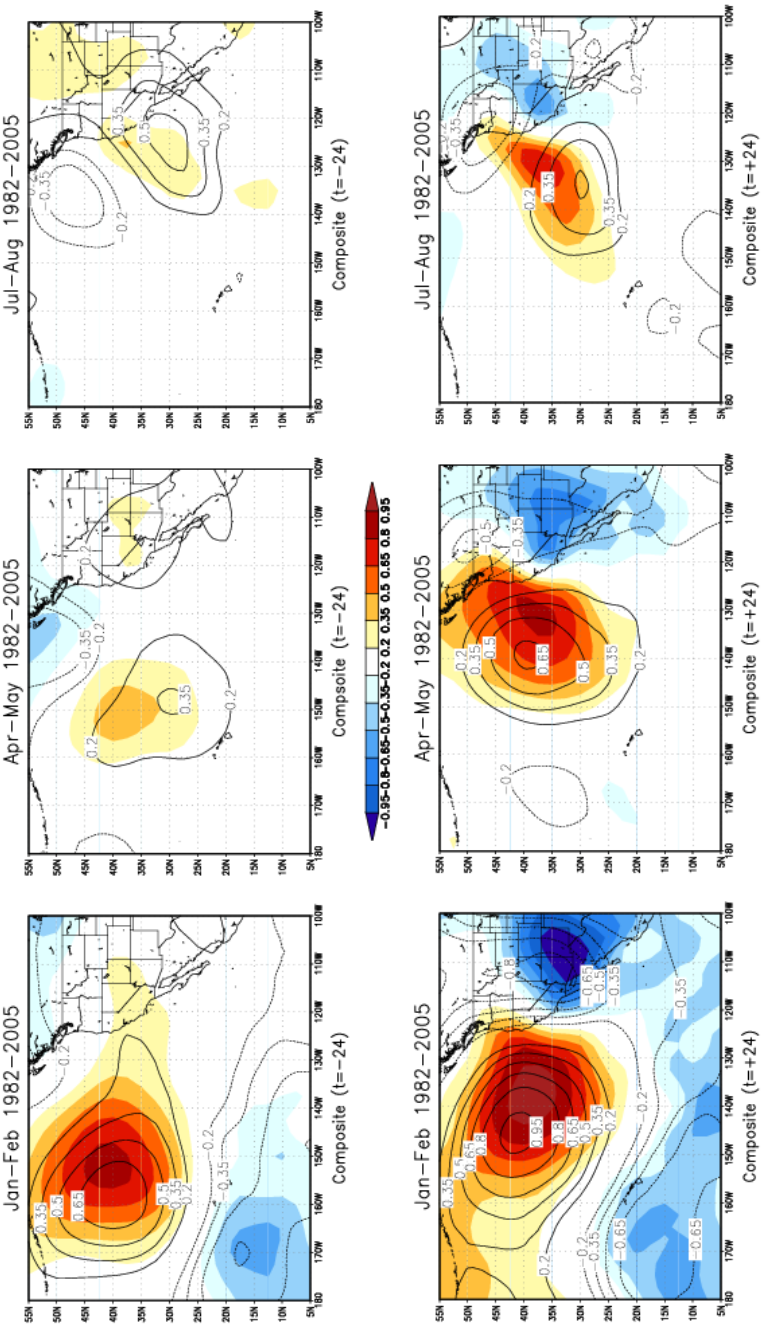

Figure 18: Composite of anomalies of 1000mb heights (shading) and 500mb heights (contours) for lag-1 day (top) and lag+1 day (bottom) relative to initiation of wind events observed at NDBC buoy 46014 (39N, 124W). Units are standard deviations.

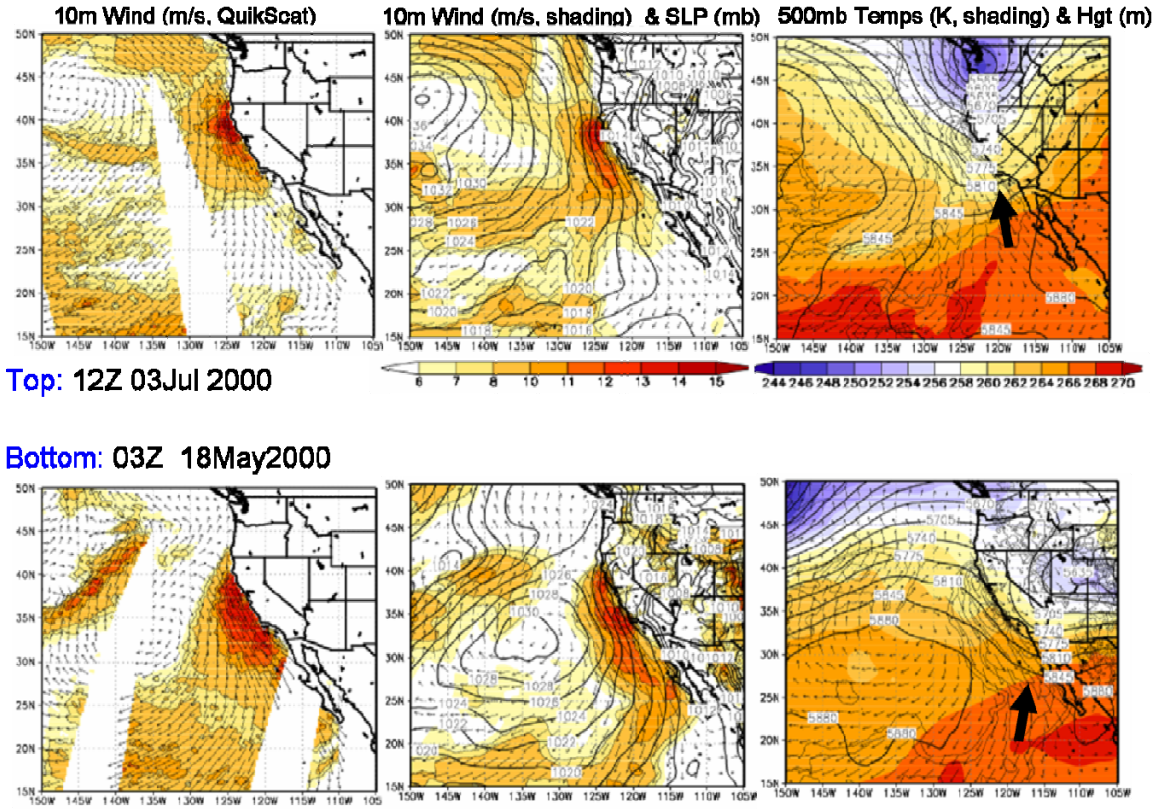

Figure 19: Wind event case examples of a strong trough on 03Jul 2000 (top) and 18May 2000 (Bottom). Left panels show QuikScat wind speed (m/s) and direction estimates. Middle panels show SLP (contours, mb) and 10m wind speed (shading, m/s) from NARR. Right panels show 500mb heights (contours, m) and 500mb temperatures (shading, K). Black arrows point toward the trough location on the 500mb surface (right panels).

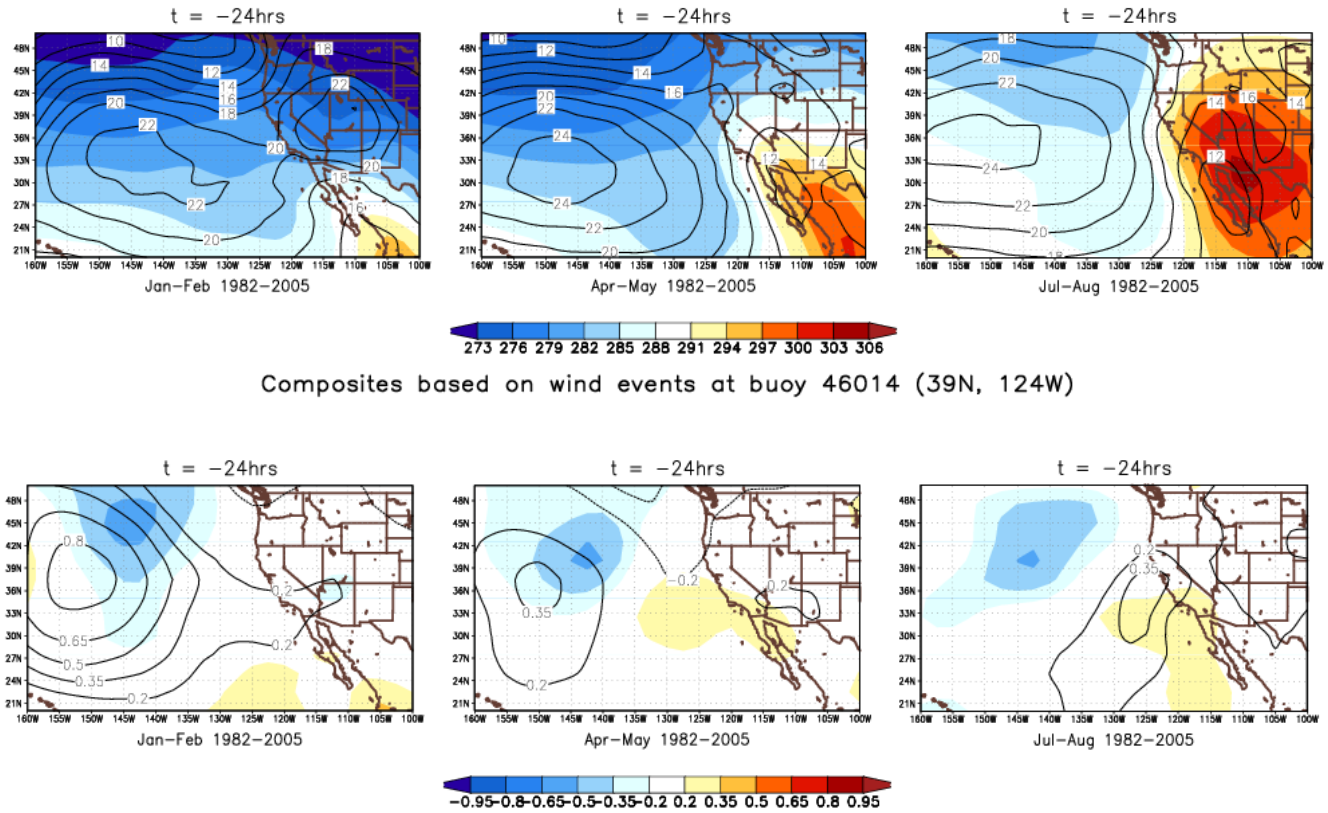

Figure 20: Composite of 925mb Air Temperature fields (shading, K) and SLP (contours, mb-1000) for lag-1 day (top) and composite of anomalies of 925mb Air Temperatures (shading) and SLP (contours) for lag-1 day (bottom) relative to initiation of wind events observed at NDBC buoy 46014 (39N, 124W). Units are Kelvin (top) and standard deviations (bottom).

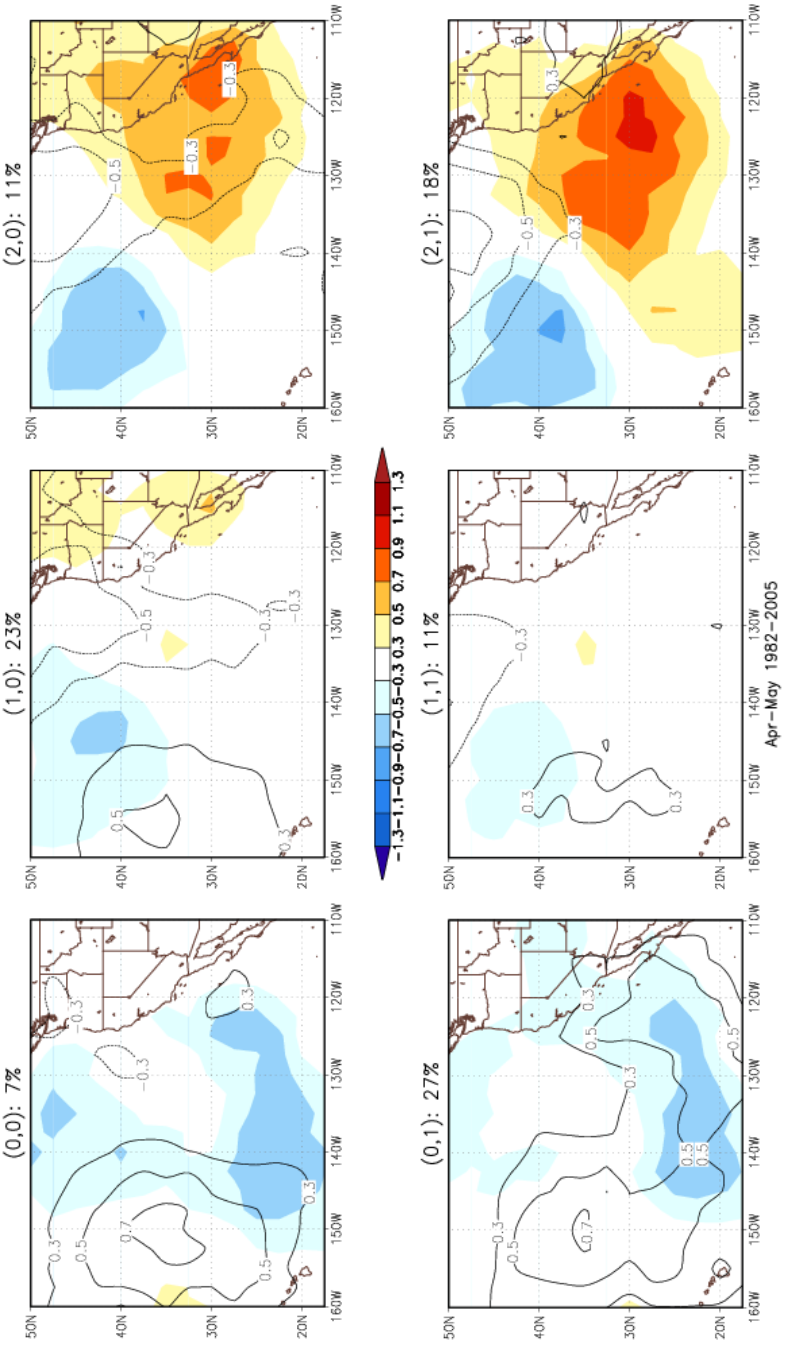

Figure 21. Joint SOM of composite of SLP (contours) and 925mb Air Temperature (shading) anomalies shown in the top middle panel of Figure 18 (Apr-May, lag-1).

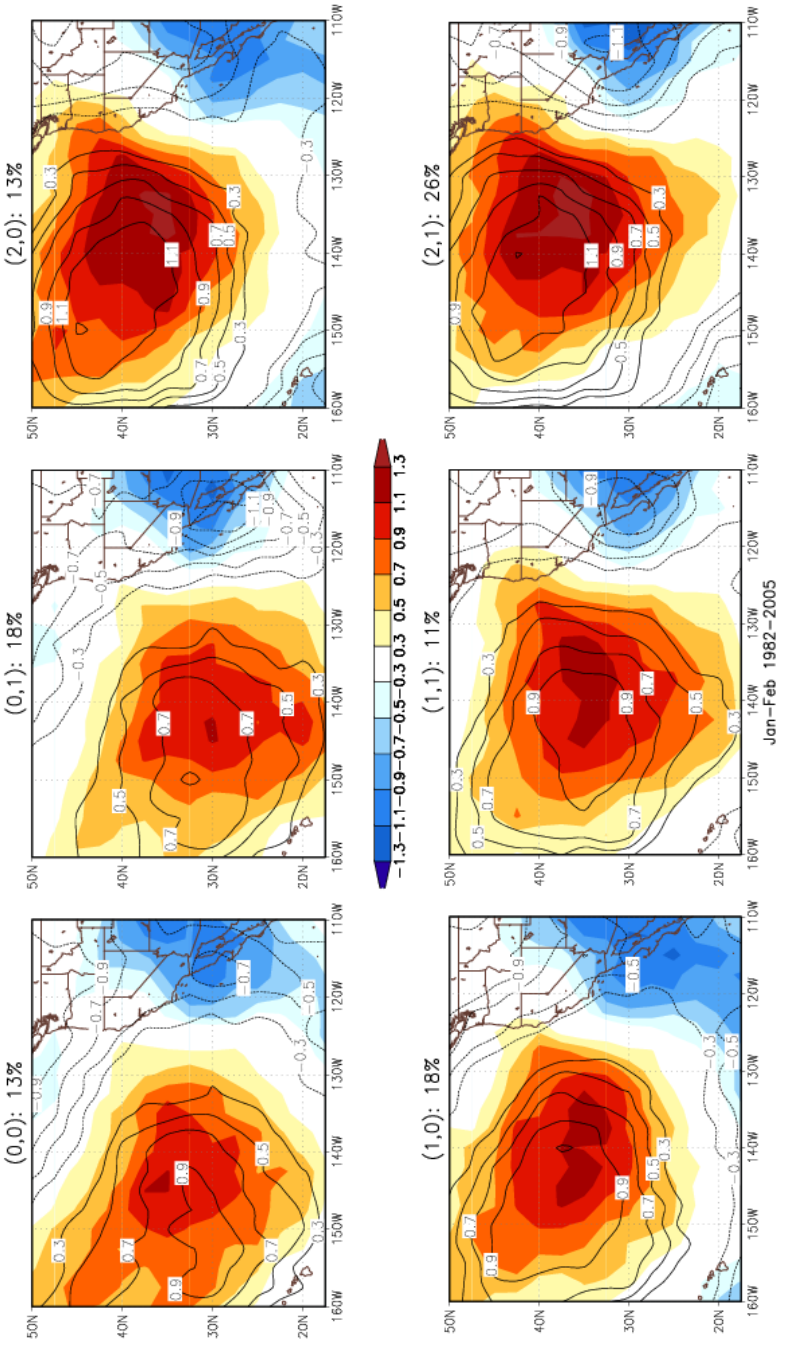

Figure 22: Joint SOM of composite of SLP and 500mb height anomalies shown in the bottom left panel of Figure 18 (Jan-Feb, lag+1).

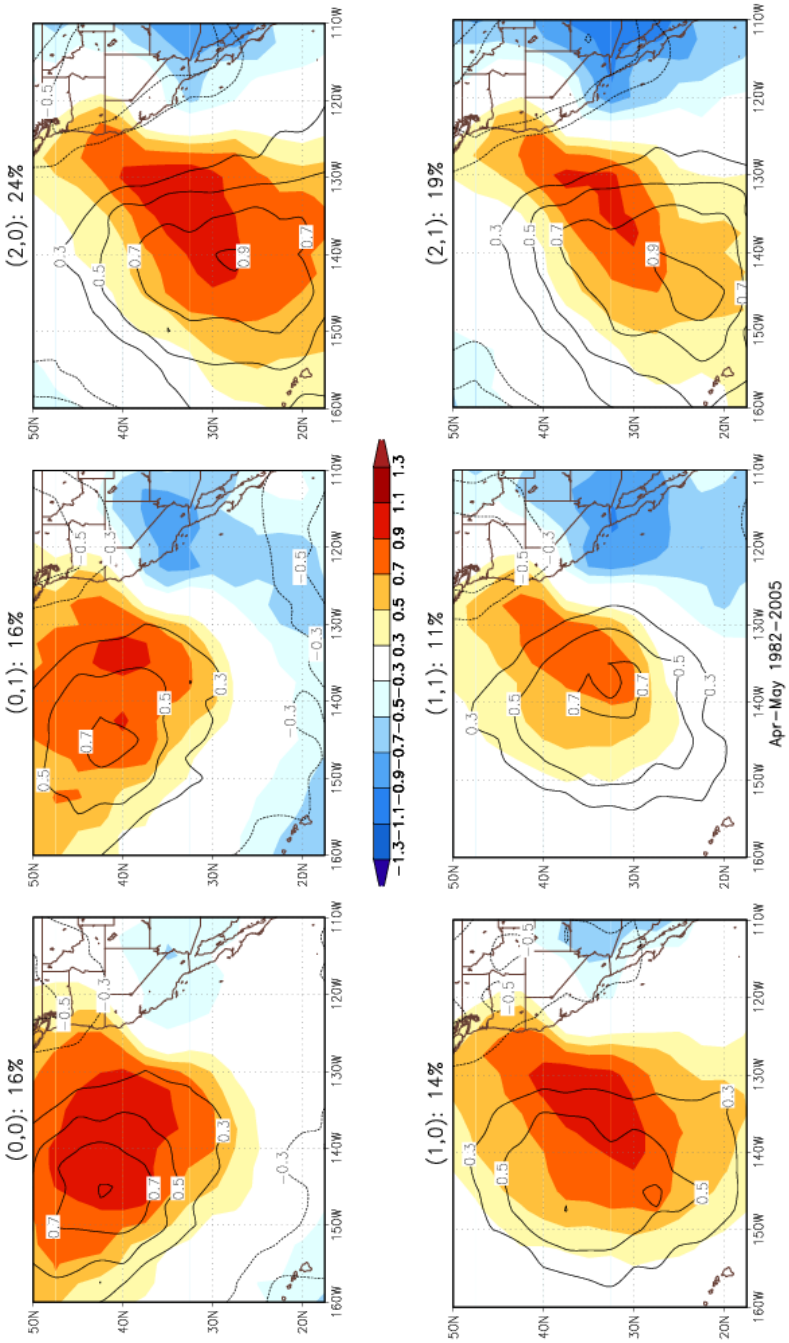

Figure 23: Joint SOM of composite of SLP and 500mb height anomalies shown in the bottom middle panel of Figure 18 (Apr-May, lag+1).

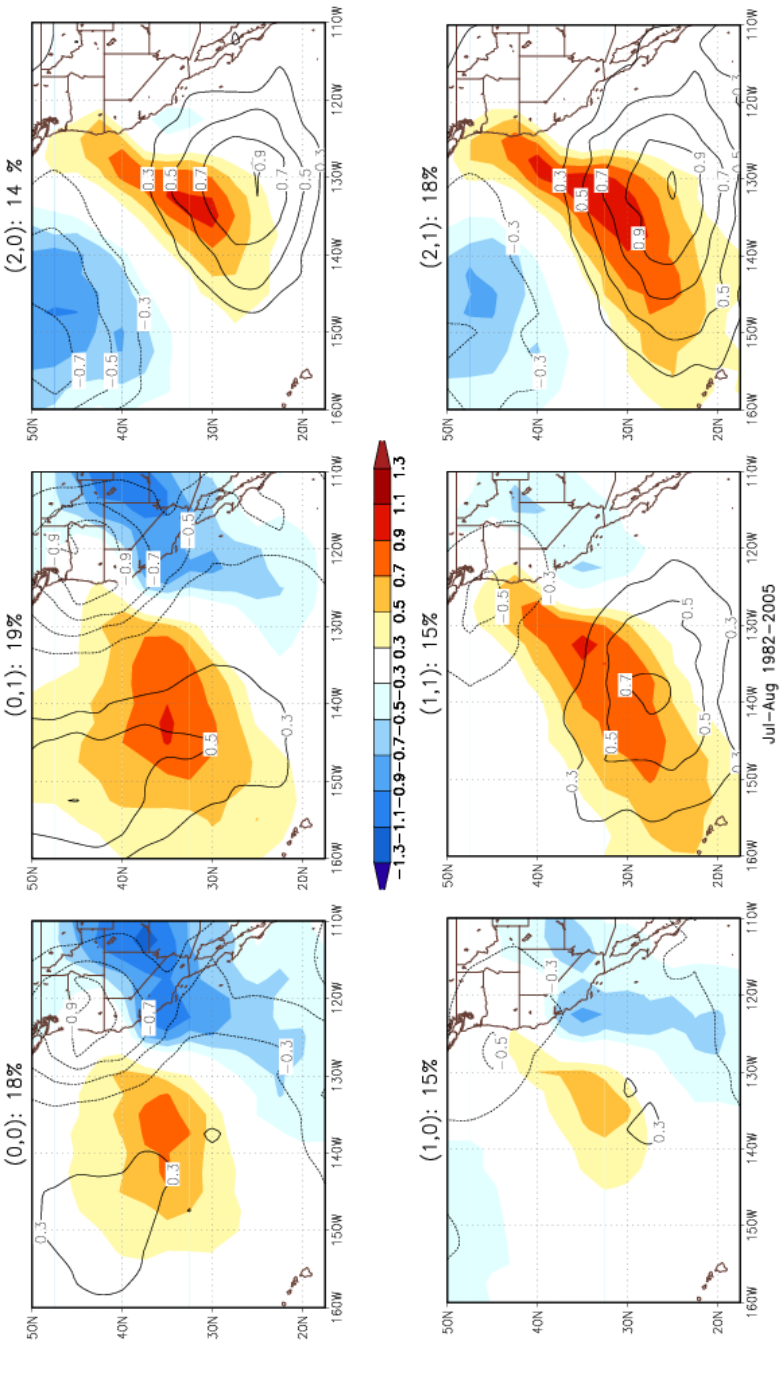

Figure 24: Joint SOM of composite of SLP and 500mb height anomalies shown in the bottom right panel of Figure 18 (Jul-Aug, lag+1).

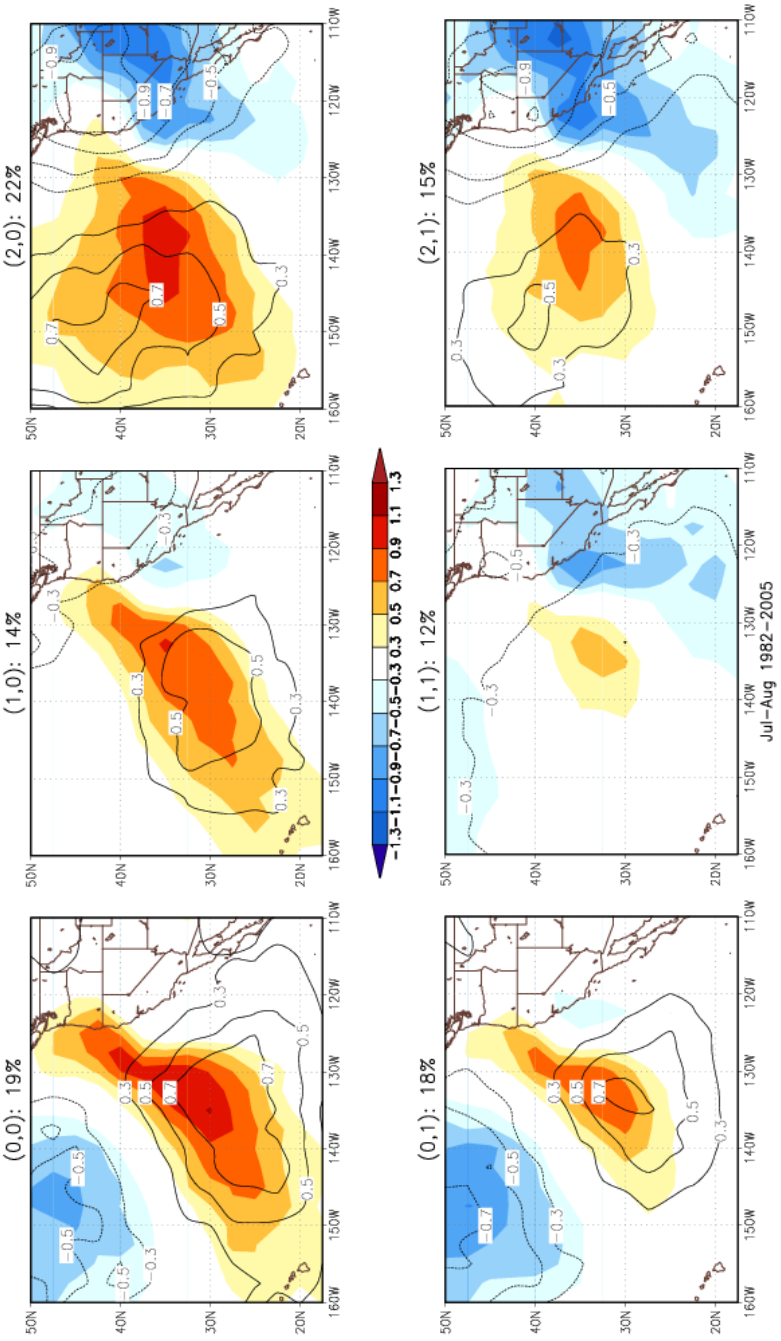

Figure 25: Joint SOM of composite of SLP and 700mb height anomalies for lag+1 summer (Jul-Aug) composites.

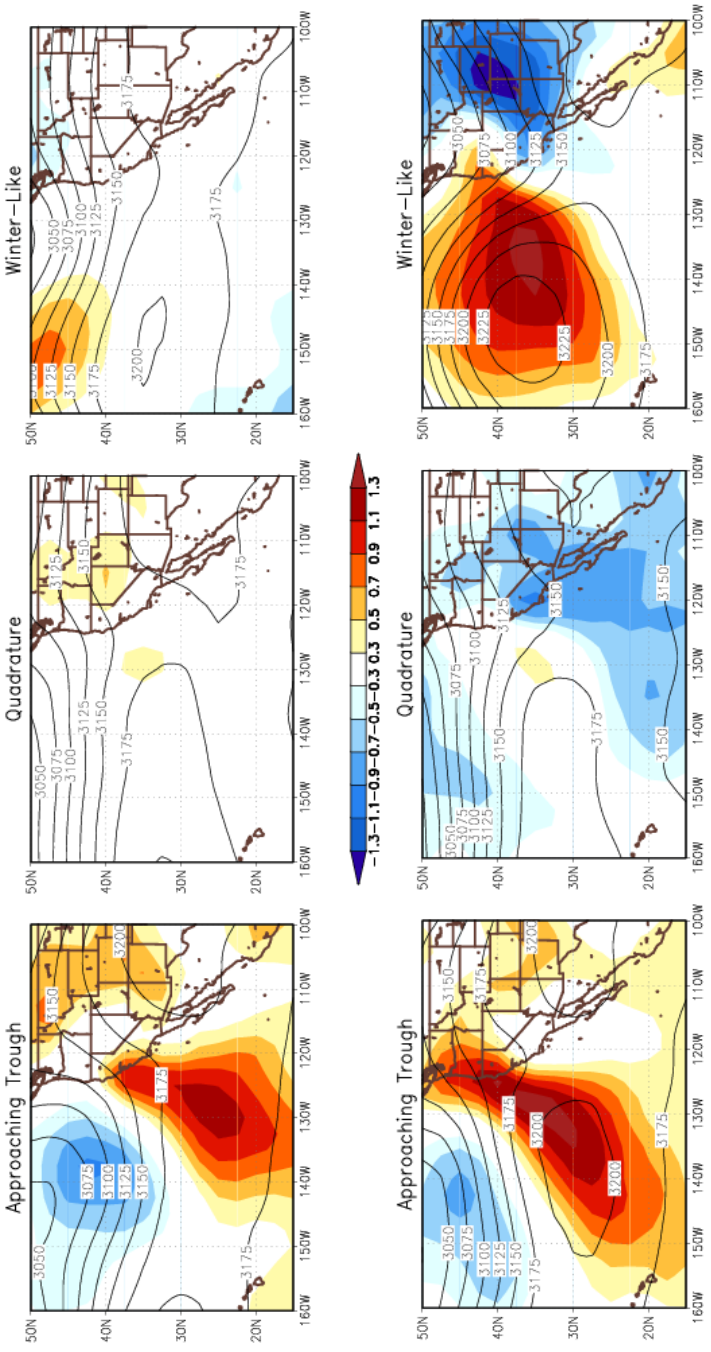

Figure 26: Conditional composite of 700mb geopotential height (contours) and SLP (shading) in sigma units. The conditional composite is described in Section 2.5.1.

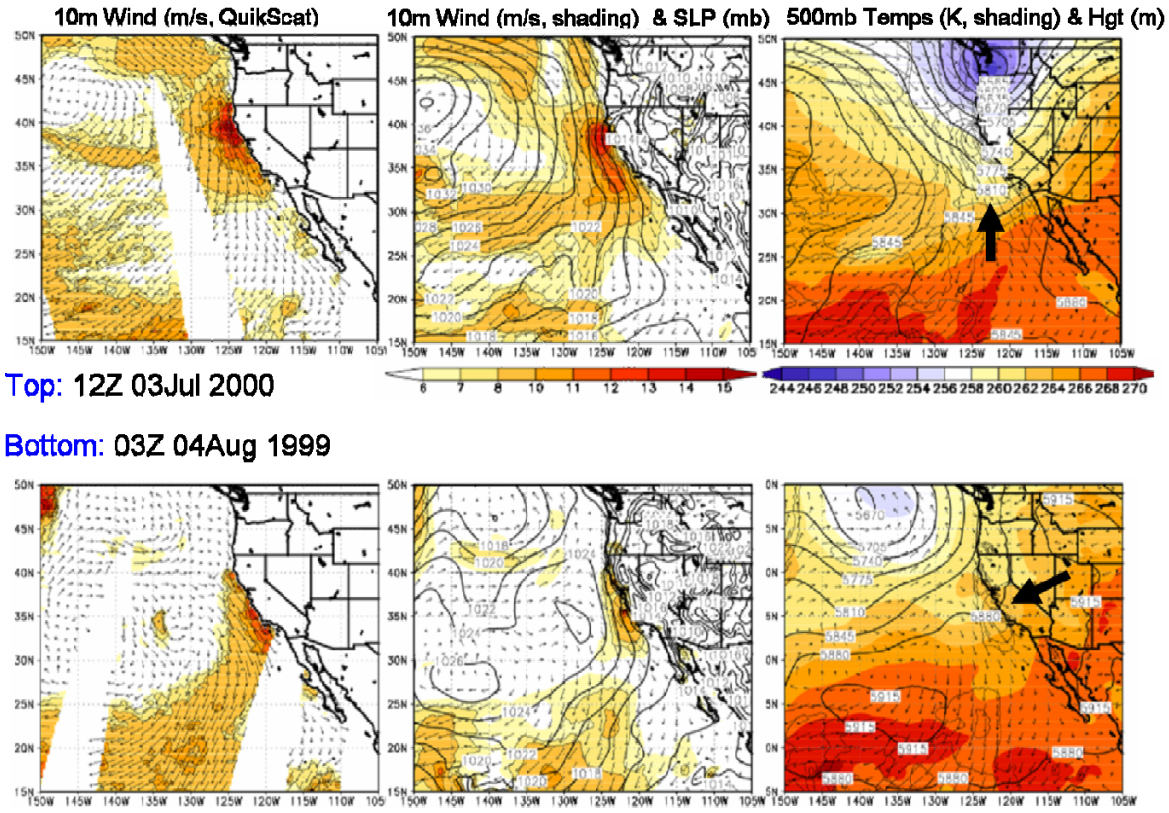

Figure 27: Wind event case examples of a strong trough on 03Jul 2000 (top) and a weak trough on 04Aug 1999 (Bottom). Left panels show QuikScat wind speed (m/s) and direction estimates. Middle panels show SLP (contours, mb) and 10m wind speed (shading, m/s) from NARR. Right panels show 500mb heights (contours, m) and 500mb temperatures (shading, K). Black arrows point toward the trough location on the 500mb surface (right panels).

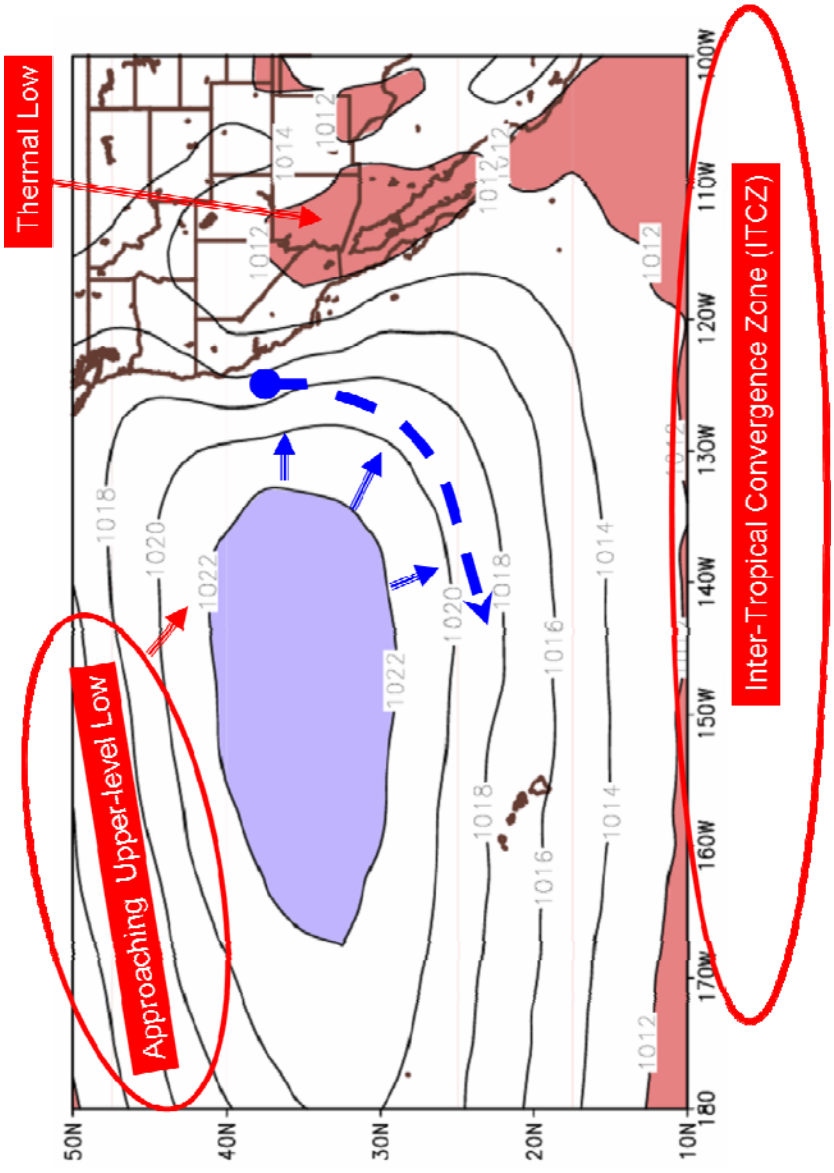

Figure 28: Schematic of southeast migration hypothesis. The contours indicate SLP (mb). The location of the North Pacific High (blue) and the termal low and ITCZ (red) and as indicated.

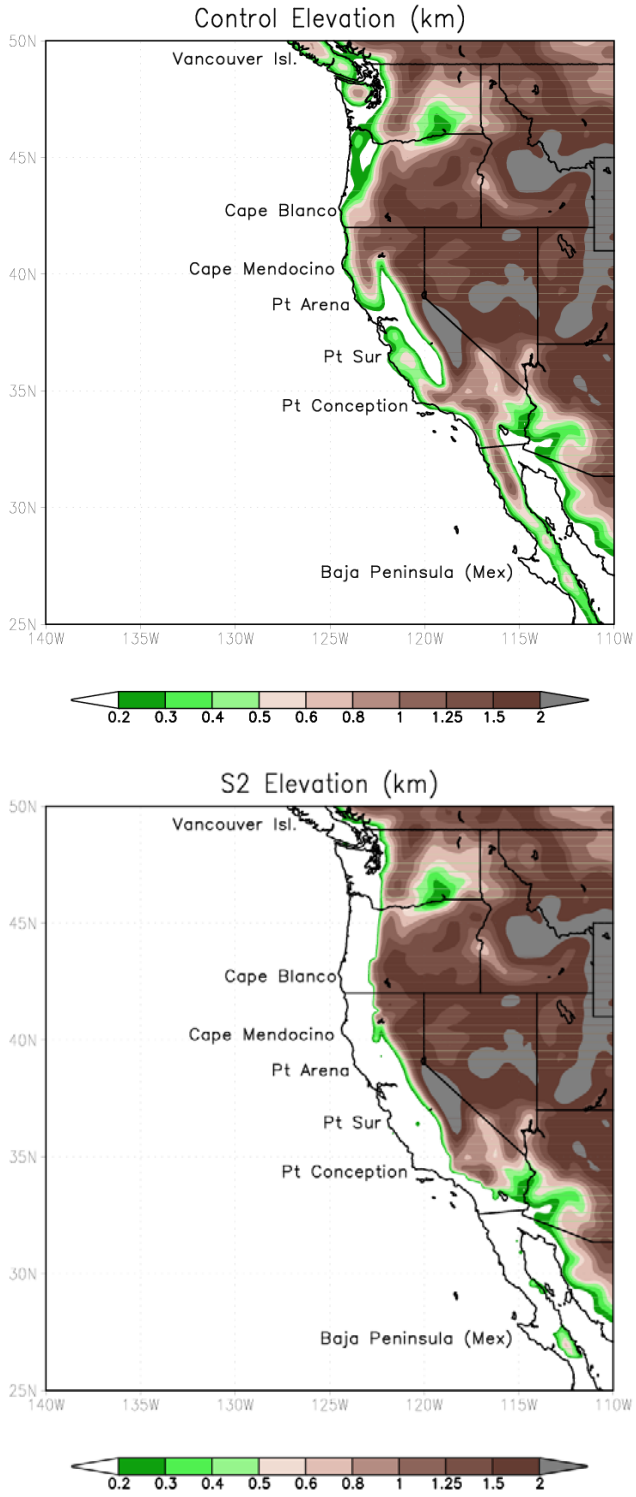

Figure 29: Terrain for control run (Top) and the flattened terrain used for the second sensitivity test (Bottom).

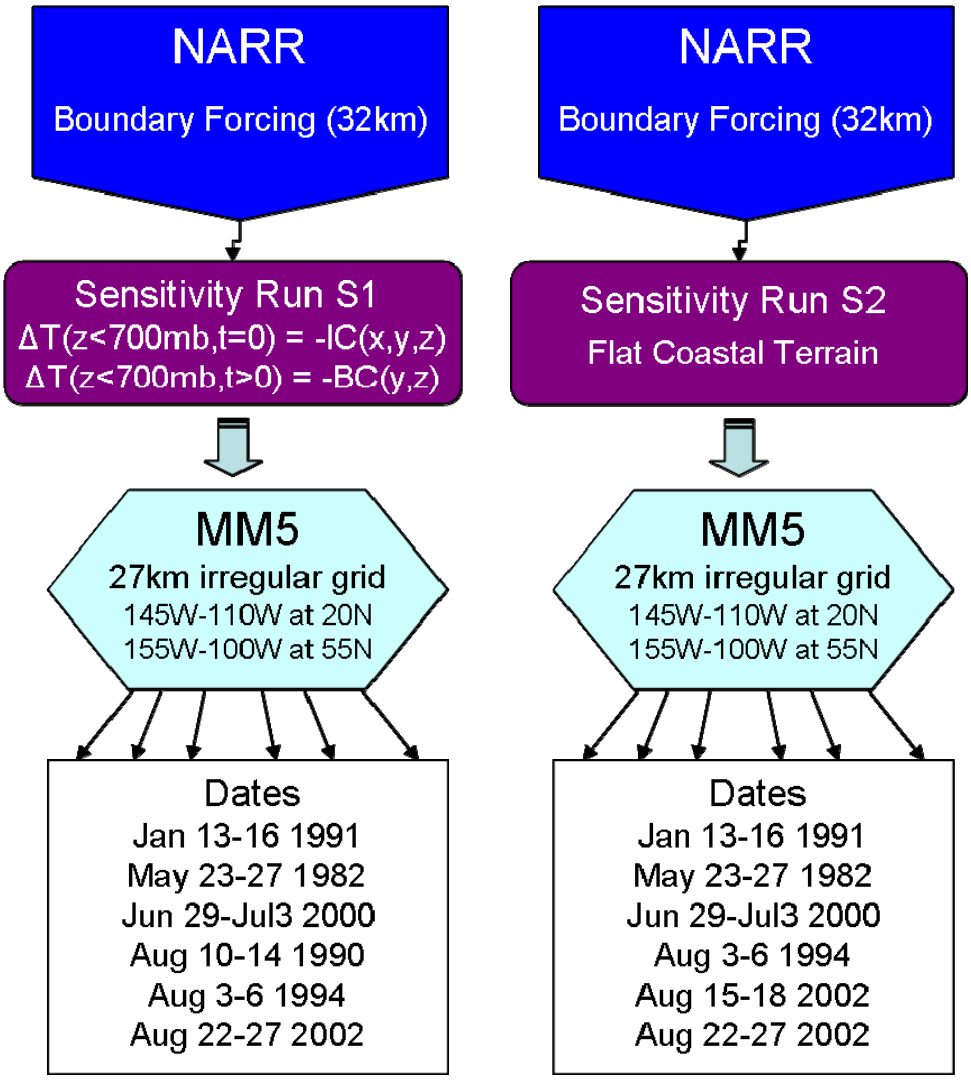

Figure 30: Flowcharts of sensitivity tests.

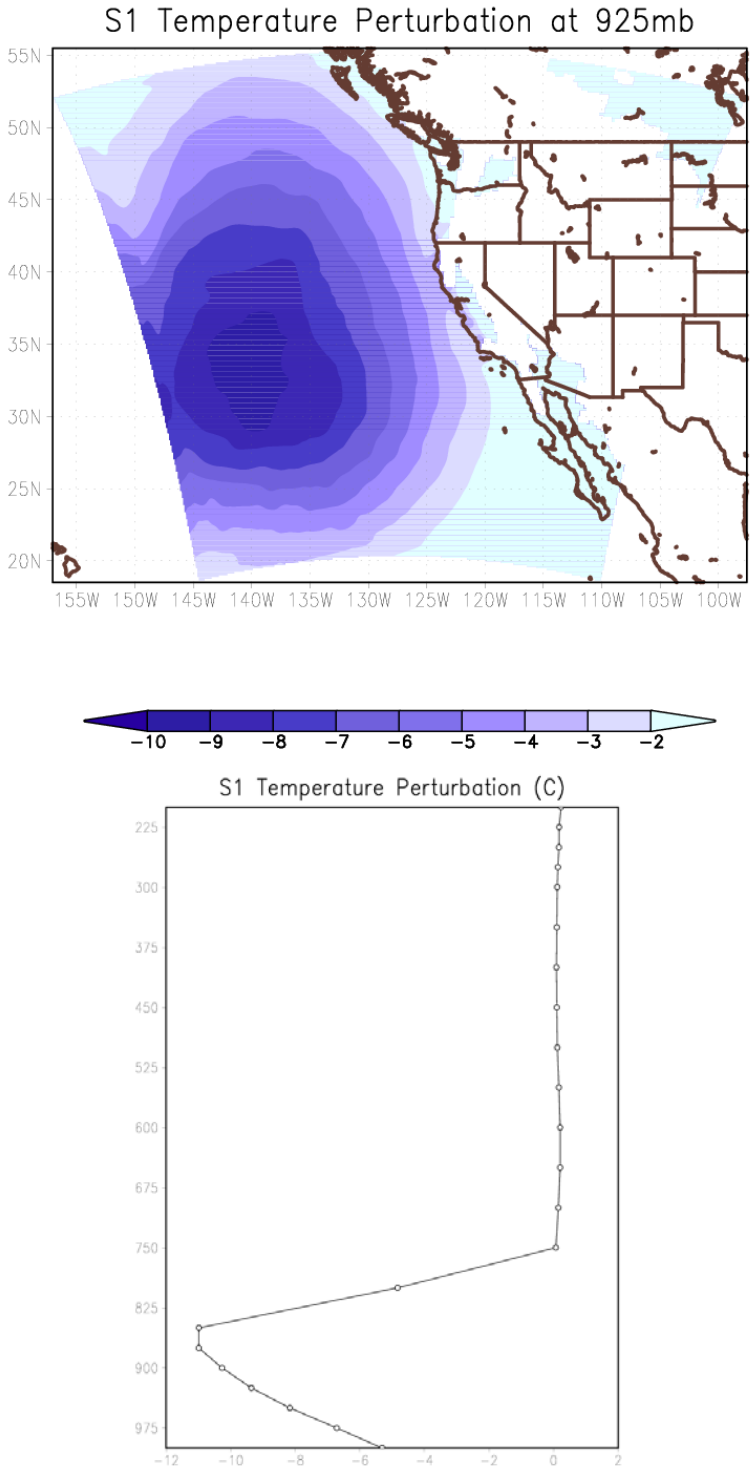

Figure 31: Initial condition for S1. Gaussian distribution at 925mb (Top). The lower panel shows the vertical profile at 140W, 35N.

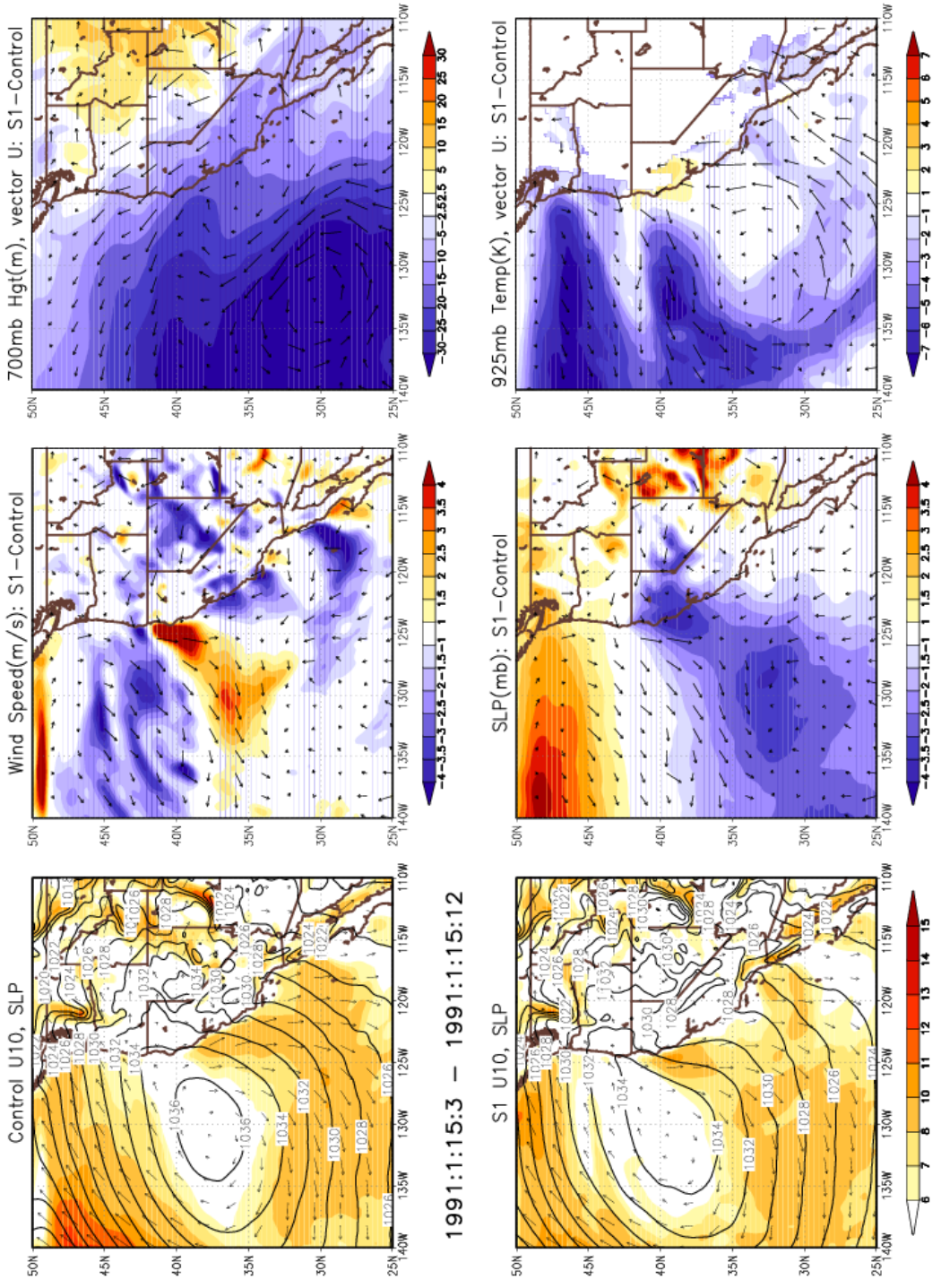

Figure 32: Winter Temperature Perturbation (S1) sensitivity test. Left panels show SLP (mb) and wind speed (m/s). Center panels show differences in wind speed (top, m/s) and SLP (bottom, mb). The right panels show differences in 700mb heights (top, m) and 925mb temperatures (bottom, K).

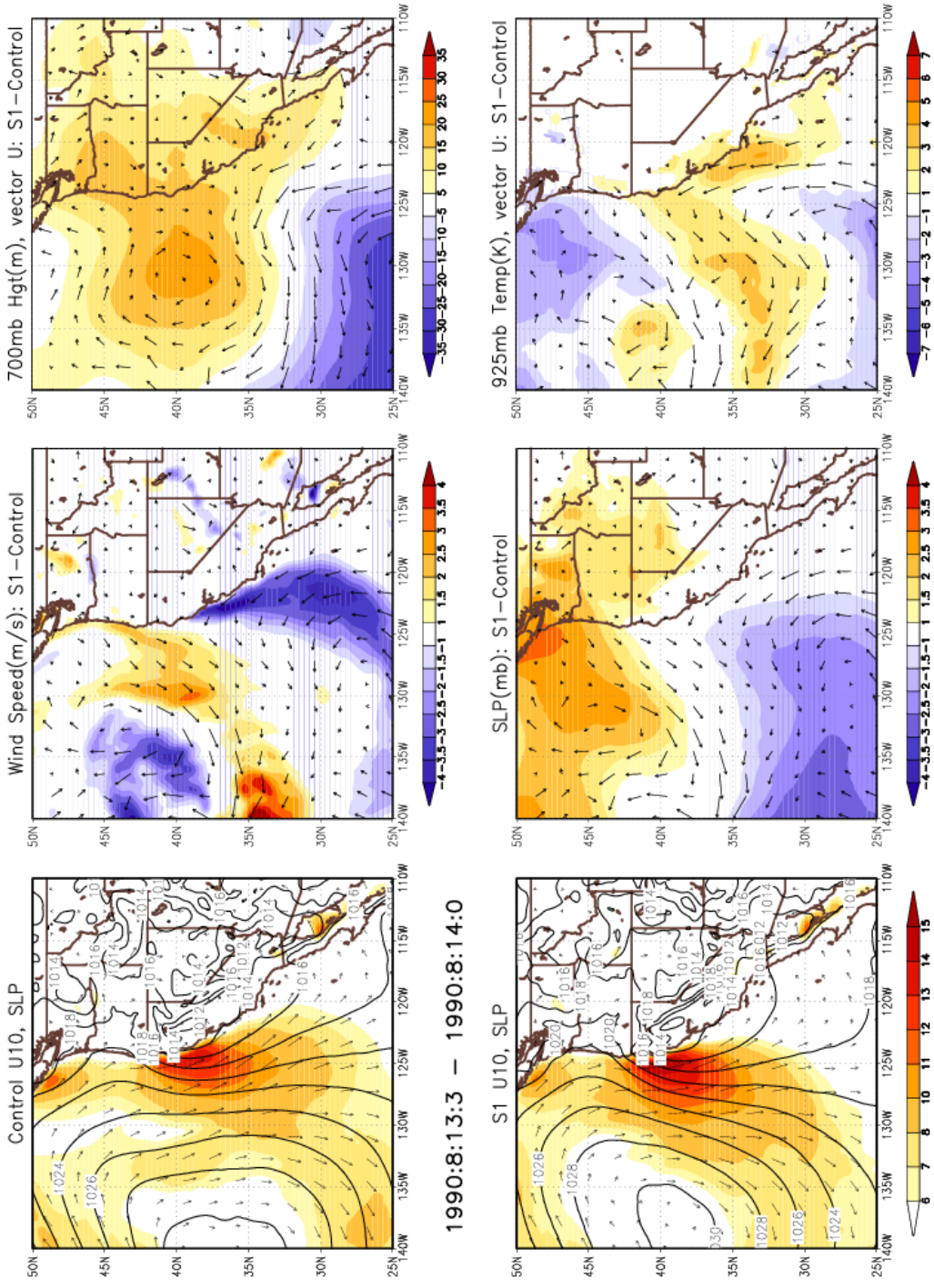

Figure 33: Summer Temperature Perturbation (S1) sensitivity test. Left panels show SLP (mb) and wind speed (m/s). Center panels show differences in wind speed (top, m/s) and SLP (bottom, mb). The right panels show differences in 700mb heights (top, m) and 925mb temperatures (bottom, K).

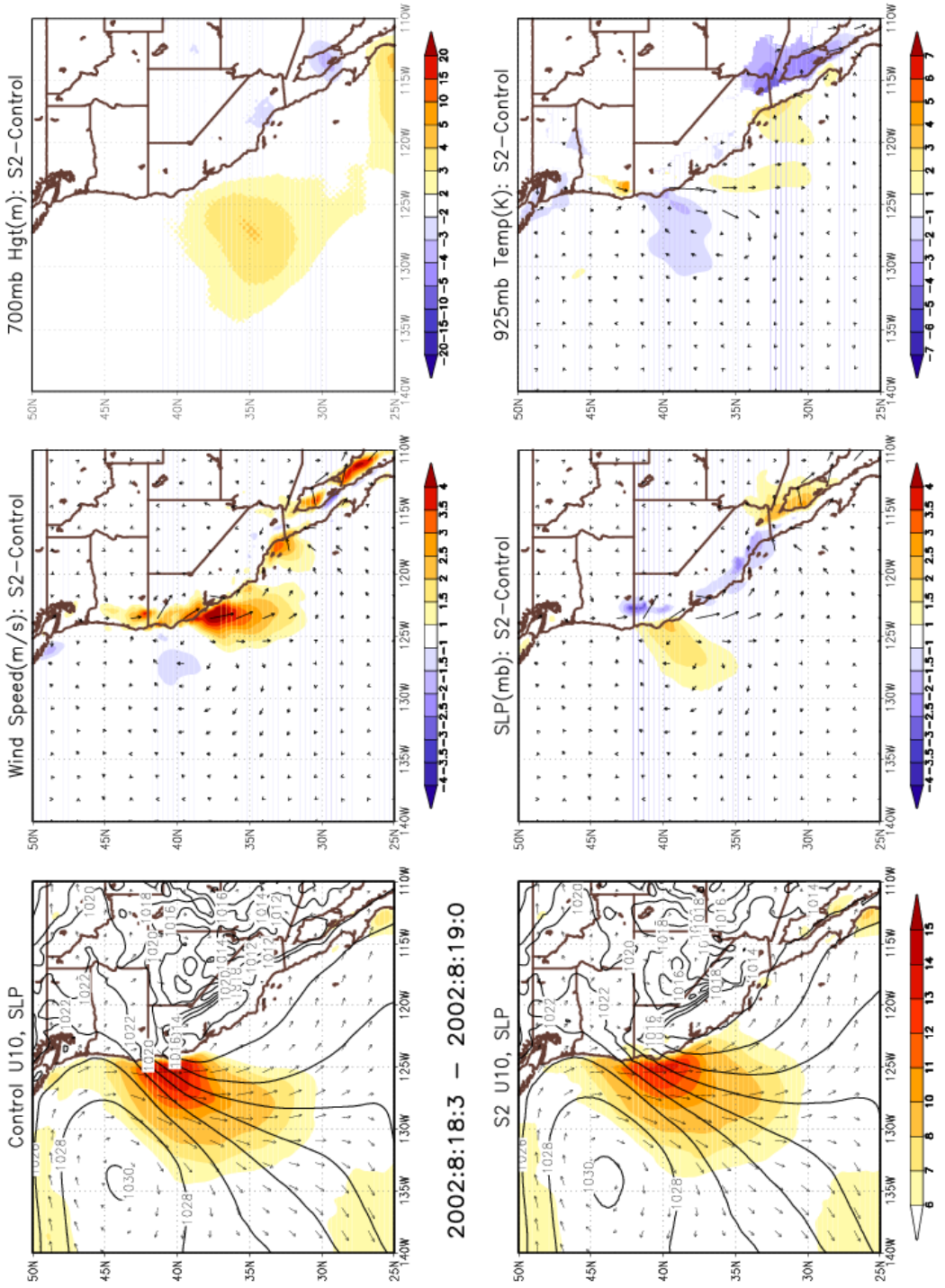

Figure 34: Summer flat terrain (S2) sensitivity test. Left panels show SLP (mb) and wind speed (m/s). Center panels show differences in wind speed (top, m/s) and SLP (bottom, mb). The right panels show differences in 700mb heights (top, m) and 925mb temperatures (bottom, K).

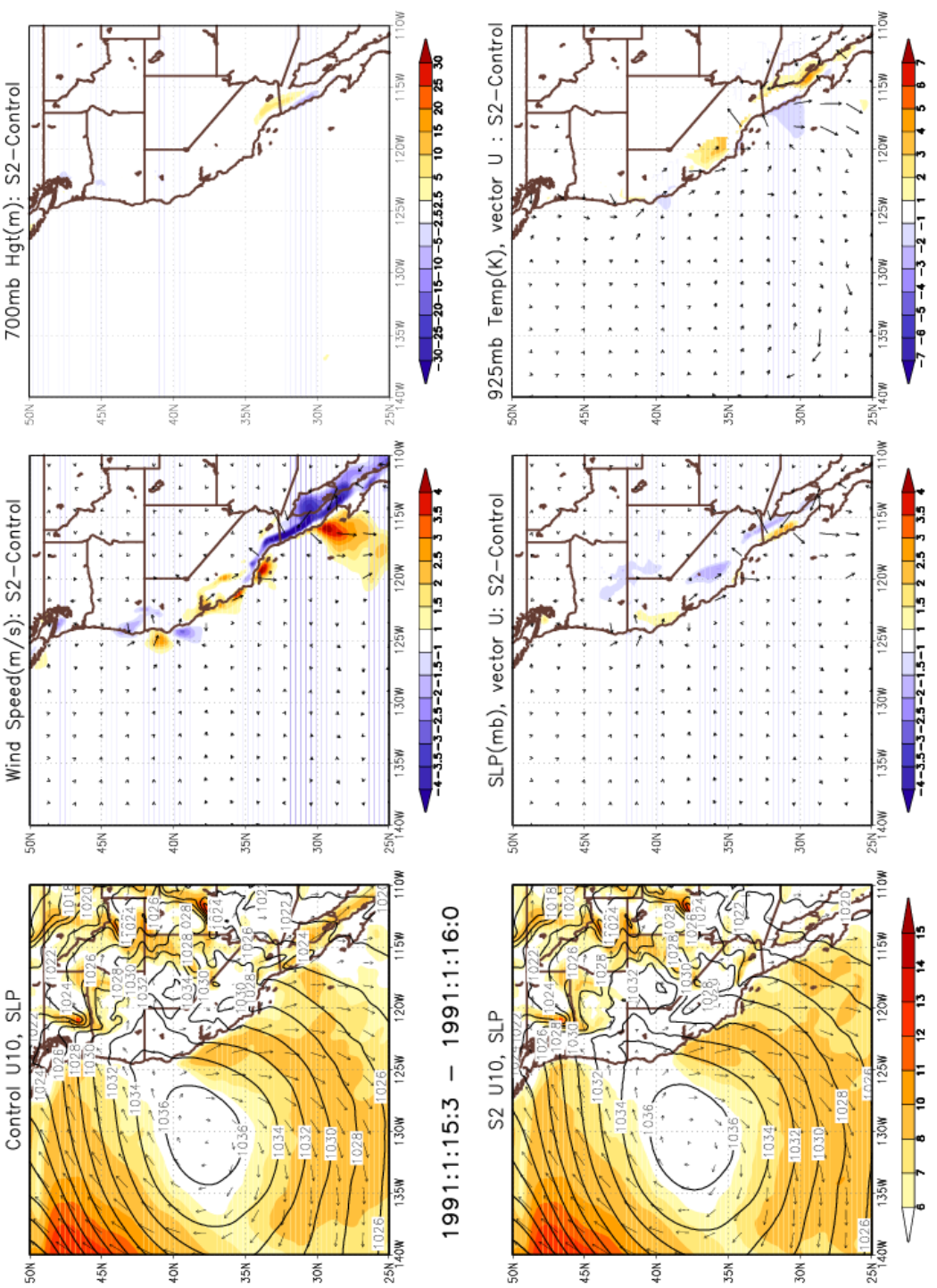

Figure 35: Winter flat terrain (S2) sensitivity test. Left panels show SLP (mb) and wind speed (m/s). Center panels show differences in wind speed (top, m/s) and SLP (bottom, mb). The right panels show differences in 700mb heights (top, m) and 925mb temperatures (bottom, K).

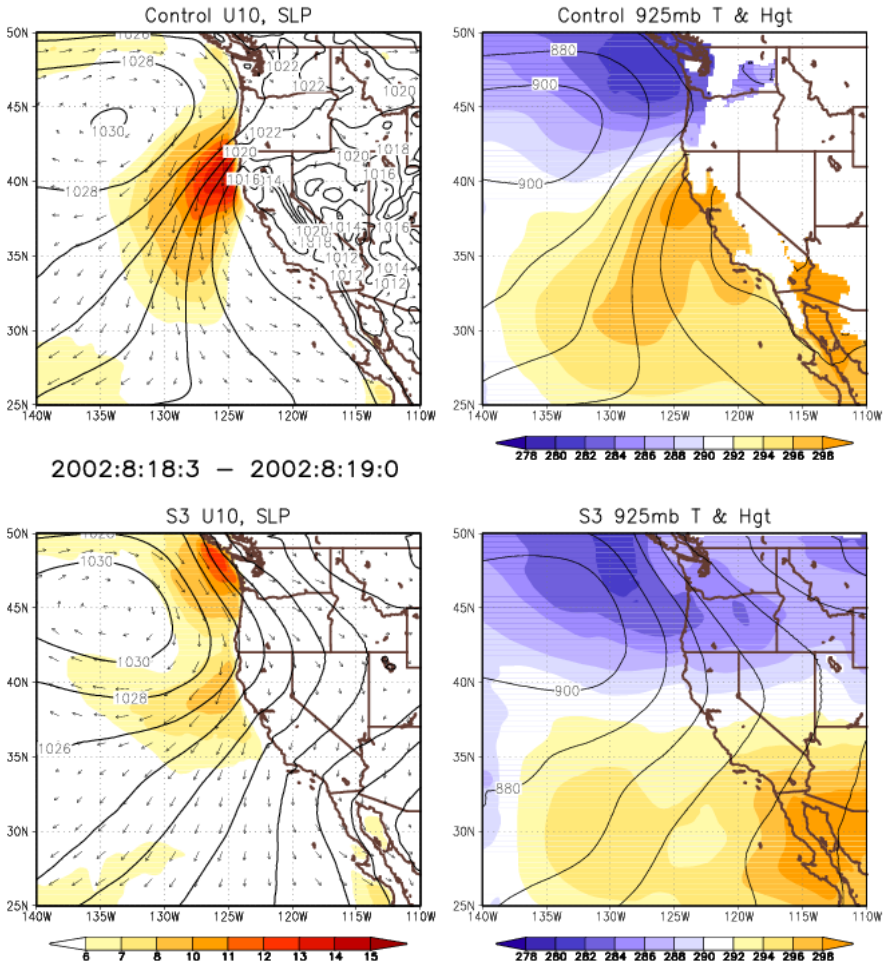

Figure 36: Summer "no terrain" sensitivity test. This one case was run with terrain above 200m removed everywhere in the domains shown in Figure 29. Sensitivity experiment results are shown in the lower panels with control run in top panels. Left panels show SLP (mb) and wind speed (m/s). Right panels show 925mb level height (m) and temperature (K).

APPENDIX

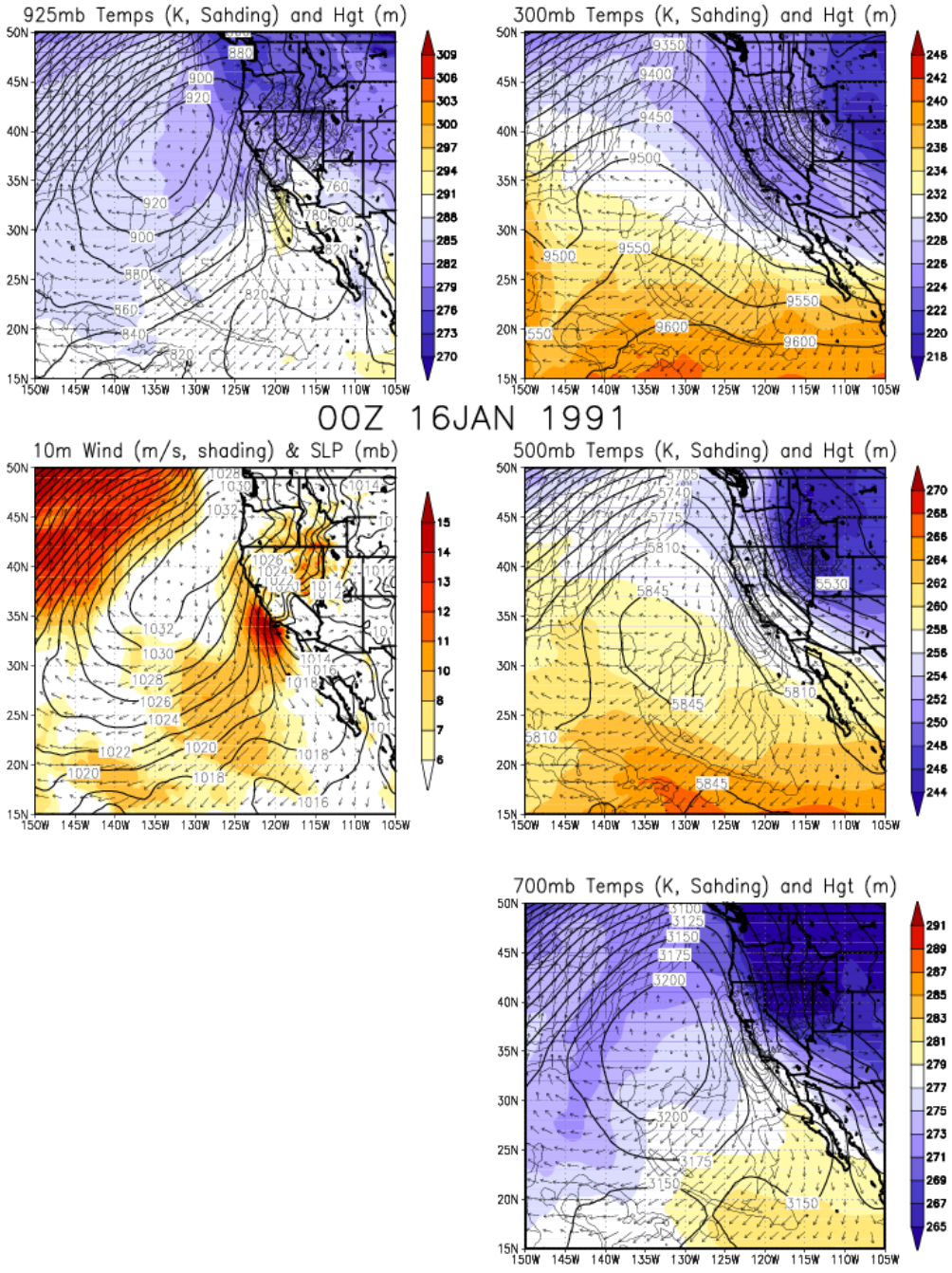

Appendix Figure A1: Wind event case study. The bottom left-panel shows QuikScat wind speed and direction estimates. The other panels show NARR fields at the specified levels.

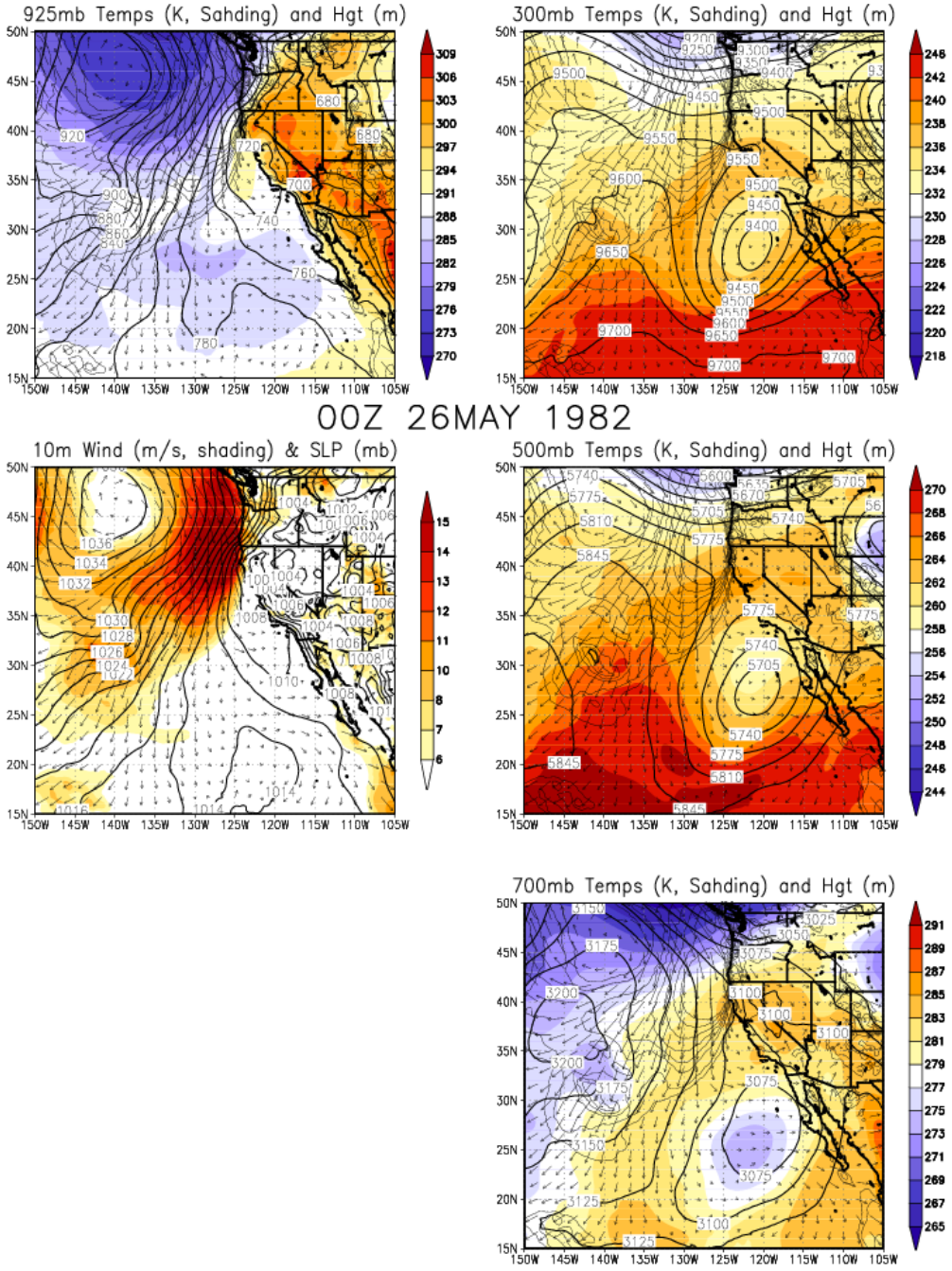

Appendix Figure A2: Wind event case study. The bottom left-panel shows QuikScat wind speed and direction estimates. The other panels show NARR fields at the specified levels.

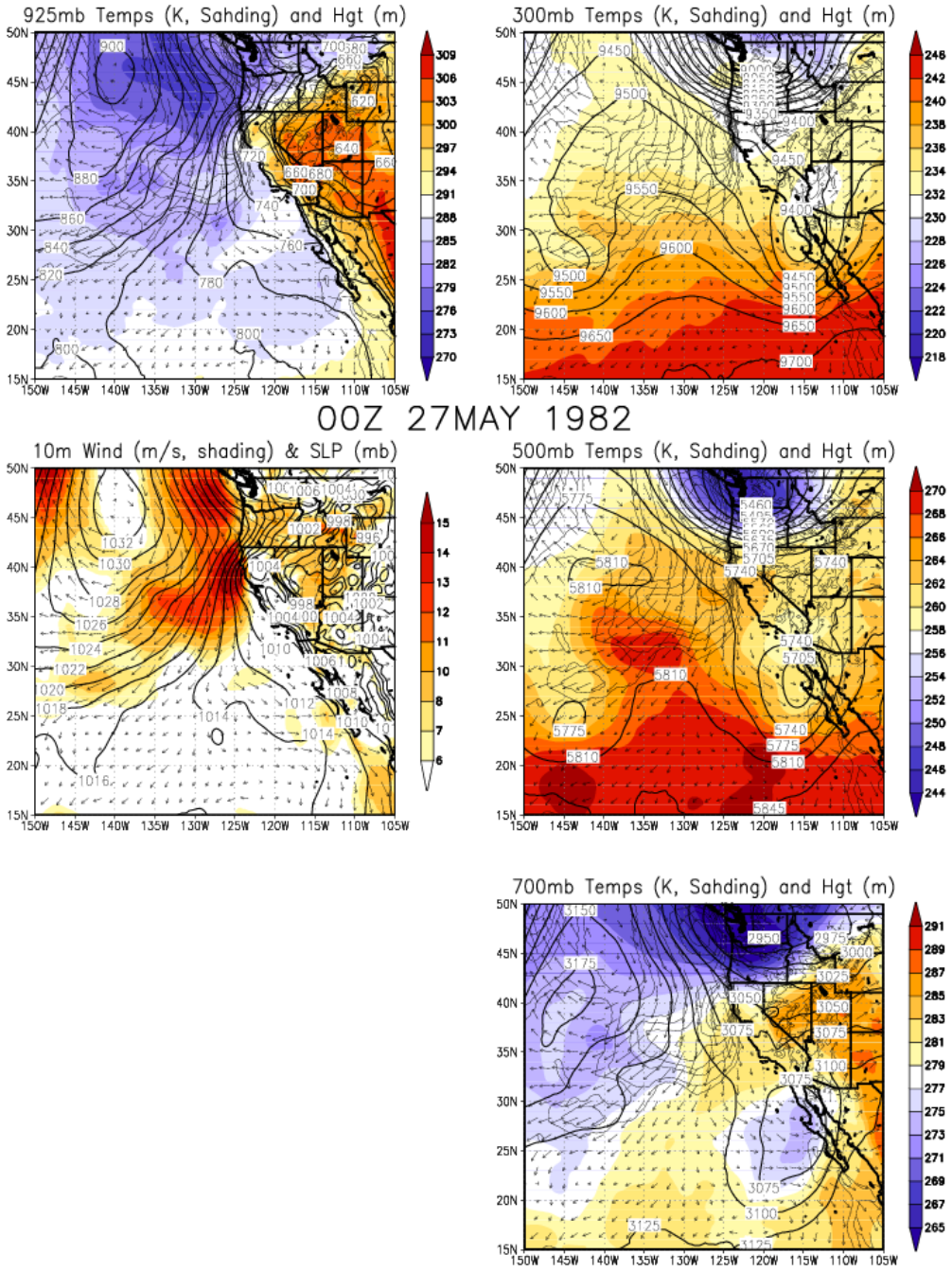

Appendix Figure A3: Wind event case study. The bottom left-panel shows QuikScat wind speed and direction estimates. The other panels show NARR fields at the specified levels.

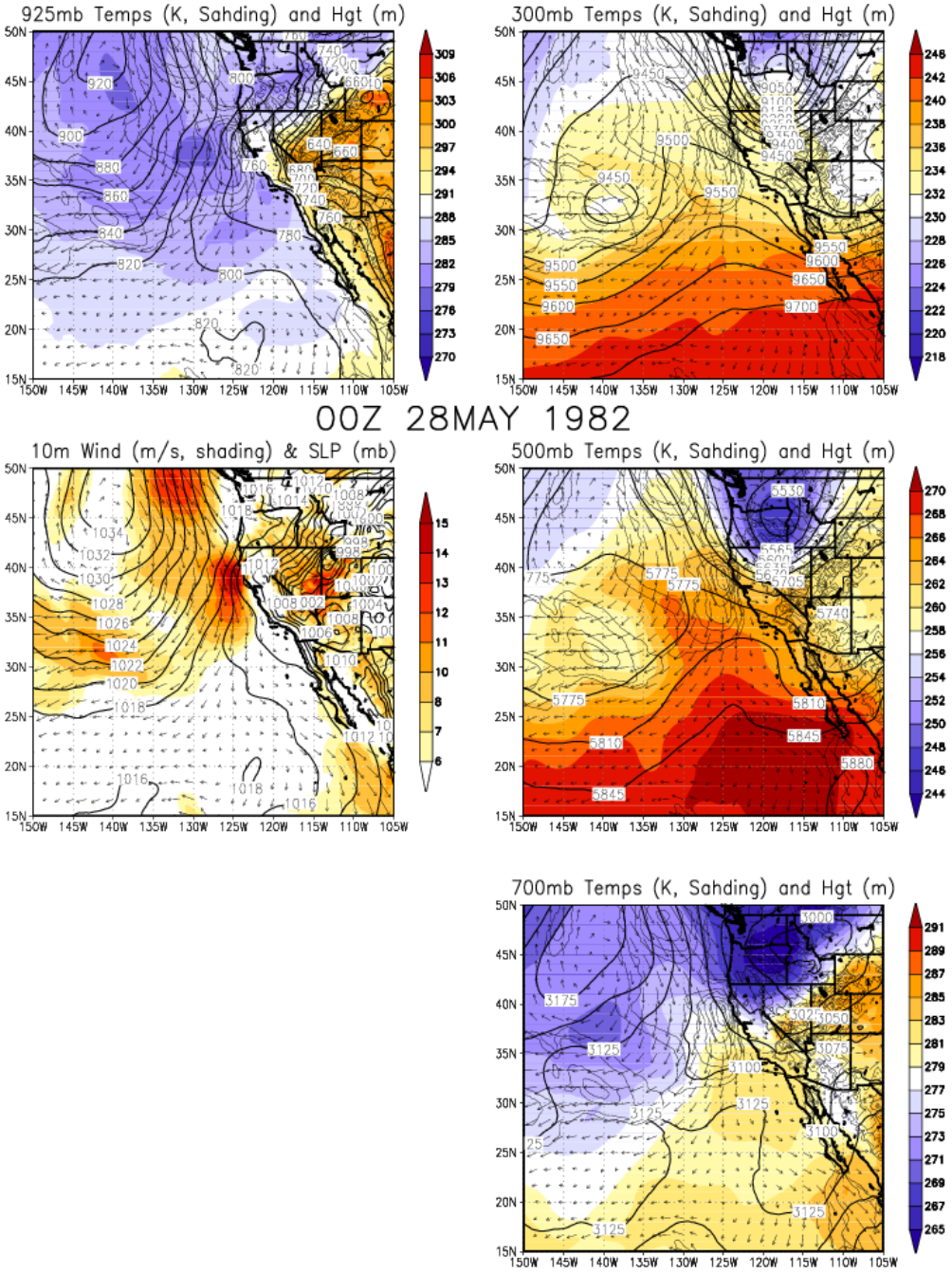

Appendix Figure A4: Wind event case study. The bottom left-panel shows QuikScat wind speed and direction estimates. The other panels show NARR fields at the specified levels.

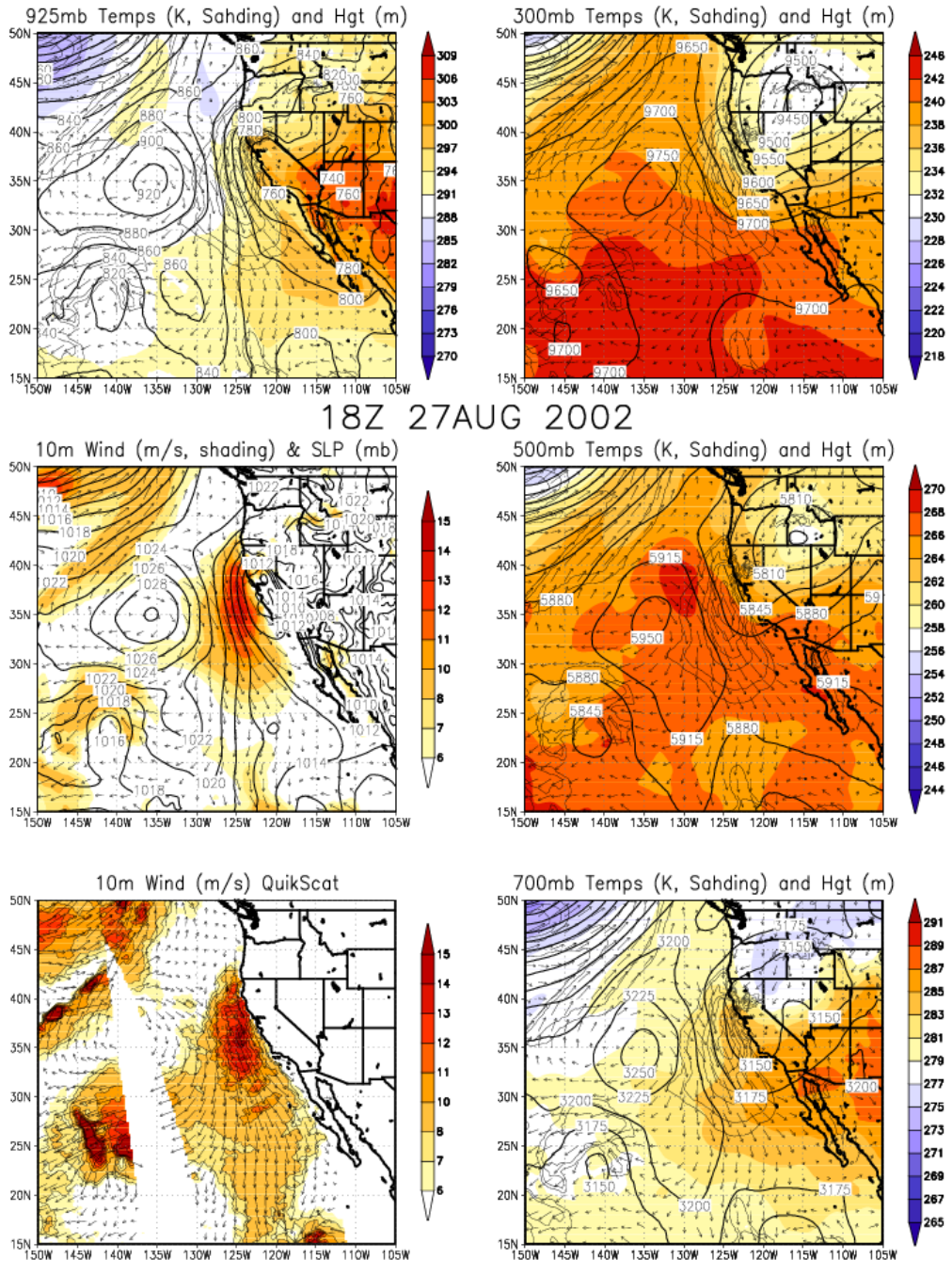

Appendix Figure A5: Wind event case study. The bottom left-panel shows QuikScat wind speed and direction estimates. The other panels show NARR fields at the specified levels.

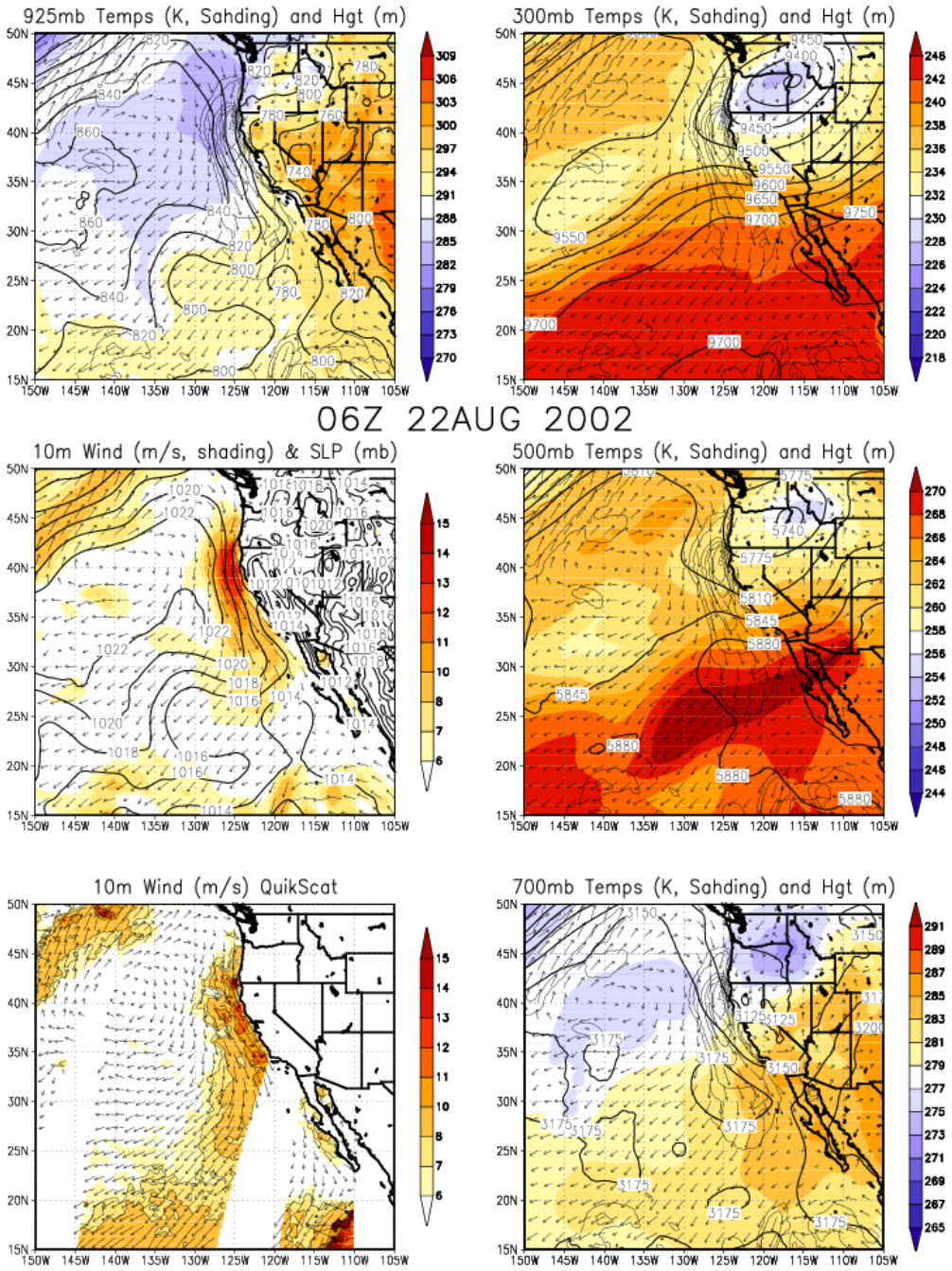

Appendix Figure A6: Wind event case study. The bottom left-panel shows QuikScat wind speed and direction estimates. The other panels show NARR fields at the specified levels.

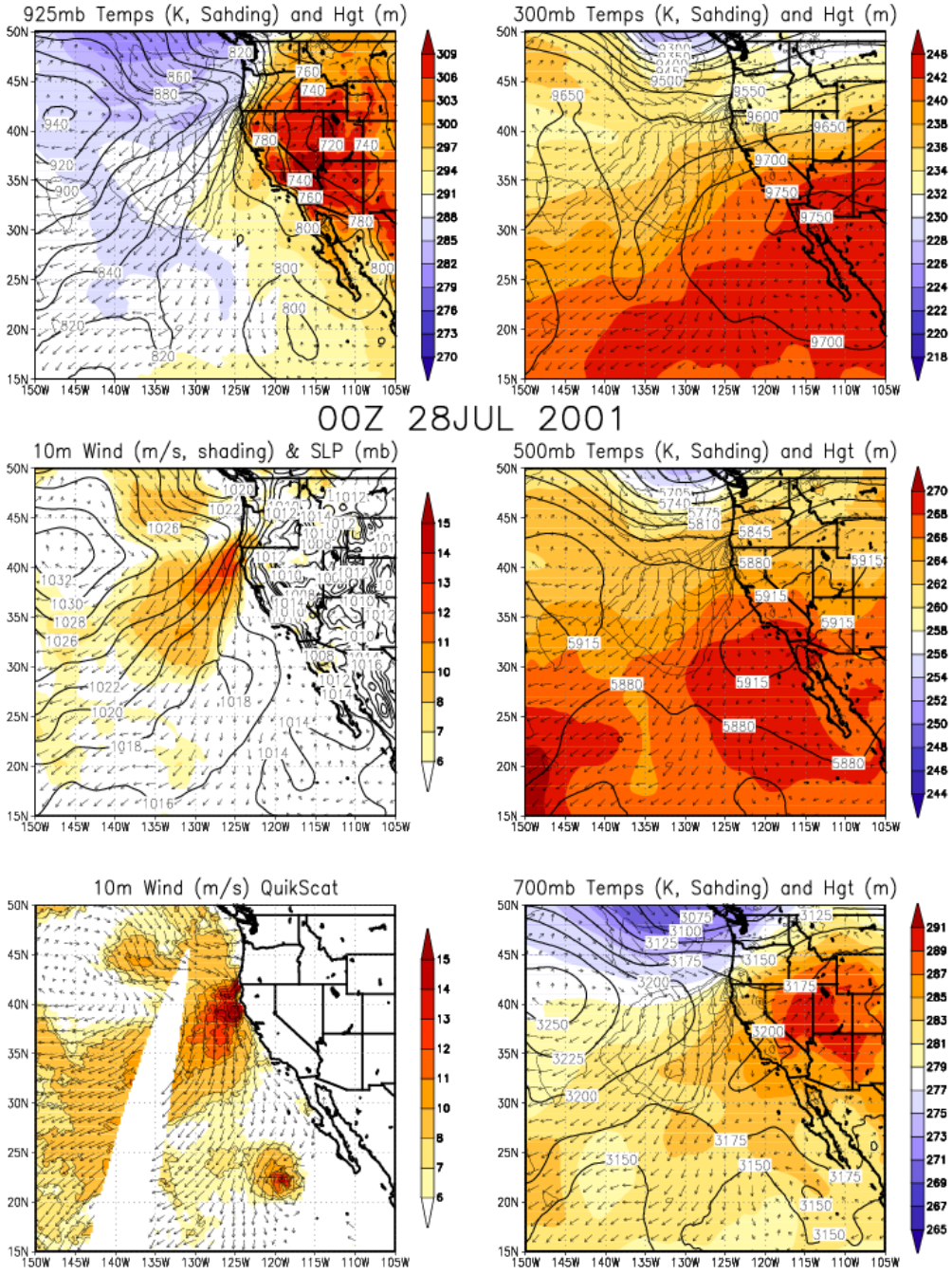

Appendix Figure A7: Wind event case study. The bottom left-panel shows QuikScat wind speed and direction estimates. The other panels show NARR fields at the specified levels.

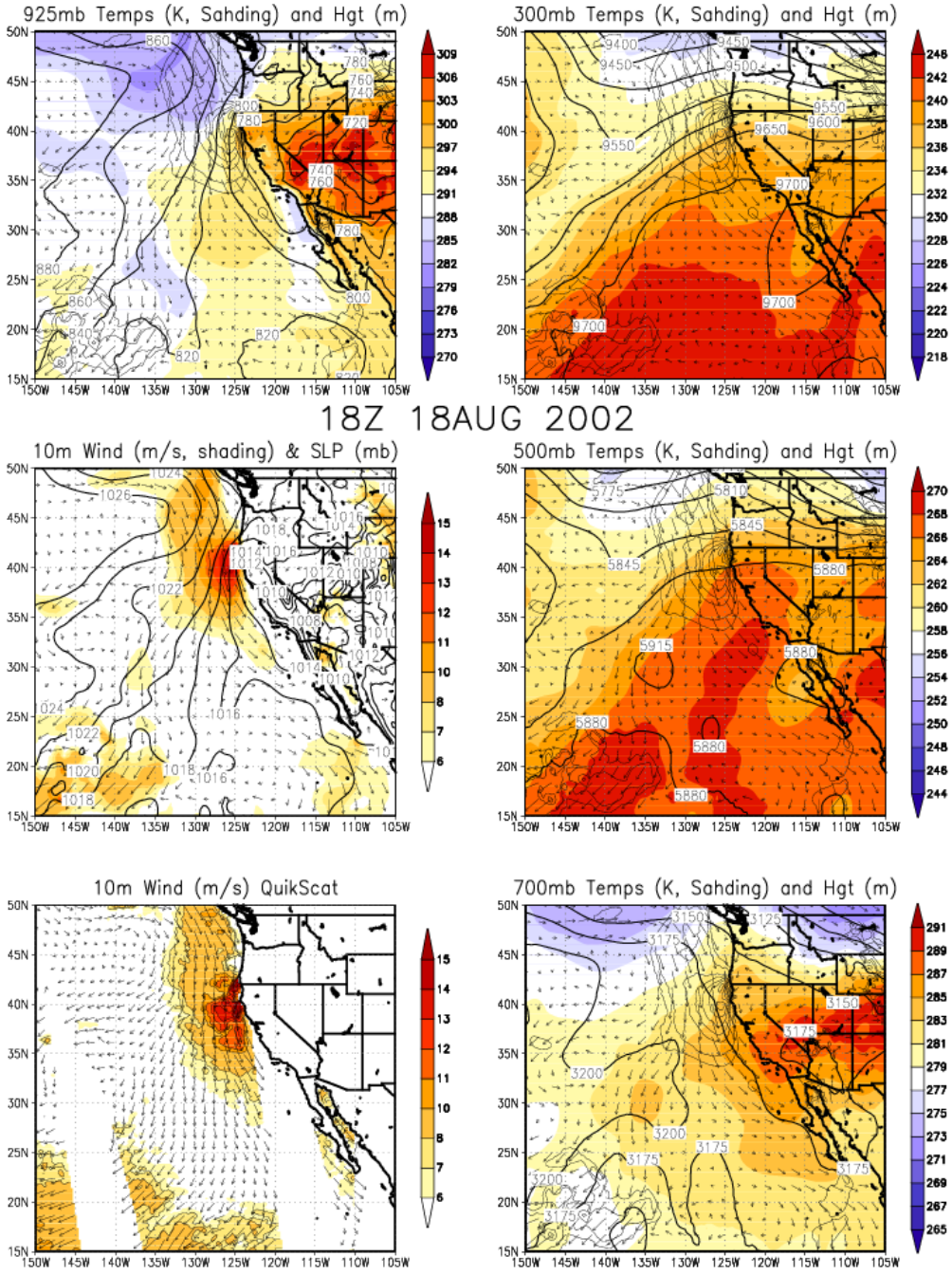

Appendix Figure A8: Wind event case study. The bottom left-panel shows QuikScat wind speed and direction estimates. The other panels show NARR fields at the specified levels.

REFERENCES

Bakun, A., and C. S. Nelson (1991), Wind stress curl in subtropical eastern boundary current regions, J. Phys. Ocanogr., 21, 1815-1834.

Baynton, H. W., J. M. Bidwell, and D. W. Beran (1965), The association of the low-level inversions with surface wind and temperature at Point Arguello, J. Appl. Meteor., 4, 509-516.

Beardsley, R. C., C. E. Dorman, C. A. Friehe, L. K. Rosenfeld, and C. D. Winant (1987), Local atmospheric forcing during the Coastal Ocean Dynamics Experiment 1. A description of the marine boundary layer and atmospheric conditions over a Northern California upwelling region, J. Geophys. Res., 92(C2), 1467-1488.

Brost, R. A., D. H. Lenschow, and J. C. Wyngaard, (1982), Marine stratocumulus layers: Mean conditions, J. Atmos. Sci., 39, 800-817.

Burk, S. D., and W. T. Thompson (1996), The summertime low-level jet and MBL structure along the California coast, Mon. Wea. Rev., 124, 668-686.

Caldwell, P. C., and D. W. Stuart (1986), Mesoscale wind variability near Point Conception, California during spring 1983, J. Clim. Appl. Meteor., 25, 1241-1254.

Cavazos, T., 2000: Using self-organizing maps to investigate extreme climate events: an application to wintertime precipitation in the Balkans. J. Clim., 13, 1605-1808.

Chelton, D. B., M. G. Schlax, M. H. Freilich, and R. F. Milliff (2004), Satellite radar measurements reveal short-scale features in the wind stress field over the world ocean, Science, 303, 978-983.

Chelton, D. B., and M. H. Freilich (2005), Scatterometer-based assessment of 10-m wind analyses from the operational ECMWF and NCEP numerical weather prediction models, Mon. Wea.Rev., 133, 409-429.

Cui, Z., M. Tjernstrom, and B. Grisogono (1998), Idealized simulations of atmospheric coastal flow along the central coast of California. J. Appl. Meteorol., 37, 1332-1363.

Dabberdt, W. F., and W. Viezee (1987), South Central Coast Cooperative Aerometric Monitoring Program (SCCCAMP), Bull. Am. Meteor. Soc., 68, 1098-1110.

Dorman, C. E., T. Holt, D. P. Rogers, and K. A. Edwards (2000), Large-scale structure of the June-July 1996 marine boundary layer along California and Oregon, Mon. Wea. Rev., 128, 1632-1652.

Dorman, C.E., D.P. Rogers, W. Nuss, W.T. Thompson (1999), Adjustment of the summer marine boundary layer around Point Sur, California. Mon. Wea. Rev., 127, 2143-2159.

Dorman, C.E., C.D. Winant (2000), The structure and variability of the marine atmosphere around the Santa Barbara Channel. Mon. Wea. Rev., 128, 261-282.

Dorman, C. E., and C. D. Winant (1995), Buoy observations of the atmosphere along the west coast of the United State, 1981-1990, J. Geophys. Res., 100(C8), 16029-16044, doi:10.1029/95JC00964.

Draper, D. W., and D. G. Long (2002), An assessment of SeaWinds on QuikSCAT wind retrieval, J. Geophys. Res., 107, 3212, doi:10.1029/2002/JC001330.

Dudhia, J. (1993), A non-hydrostatic version of the Penn State/NCAR mesoscale model: Validation tests and simulation of an Atlantic cyclone and cloud front, Mon. Wea. Rev., 121, 1493-1513.

Ebuchi, N., H. C. Graber, and M. J. Caruso (2002), Evaluation of wind vectors observed by QuikSCAT/SeaWinds using ocean buoy data, J. Atmos. Oceanic Technol., 19, 2049-2062.

Edwards, K. A., D. P. Rogers, and C. E. Dorman (2002), Adjustment of the marine atmospheric boundary layer to the large-scale bend in the California coast, J. Geophys. Res., 107(C12), 3213, doi:10.1029/2001JC000807.

Elliot, D. L., and J. J. O'Brien (1977), Observational studies of the marine boundary layer over and upwelling region, Mon. Wea. Rev., 105, 86-98.

Filonczuk, M. K., D. R. Cayan, and L. G. Riddle (1995), Variability of marine fog along the California coast, Scripps Institution of Oceanography Reference No. 95-2, pp. 102.

Fosberg, M. A., and M. J. Schroeder (1966), Marine air penetration in central California, J. Appl., Meteor., 5, 573-589.

Freeman, J.C., Jr, 1950: The wind field of the equatorial east Pacific as a Prandtl-Meyer expansion. Bull. Amer. Meteor. Soc., 31, 303-304.

Freilich, M. H., D. G. Long, and M. W. Spencer (1994), SeaWinds: a scanning scatterometer for ADEOS II - science overview, Proc. Int. Geoscience and Remote Sensing Symp., Pasadena, CA, IEEE, 960-963.

Gilhousen, D. B. (1987), A field evaluation of NDBC moored buoy winds, J. Atmos. Ocean. Tech., 4, 94-104.

Haack, T. and S.D. Burk (2001), Summertime marine refractivity conditions along coastal California, J. Appl. Meteor., 40, 673-687.

Halliwell, G. R. and J. S. Allen (1987), The large-scale coastal wind field along the west coast of North America, 1981-1982, J. Geophys. Res., 92(C2), 1861-1884.

Hamilton, G. D. (1980), NOAA Data Buoy Office programs, Bull. Amer. Meteor. Soc., 61, 1012-1017.

Hewitson, B. B., and R. G. Crane, 2002: Self-organizing maps: applications to synoptic climatology, Clim. Res., 22, 13-36.

Hodur, R.M. (1987), Evaluation of a regional model with an update cycle, Mon. Wea. Rev., 115, 2707-2718.

Hogan, T.F., and T.E. Rosmond (1991), The description of the Navy Operational Global Atmospheric Prediction System's spectral forecast model, Mon. Wea. Rev., 119, 1786-1815.

Hoskins, B. J. (1996), On the existence and strength of the summer subtropical anticyclones, Bull. Am. Met Soc., 77, 1287-1292.

Hsu, S. A., E. A. Meindl, D. B. Gilhousen, (1994), Determining the power-law wind-profile exponent under near-neutral stability conditions at sea, J. Applied Meteor., 33(6), 757-765.

Huyer, A. (1983), Coastal upwelling in the Caliornia Current system, Prog. Oceanog., 12, 259-284.

Kalnay, E., and Coauthors (1996), The NCEP/NCAR 40-year reanalysis project, Bull. Amer. Meteor. Soc., 77(3), 437-471.

Kanamitsu, M., and Coauthors (2002), NCEP/DOE AMIP-II Reanalysis (R-2). Bull. Amer. Meteor. Soc., 82, 247-267.

Kaski, S., J. Kangas, and T. Kohonen (1998), Bibliography of Self-Organizing Map (SOM) Papers: 1981-1997, Neural Computing Surveys, 1: 102-350

Klein, S. A., D. L. Hartmann, and J. R. Norris (1995), Relationships among low cloud structure, sea surface temperature, and atmospheric circulation. J. Clim., 8, 1140-1155.

Kohonen, T., (1982) Self-organized information of topologically correct features maps. Biol. Cybernetics, 43, 59-69.

Kohonen, T., (1989) Self-organization and associative memory, 3rd edn. Spring-Verlag, Berlin.

Kohonen, T., J. Hynninen, J. Kangas, and J. Laaksonen, (1995) SOM_PAK, The self-organizing map program package Version 3.1. Helsinki University of Technology, Laboratory of Computer and Information Science. [Avaliale online at: Http://www.cis.hut.fi/nnrc]

Kohonen, T. (2001) Self-Organizing Maps. Springer, Berlin, 3rd edition.

Large, W. G., and S. Pond (1982), Sensible and latent heat flux measurements over the ocean, J. Phys. Oceanogr., 12, 464-482.

Lindzen, R., and A. Hou (1988), Hadley circulations for zonally averaged heating centered off the equator. J. Atmos. Sci., 45, 2416-2427.

Liu, W. T. (2002), Progress in scatterometer application, J. Oceanogr., 58, 121-136.

Liu, W. T., and W. Tang (1996), Equivalent neutral wind, JPL Publication 96-17, Pasadena, CA, 8 pp.

Liu, W. T., and X. Xie (2001), Improvement in spacebased scatterometers and increased scientific impact in the past decade, Proc. Oceans 2001, Honolulu, HI., Vol. 1, Marine Technology Society, 626-630.

Liu, Y., R. H. Weisberg, and R. He, 2006: Sea surface temperature patterns on the west Florida shelf using growing hirerarchical self-organizing maps

Liu, Y.M., G.X. Wu, and R. Ren, 2004: Relationship between the subtropical anticyclone and diabatic heating. J. Climate, 17, 682-698.

Lorenz, E. N. (1969), The nature of the global circulation of the atmosphere: a present view, The Global Circulation of the Atmosphere Royal Meteorological Society, 3-23.

Lovegrove, J. (2003), Redefining small craft advisory for hazardous seas, National Weather Service Western Region Tech Attach. No. 03-11, pp. 9.

Mass, C. F., M. D. Albright, and D. J. Brees (1986), The onshore surge of marine air into the Pacific Northwest: a coastal region of complex terrain, Mon. Wea. Rev., 114, 2602-2627.

Mears, C. A., D. K. Smith, and F. J. Wentz (2001) Comparison of Special Sensor Microwave Imager and buoy-measured wind speeds from 1987 to 1997, J. Geophys. Res., 106, 11 719-11 729.

Miller, A. J., et al. (1999) Observing and modeling the California Current System, Eos, Transactions, American Geophysical Union, 80, 533-539

Miyasaka, T., and H. Nakamura (2005), Structure and formation mechanisms of the Northern Hemisphere summertimes subtropical highs, J. Clim., 18, 5046-5065.

Mesinger, F., (2000) Numerical methods: The Arakawa approach, horizontal grid, global, and limited-area modeling. General Circulation Model Development, D.A. Randall, Ed., Academic Press, 373-419.

Mesinger, F., and Coauthors, (2006) North American Regional Reanalysis. Bull. Amer. Meteor. Soc., March, 343-360.

Mesinger, F., and Coauthors, (2005), North American Regional Reanalysis: Evaluation Highlights and Early Usage , Eos Trans. AGU, 86(18), Jt. Assem. Suppl., Abstract A21B-06

Mo, K., and M. Chelliah (2006), The Modified Palmer Drought Severity Index Based on the NCEP North American Regional Reanalysis. J. Appl. Meteor. and Climat., 45, 1362-1375. DOI: 10.1175/JAM2402.1

Mo, K., M. Chelliah, M. Carrera, R. Higgins, and W. Ebisuzaki (2005), Atmospheric Moisture Transport over the United States and Mexico as Evaluated in the NCEP Regional Reanalysis. J. Hydromet., 6, 710-728, DOI: 10.1175/JHM452.1

Munk, W. (1950), On the wind-driven ocean circulation. J. Meteor., 7, 79-93.

Naderi, F. M., M. H. Freilich, and D. G. Long (1991), Spaceborne radar measurement of wind velocity over the ocean - An overview of the NSCAT scatterometer system, Proc. IEEE, 97, 850-866.

Neiburger, M., D. S. Johnson, and C.-W. Chien (1961), Studies of the structure of the atmosphere over the eastern Pacific Ocean in summer, volume 1(1) of University of California Publications in Meteorology. University of California Press, 1961. 58 pp.

Nelson, C. S. (1977), Wind stress and wind stress curl over the California Current, NMFS Rep. SSRF-714, 87 pp.

Norris, J. R., and C. B. Leovy (1994), Interannual variability in stratiform cloudiness and sea surface temperature. J. Clim., 7, 1915-1925.

Oja, M., Kaski, S., and T. Kohonen (2003), Bibliography of Self-Organizing Map (SOM) Papers: 1998-2001 Addendum, Neural Computing Surveys, 3: 1-156.

Perlin, N., R. M. Samelson, and D. B. Chelton (2004), Scatterometer and model wind and wind stress in the Oregon-Northern California coastal zone, Mon. Wea. Rev., 132, 2110-2129.

Pincus, R., M. B. Baker, and C. S. Bretherton (1997), What controls stratocumulus radiative properties? Lagrangian observations of cloud evolution, J. Atm. Sci., 54, 2215-2236.

Rodwell, M., and B. Hoskins (2001), Subtropical anticyclones and summer monsoons. J. Clim., 14, 3192-3211.

Rogers, D. P., et al (1998), Highlights of Coastal Waves 1996, Bull. Am. Met Soc., 79, 1307-1326.

Rogers, E., M. Elk, Y. Lin, K. Mitchell, D. Parrish, and G. DiMego, (2001) Changes to the NCEP Meso Eta analysis and forecast system: Assimilation of Observed precipitation, upgrades to land-surface physics, modified 3DVAR analysis., EMC, NCEP. [Available online at www.emc.ncep.noaa/glov/mmb/mmbpll/spring2001/tpb.]

Ruiz-Barradas, A., and S. Nigam (2006), Great Plains Hydroclimate Variability: The View from North American Regional Reanalysis. J. Climate, 19, 3004-3010, DOI: 10.1175/JCLI3768.1

Schlax, M.G., D.B. Chelton, and M.F. Freilich (2001), Sampling errors in wind fields constructed from single and tandem scatterometer datasets, J. Atmos. Oceanic Technol., 18, 1014-1036.

Seager, R., R. Murtugudde, N. Naik, A. Clement, N. Gordon, and J. Miller (2003), Air-sea interaction and the seasonal cycle of the subtropical anticyclones, J. Clim., 16, 1948-1966.

Waliser, D., and R. Somerville (1994), Preferred latitudes of the intertropical convergence zone. J. of the Atm. Sci., 51, N12, 1619-1639.

Wang, J., and K.P. Georgakakos (2005), Effects of cold microphysical processes on the surface precipitation variability of nonsquall tropical oceanic convection, J. Geophys. Res., 110, DOI:10.1029/2005JD005787.

Wang, Y., S.-P. Xie, B. Wang, and H. Xu (2005), Large-scale atmospheric forcing by southeast Pacific boundary layer clouds: A regional model study. J. Climate, 18, 934-951.

Wentz, F. J. (1997), A well-calibrated ocean algorithm for special sensor microwave/imager, J. Geophys. Res., 102(C4), 8703-8718.

Winant, C. D., and C. E. Dorman (1997), Seasonal patterns of surface wind stress and heat flux over the Southern California Bight, J. Geophys. Res., 102, 5641-5653, doi:10.1029/96JC02801.

Winant, C. D., C. E. Dorman, C. A. Friehe, and R. C. Beardsley (1988), The marine layer off Northern California: an example of supercritical channel flow, J. Atm. Sci., 45, 3588-3605.

Yen-Nakafuji, D. (2005), California Wind Resources, CEC publication # CEC-500-2005-071-D, 31 pp.